Application of a Novel Quasi-3D Microscopy Technique to Investigate Early Osteocyte Mechanotransduction Events

Andrew D. Baik

Submitted in partial fulfillment of the
requirements for the degree of
Doctor of Philosophy
in the Graduate School of Arts and Sciences

COLUMBIA UNIVERSITY

2013

© 2012
Andrew D. Baik
All Rights Reserved

ABSTRACT

Application of a Novel Quasi-3D Microscopy Technique to Investigate Early Osteocyte Mechanotransduction Events

Andrew D. Baik

The objective of this thesis is to observe and characterize the early mechanical and biochemical events in osteocyte mechanotransduction.

Physical forces have been increasingly implicated in normal physiological and pathological cellular activities of osteocytes. The mechanotransduction process in osteocytes involves spatiotemporally complex changes in cytoskeletal organization, signal activation, and whole cell mechanical properties. Most *in vitro* biophysical techniques currently available sacrifice either spatial or temporal resolution and are unable to visualize 3D cellular behavior on the millisecond time scale. Here, we develop a novel multi-channel quasi-3D microscopy technique to simultaneously visualize and measure whole-cell mechanics, intracellular cytoskeletal deformation, and biochemical signal activation under fluid shear flow.

The technique was applied to visualize cell dilatation and cytoskeletal deformation in osteocytes under steady fluid shear flow. Analysis of the plasma membrane and either the intracellular actin or microtubule cytoskeletal networks provided characterization of their deformations over time. No volumetric dilatation of the whole cell was observed under flow, and both cytoskeletal networks experienced primarily tensile viscoelastic creep and recovery in all measured strain components. Intra- and inter- cellular mechanical heterogeneity was observed in both cytoskeletal networks.

Cytoskeletal disruption pointed towards a unidirectional mechanical interaction where microtubule networks affected actin network strains, but not vice versa.

The second study in this thesis investigated the effects of steady and oscillatory flow on the actin and microtubule networks within the same cell. Shear strain was the predominant strain in both steady and oscillatory flows, in the form of viscoelastic creep and elastic oscillations, respectively. Under oscillatory fluid shear flow, the actin networks displayed an oscillatory strain profile more often than the MT networks in all the strains tested and had a higher peak-to-trough magnitude. Taken together with the first study, the actin networks were determined to be the more responsive cytoskeletal networks in osteocytes to fluid flow and may play a bigger role in mechanotransduction.

The final culminating study tracked $[Ca^{+2}]_i$ and F-actin network strains simultaneously in a single osteocyte. We demonstrated novel osteocyte mechano- and transduction behavior where $[Ca^{+2}]_i$ oscillations activate phasic actomyosin contractions using a smooth muscle-like mechanism. Fluid shear, ATP, and ionomycin induced $[Ca^{+2}]_i$ signaling with a subsequent compression and recovery in actin strains of the cell, being most apparent in the height direction strain. This contraction was reversible over the period of hundreds of seconds. ML-7, a myosin light chain kinase inhibitor, significantly slowed down the kinetics of contraction initiation, but blebbistatin, a potent skeletal and non-muscle inhibitor, had no effect on the actin contraction. Furthermore, smooth muscle contraction-related proteins were detected by Western blot. The observation of muscle-like contractility in osteocytes demonstrates a possible positive feedback mechanism of osteocytes to activate mechanotransduction pathways.

Table of Contents

List of Tables

List of Figures

Acknowledgements

While there is only one name on the first page of this dissertation, it is by no means accurate to assume that I was able to complete this work by myself. The completion of this dissertation came through the support and guidance of many people of whom I am indebted to. In chronological order because I can't figure out a better way:

I would like to thank my parents for their unconditional love. Being first generation immigrants to America was not easy, but they chose this route to ensure that my brother and I would have access to the best education and opportunities. Their teaching of duty and the pursuit of excellence helped guide me through my life.

I would like to thank my Lord and Savior, Jesus Christ, who has been setting a crooked path straight(er) and has blessed me with the opportunity to study the beauty of the machine that is the human body.

Dr. X. Edward Guo, my graduate advisor, is the man behind the entire thesis and my research career. The door to his office was always open, and I sincerely appreciate the opportunities that he provided me to participate in writing grants and attending conferences around the world. His mentorship has been invaluable in shaping my career as a scientist.

I would also like to thank my committee, Dr. Clark T. Hung, Dr. Chris R. Jacobs, Dr. Elizabeth M. Hillman, and Dr. Cheng Dong, for their advice, perspectives, and technical expertise. They have been invaluable sources of inspiration and guidance on how to navigate the minefield that is a PhD. Their helpful comments have helped refine my research ideas and projects towards something resembling a rigorous scientific study.

I would like to thank the veteran members of the Bone Bioengineering Laboratory, Dr. Lucas Lu, Dr. Sherry Liu, and Dr. Ete Chan. They were older siblings in the lab who helped me

adjust to Columbia and lent a hand in any problem I ran into. I can only hope to be as helpful as they were to me to future students. I would also like to thank the current members of the lab for the joy and great times we've shared in organizing conferences and cleaning up the lab. Jun Qiu, Bin Zhou, Genevieve Brown, Eric Yu, Ji Wang, Da Jing, and Dr. Isabel Leong have all played a role in my physical and emotional wellbeing in the laboratory whenever a failed experiment diminished my will to continue.

I'd also like to thank my colleagues in the Columbia Biomedical Engineering Department for their presence and good times. Specifically, Keith Yeager, Andrew Kang, Heon Goo Lee, Yukkee Cheung, Evren Azeloglu, Andrea Tan, Kristen Lee, Jarett Michaelson, and Julia Chen. The staff that keeps our department running, Jarmaine Lomax, Michelle Cintron, Paulette Louissaint, and Shila Maghji, have been invaluable in tracking down lost packages or lost paychecks. Without them, I would not have been able to do anything.

I'd like to especially thank Timothy K. Lee, a dear friend who started graduate school in Bioengineering at the same time as me, although across the country at Stanford. He has been a source of encouragement (and MATLAB code) to me as we commiserated together through our respective studies.

And finally, I thank my soulmate and fiancée, Mirae Kang, to whom I love and support, as she has loved and supported me with homemade bento boxes and for falling asleep whenever I practiced scientific talks on her. Her support has made these achievements possible.

Chapter 1. Overview

1.1 General Background

1.1.1 Osteocytes in Bone

Among the three major classes of bone cells (osteoblasts, osteoclasts, and osteocytes), osteocytes have attracted particular interest recently (Bonewald and Johnson 2008; Bonewald 2011). Osteocytes are terminally differentiated cells from the osteoblastic lineage of mesenchymal stem cells. However, osteocytes are drastically different in shape and function than osteoblasts. 95% of the population of bone cells at any given time are osteocytes, showing their relative intransience compared to the osteoblast and osteoclast cell types, which are differentiated primarily during turnover phases of bone tissue. Recent mouse conditional knockout studies have established the osteocyte as a mechanosensory cell type that acts as a regulator of osteoblast and osteoclast differentiation through production of molecules such as sclerostin and receptor activator of nuclear factor-κB ligand (RANKL) (Tatsumi, Ishii et al. 2007; Kramer, Halleux et al. 2010; Nakashima, Hayashi et al. 2011; Xiong, Onal et al. 2011). Osteocytes are "entombed" in the lacunocanalicular system of bone's mineralized matrix and are interconnected with each other and with other cell types through intercellular processes. Mechanical load-induced fluid flow through the lacuncanalicular system has been proposed to provide the necessary nutrients and waste removal to maintain osteocyte health and communication with the rest of the body (Piekarski and Munro 1977; Price, Zhou et al. 2011). An additional effect of this fluid transport is fluid flow-induced shear

stresses over the cell body and processes of the embedded osteocytes in the pericellular space (Weinbaum, Cowin et al. 1994; Burger and Klein-Nulend 1999).

1.1.2 Cellular Mechanotransduction

Mechanotransduction is defined as the "conversion of a biophysical force into a cellular response" (Duncan and Turner 1995). Mechanical forces such as gravity, fluid shear, and sound waves are transduced into biochemical signals within a cell. This process is used for diverse functions in the body such as the hearing and touch senses. Since the discovery of mechanical stretch-activated membrane ion channels (Guharay and Sachs 1984), research has been focused on precisely how mechanical signals are perceived by cells and converted into biological outputs. For example, the extracellular matrix and the integrin/focal adhesion complex have been shown to directly transduce mechanical stresses from fluid shear flow to regulate cell proliferation and apoptosis pathways in endothelial cells (Shyy and Chien 1997). The intracellular cytoskeleton is also active in propagating and transducing stresses across the cell to areas that have mechanosensitive proteins, such as the nucleus (Wang, Butler et al. 1993; Na, Collin et al. 2008). Clearly, mechanical inputs are sensed by multiple intracellular structures depending on the magnitude and type of mechanical stress applied to the body.

1.1.3 Osteocyte Mechanotransduction

It has been hypothesized that the dominant loading mechanism of the mechanosensing osteocytes is oscillatory fluid shear stress resulting from the mineralized matrix deformation of bone (Owan, Burr et al. 1997; Jacobs, Yellowley et al. 1998; You, Yellowley et al. 2000). Osteocytes *in vivo* are characterized by a spherical or ellipsoidal cell body with a large number of dendritic processes that connect to other osteocytes and

to the bone surface (Vatsa, Breuls et al. 2008; van Hove, Nolte et al. 2009). Several groups have posited unique mechanotransduction properties in the processes involving glycocalyx in the canalicular space and have calculated that the fluid shear stresses in the lacunae are too low to be sensed by osteocytes (Cowin, Weinbaum et al. 1995; Reilly, Haut et al. 2003; Han, Cowin et al. 2004). Interestingly, other research groups (Adachi, Aonuma et al. 2009; Burra, Nicolella et al. 2010) have established differences in the mechanosensitivity of the cell body and cell processes in *in vitro* experiments.

Most *in vitro* fluid shear studies on primary osteocytes and osteocyte cell lines have focused on monolayers of flat, spread osteocytes, but few *in vitro* studies have recapitulated the correct spherical or ellipsoidal cell body shape. One particular study demonstrated that osteocytes are much more mechanosensitive in this 3D configuration than when flat and spread (Bacabac, Mizuno et al. 2008). This suggests that the whole picture of osteocyte mechanosensitivity is incomplete, especially when considering the *in vivo* shape and microenvironment of the cellular processes and cell body. While it has been hypothesized that the osteocyte cell body experiences lower strains *in vivo,* the current evidence suggests that its native rounded shape may compensate for this and still be highly mechanosensitive. Furthermore, key mechanical signaling complexes decorate the periphery of cell body and not the cellular processes, such as the putative focal adhesion complexes i*n vivo* (Kamioka, Sugawara et al. 2006; Vatsa, Semeins et al. 2008), which can sense and transmit forces directly (Grashoff, Hoffman et al. 2010). Additionally, the actin and microtubule networks have been imaged in osteocytes and show unique properties and distributions from other cell types (Tanaka-Kamioka, Kamioka et al. 1998). Therefore, it was of interest in this thesis to characterize the

deformational behavior of the osteocyte's cell body under a physiological level of fluid shear flow for better characterization of understudied, potential mechanisms.

How an osteocyte deforms under a dynamic, oscillating fluid flow is still poorly understand in two important aspects. First, most *in vitro* cell studies of osteocytes under oscillating flow have been performed on either semi-confluent or confluent adherent osteocytes. Very few studies have considered the mechanical behavior of osteocytes at the single cell level (Baik, Lu et al. 2010; Rath, Bonewald et al. 2010). In a recent study on bone cell deformation under oscillating flow, microspheres were attached to the cell membrane and displacements of these microspheres were used to indicate the dynamic displacement of cell deformation. The tested bone cells deformed more or less elastically under dynamic oscillating flow but viscoelastically under a steady flow (Kwon and Jacobs 2007). This highlights the need to characterize osteocyte mechanics under appropriate fluid shear flow patterns. Furthermore, recent experimental and theoretical evidence suggest the existence of subcellular location-dependent responsiveness to fluid shear (Wang, McNamara et al. 2007; Adachi, Aonuma et al. 2009). However, this critical hypothesis of mechanotransduction in osteocytes remains to be verified under physiological oscillating flow. Limitations in temporal or spatial resolution of traditional microscopy techniques (i.e. confocal, deconvolution, widefield) have hindered the ability to capture the 3D mechanical behavior of osteocytes because of the dynamic nature of oscillating flow (1 Hz).

1.1.4 Calcium Signaling in Osteocytes

Ca^{+2}/calmodulin is a ubiquitous second messenger system in mammalian cells. Temporal changes in the intracellular concentration of Ca^{+2} ($[Ca^{+2}]_i$), such as in action

potentials, can encode signals to activate broad downstream molecules such as protein kinase A, protein kinase C, CaM kinase, and myosin light chain kinase. Two major sources of Ca^{+2} are intracellular stores such as the sarcoplasmic or endoplasmic reticulum and the extracellular space. Trafficking through membrane channels regulate the influx and efflux.

Osteocytes have been shown to utilize Ca^{+2} signaling to regulate bone physiology. For example, ATP, 17β-estradiol, and PTH are physiologically relevant signaling molecules that can activate intracellular Ca^{+2} signaling pathways in bone (Miyauchi, Notoya et al. 2000; Gu, Preston et al. 2001; Huo, Lu et al. 2010; Ren and Wu 2012). The focus of this thesis and of this section will be on mechanically regulated Ca^{+2} signaling. Early studies demonstrated PGE_2 production in osteocytes was regulated by Ca^{+2} signaling (Ajubi, Klein-Nulend et al. 1999). Remarkably, fluid shear flow stimulated more $[Ca^{+2}]_i$ oscillations in osteocytes than from substrate strain, presumably due to the higher intracellular strain development (You, Yellowley et al. 2000), lending credence to the hypothesis that fluid shear flow is the predominant mechanical load that osteocytes respond to. A recent study in our laboratory demonstrated that osteocytes display multiple $[Ca^{+2}]_i$ oscillations/spikes in response to steady and oscillatory flow (Lu, Huo et al. 2012). This behavior was not observed in the predecessor osteoblast cell type (Lu, Huo et al. 2012). ATP secretion from fluid flow was determined to be the primary mechanism by which osteocytes received stimuli to generate multiple $[Ca^{+2}]_i$ spikes. Differences in ATP release mechanisms and ratios of voltage-sensitive calcium channel types in osteocytes and osteoblasts may account for these disparate $[Ca^{+2}]_i$ responses (Genetos, Kephart et al. 2007; Thompson, Majid et al. 2011).

1.1.5 Genetically Encoded FRET-based Biosensors

Advances in the development of a wide variety of recombinant fluorescent proteins (FP) have allowed the application of Fluorescent/Forster resonance energy transfer (FRET) using fluorescent proteins. FRET, in the context of its most common usage in fluorescent microscopy, refers to the ability of a donor fluorophore to transfer energy to an acceptor fluorophore. Proper choices of donor and acceptor fluorophores with overlapped donor emission with acceptor excitation allows FRET to occur. This FRET efficiency depends on fluorophore orientations and intermolecular distance, with exponential increases in efficiency at distances lower than 10nm. Protein-protein interactions on a scale much lower than the resolution limit of visible light microscopy (~250μm) can be observed using the FRET phenomenon. This technology has been utilized to create genetically encoded fluorescent protein biosensors. In a two-fluorophore FRET biosensor design, a donor FP is coupled with an acceptor FP (such as CFP and YFP) with a linker region. This linker region is designed to undergo conformational changes based on some cellular event that can increase or decrease FRET efficiency of the two FPs. Measurable outputs are numerous depending on the donor and acceptors. For example, measuring the ratio of donor to acceptor emission or the fluorescence lifetime of the donor fluorophore are two common, popular methods to measure changes in the FRET efficiency. Therefore, the FRET output can be used as a real-time sensor of some cellular event, such as kinase activity. In contrast, traditional protein assays, such as ELISA or Western immunblotting, require cell lysates and therefore suffer from the lack of an ability to monitor changes in kinase activity real-time. Perhaps the most successfully implemented FP-based FRET biosensor is the family of “Cameleons”

(Miyawaki, Llopis et al. 1997), which can detect increases in intracellular calcium ion concentration. The linker region consists of the calcium-binding region calmodulin (CaM) and a CaM binding domain (M13) domain from myosin light chain kinase (MLCK). Changes in calcium ion concentration cause conformational changes in the CaM-M13 linker region and changes the FRET efficiency of the donor and acceptor.

An advantage of using genetically encoded biosensors is the ability to target subcellular regions using localization tags. Short amino acid sequences can be added to the biosensor to traffic the biosensor to specific organelles, such as the mitochondria, plasma membrane, lipid rafts, endoplasmic reticulum (ER), and nuclear membrane. For instance, the calcium concentration ($[Ca^{+2}]$) of the ER and mitochondria can be measured using ER and mitochondrial localization sequences tagged to the Cameleon biosensor (Arnaudeau, Frieden et al. 2002). In contrast, organic calcium dyes such as the fluo, indo, and fura series of calcium indicators, while having shown great success in measuring cytoplasmic intracellular calcium concentration ($[Ca^{+2}]_i$), cannot be targeted to specific intracellular organelles.

1.1.6 Side-View Imaging

Traditional inverted fluorescent microscopy has limitations in axial resolution and has hindered the ability to posit questions on height-dependent cellular behavior. A promising technique to obtain additional spatial information while maintaining a high temporal resolution is to view the cell from the side. Imaging cells in side-view has been pursued by several research groups, as it represents a relatively simple add-on to the traditional inverted microscope that is present in almost all biological laboratories. Imaging cells in side-view has been used in several applications, including cell

adhesion/detachment (Cao, Usami et al. 1997; Dong, Cao et al. 1999; Leyton-Mange, Yang et al. 2006) and atomic force microscopy (Chaudhuri, Parekh et al. 2009). However, these studies sacrificed the ability to also simultaneously image the traditional inverted microscope-based bottom-view, which would provide additional spatial detail. More recent innovations have pushed side-view imaging to provide simultaneous dual-orthogonal plane imaging (Juette, Gould et al. 2008; Tang, Akerboom et al. 2010). The unique advantages of each of these side-view imaging techniques represent a new platform to be able to observe novel spatial or temporal dynamics of cellular processes.

1.2 Specific Aims and Organization

1.2.1 Specific Aims

To guide our effort, the following specific aims and hypotheses are proposed:

Hypothesis H_1: The dynamics of deformation of the actin and microtubule cytoskeletal networks in single osteocytes under steady and oscillatory fluid flow are spatiotemporally distinct between the networks and between flow profiles.

Specific Aim 1a: Develop a multi-channel quasi-3D imaging technique with adequate spatiotemporal resolution to capture the millsecond-scale 3D deformations of intracellular cytoskeletal networks under dynamic fluid shear loading.

Specific Aim 1b: Simultaneously track and analyze actin filament networks and microtubule networks using multi-channel quasi-3D imaging of single MLO-Y4 osteocytes under steady and dynamic oscillatory fluid flow to directly compare the 3D spatiotemporal development of strains between the two cytoskeletal networks.

Hypothesis H_2: Osteocytes utilize fluid shear flow-induced $[Ca^{+2}]_i$ oscillations to activate $[Ca^{+2}]_i$-dependent actomyosin contractions through a muscle-like mechanism.

Specific Aim 2: Simultaneously track and analyze actin filament networks and $[Ca^{+2}]_i$ in single MLO-Y4 osteocytes over time to observe the spatiotemporal effects of $[Ca^{+2}]_i$ on actin strain.

1.2.2 Organization

The framework of this thesis consists of three major concentrations: (1) the development and validation of a multi-channel quasi-3D microscopy technique to enable observations of cellular events at a high spatiotemporal resolution, (2) the application of the novel technique to investigate the mechanics of osteocyte actin and microtubule cytoskeletal networks under physiologically relevant fluid flow profiles, and (3) the application of the technique to observe the effects of $[Ca^{+2}]_i$ oscillations on the osteocyte actin cytoskeletal network.

The study presented in Chapter 2 develops the single-channel quasi-3D technique and, as a proof of principle, applies it to investigate the strain development of the actin and microtubule networks under steady fluid shear flow. The image processing techniques to calculate intracellular strains are developed and validated for both networks. Additional imaging and mechanical validation studies are carried out in Appendix A. Cell shape changes are measured by reconstructing a quasi-3D cell shape using 2D plasma membrane images. Depolymerization of the actin and microtubule cytoskeletal networks demonstrate subcellular mechanical interplay between the two networks dependent on the flow directionality. Intercellular heterogeneities suggest the necessity of tracking both cytoskeletons simultaneously.

The study presented in Chapter 3 further refines the quasi-3D technique developed in Chapter 2 to introduce multi-channel image collection. Quadview beamsplitters are incorporated into the microscopy design to allow simultaneous acquisition of up to 4 separate fluorescent channels. This new technique is utilized to track both the actin and microtubule networks in the same cell under steady and oscillatory fluid shear flows to allow paired comparisons between the networks. Viscoelastic and elastic effects are observed in both networks under steady and oscillatory flows, respectively. The actin networks display higher deformations under oscillatory flow, demonstrating that the actin networks are more responsive under physiological levels of loading.

The study in Chapter 4 incorporates FRET biosensors and fully utilizes the strengths of the multi-channel quasi-3D imaging technique. The acquisition of three fluorescent dyes is optimized to obtain $[Ca^{+2}]_i$ and actin strains simultaneously in a single cell. Actomyosin contractions dependent on smooth muscle myosin are discovered to occur in osteocytes when $[Ca^{+2}]_i$ spikes are induced by a variety of stimuli. The presence of smooth muscle proteins are verified using western blots and drug inhibition studies. Possible downstream pathways of osteocyte actomyosin contractility are posited for future studies.

Chapter 5 presents the conclusion of this thesis work and suggestions for future studies related to osteocyte mechanics and mechanotransduction.

Chapter 2. Quasi-3D Cytoskeletal Dynamics of Osteocytes under Fluid Flow

2.1 Introduction

Osteocytes are three-dimensional (3D), ellipsoidal, mature bone cells encased in mineralized extracellular matrix. Abundant evidence has shown that the osteocytes are the key mechanonsensors in bone that directly regulate bone-forming osteoblast and bone-removing osteoclast activities (Tatsumi, Ishii et al. 2007; Taylor, Saunders et al. 2007; You, Temiyasathit et al. 2008). It has been hypothesized that the dominant loading mechanism of the mechanosensing osteocytes is oscillating fluid shear stress resulting from the mineralized matrix deformation of bone (Jacobs, Yellowley et al. 1998). Most *in vitro* fluid shear studies on primary osteocytes and osteocyte cell lines have focused on monolayers of flat, spread osteocytes, but the *in vivo* shape of osteocytes is ellipsoidal or spherical (Vatsa, Breuls et al. 2008). *In vitro* experiments have demonstrated that osteocytes are more mechanosensitive in this 3D configuration than when flat and spread (Bacabac, Mizuno et al. 2008). Recent experimental and theoretical evidence suggest the existence of subcellular location-dependent responsiveness to fluid shear in the osteocyte (Wang, McNamara et al. 2007; Adachi, Aonuma et al. 2009). However, the 3D intracellular deformation and mechanics of an osteocyte under fluid flow is poorly characterized. The conventional bottom-view two-dimensional (2D) microscopy to view an ellipsoidal osteocyte cell is insufficient to characterize the intracellular deformation of the adhered cells at their apical surface and at their basal surface under flow (Helmke, Rosen et al. 2003).

The actin and microtubule (MT) cytoskeletons have been shown to play an important role in the osteocyte's biochemical response to fluid shear loading (Ajubi, Klein-Nulend et al. 1996; Ponik, Triplett et al. 2007). Mechanical interactions between the two networks have profound effects on the behavior of each individual network (Brangwynne, MacKintosh et al. 2006). Reconstituted cytoskeleton studies have investigated how mechanical coupling affects each network's mechanical properties (Brangwynne, Koenderink et al. 2008), but studies in live cells are lacking. Recent evidence has established the importance of studying the mechanics of whole, aggregate cytoskeletal networks in the context of a living cell, rather than just of individual filaments (Fletcher and Mullins 2010). For example, network deformation of MTs has been shown to be a direct mediator in the spatial activation of Src in smooth muscle cells (Na, Collin et al. 2008). Furthermore, this activation occurred on the millisecond timescale after mechanical stimulus, emphasizing the importance of the initial deformational events. Therefore, network deformational dynamics of the actin and MT cytoskeletons and their interactions under mechanical loading by fluid shear deserve further characterization and study.

Traditional techniques to obtain 3D images of a cell-body, such as confocal or deconvolution microscopy, are inherently timescale-limited due to the necessity of scanning a z-stack. Obtaining sufficient 3D osteocyte information using a laser scanning confocal microscopy takes approximately .5 to .8 seconds. This imaging frequency would drastically undersample the instantaneous deformational responses of bone cells, especially under physiological oscillatory flow profiles (Kwon and Jacobs 2007). A promising technique to obtain additional spatial information while maintaining a high

temporal resolution is to view the cell from the side. Imaging cells in side-view has been used in several applications, including cell adhesion/detachment (Cao, Usami et al. 1997; Dong, Cao et al. 1999; Leyton-Mange, Yang et al. 2006) and atomic force microscopy (Chaudhuri, Parekh et al. 2009). However, these studies were not capable of simultaneously imaging the traditional inverted microscope-based bottom-view at either a high spatial or temporal resolution.

In this study, we used a "quasi-3D" imaging system to simultaneously image two orthogonal planes, the traditional bottom-view plane and a side-view plane, of a single osteocyte under fluid flow. The limitations of traditional bottom-view 2D microscopy were overcome to obtain far more spatial information than previously possible. This quasi-3D system avoided the use of z-stack raster-scanning of confocal microscopy, allowing the temporal resolution to be limited only by camera frame rate. The objectives of this study were to: (1) develop a quasi-3D microscopy system to allow the simultaneous bottom- and side-view visualization of a single cell under fluid flow, (2) visualize osteocyte actin or microtubule networks along with the whole-cell shape under fluid shear; and (3) compare the network deformation of actin and microtubule networks and characterize their mechanical interactions.

2.2 Methods

2.2.1 Microscope/Quasi-3D Imaging

A custom-designed dual-microscope system consisting of an IX-71 inverted microscope and a BX-2 upright microscope (Olympus America Inc., Center Valley, PA) was utilized in this study. A custom-built holder aligned a 45° mirror in the light path

(Cao, Usami et al. 1997; Cao, Donell et al. 1998) of the upright microscope to obtain "side-view" images of a single cell, while the inverted microscope obtained regular "bottom-view" images of the same cell simultaneously (Fig. 2.1 A). The cell was imaged in a glass tube with a square cross-section (Vitrocom, Mountain Lakes, NJ), which provided perpendicular glass planes for high-resolution imaging and also served as a fluid flow chamber. Both microscopes used 60X LUCPLNFLN long working distance objective lenses (Olympus America Inc.). A Lambda DG-4 xenon light source (Sutter, Novato, CA) attached to the inverted microscope was used to switch between 2 excitation filters (Semrock, Rochester, NY) to excite either GFP (475/35) or Alexa Fluor 594 (580/23). The xenon lamp output was attenuated by 50%, and an additional 50% neutral density filter was used to minimize phototoxicity of the cells. Dual-bandpass emission filters for GFP and Alexa Fluor 594 emissions (527/42 and 645/49) and corresponding dichroics in each microscope filtered the appropriate light bands, and ORCA-AG interline CCD cameras (Hamamatsu, Japan) with 2x2 binning in each microscope captured and recorded the emissions. The resultant image resolution was .215 μm/pixel. MetaMorph 7.6.2 software (Danaher Corp., Washington, DC) controlled and synchronized the switching of the excitation filters at the light source and the two cameras' acquisition to sequentially obtain GFP and Alexa Fluor 594 emission images at 6 Hz each for a total frame rate of 12 Hz.

2.2.2 Cell Culture

MLO-Y4 osteocyte-like cells (a gift from Dr. Lynda Bonewald of the University of Missouri-Kansas City) were grown in α-MEM medium supplemented with 5% fetal bovine serum and 5% calf serum. Cells were transiently transfected with either EGFP-

actin (Clontech, Mountain View, CA) or GFP-ensconsin microtubule binding (EMTB) domain (a gift from Dr. Chlöe Bulinski of Columbia University) (Faire, Waterman-Storer et al. 1999) plasmids to visualize actin or microtubule networks. Transfection was performed using Lipofectamine PLUS (Invitrogen, Carlsbad, CA) according to manufacturer's instructions.

2.2.3 Cytoskeletal Inhibitor Studies

There were 4 groups in this study. The "Actin" group was transfected with EGFP-actin, and the actin network was tracked over time (n=7). The "Actin+Colchicine" group was transfected with EGFP-actin and incubated with 6μM colchicine (Sigma-Aldrich, St. Louis, MO) to disrupt the MT network, and the actin network was tracked over time (n=7). The "MT" group was transfected with GFP-EMTB, and the MT network was tracked over time (n=7). The "MT+cytoD" group was transfected with GFP-EMTB and incubated with 3μM cytochalasin D (cytoD) (Sigma-Aldrich) to disrupt the actin network, and the MT network was tracked over time (n=7).

2.2.4 Flow Experiments

Number 1 thickness glass slides (Fisher Scientific, Waltham, MA) were cut into thin "microslides" to fit into the flow chamber using a laser cutter (Universal Laser Systems, Scottsdale, AZ). Cells were trypsinized 24 hours after transfection and plated on the microslides for 20 minutes. Microslides were then incubated in growth medium with or without inhibitors for an additional 20 minutes, depending on their assigned cytoskeletal inhibitor group. Microslides were finally incubated in 5μg/mL wheat-germ agglutinin Alexa Fluor 594 (Invitrogen) in Hank's buffered saline solution for 5 minutes to stain the plasma membrane and then placed in a glass tube to form a flow chamber.

Plating time was chosen to ensure fully attached, rounded osteocytes without cellular processes (Takai, Landesberg et al. 2006; Bacabac, Mizuno et al. 2008).

A syringe pump (New Era Pump Systems, Wantagh, NY) and gastight syringe (Hamilton, Reno, NV) were used to provide three loading cycles of 10 seconds of steady fluid flow that generated a shear stress of 10 dynes/cm^2 on the apical surface of the osteocytes with a 10 second rest period in-between each cycle.

Non-flowed control groups of Actin (n=3) or MT (n=3) tracked cells were prepared and imaged in the same manner as the flowed groups to measure the baseline amount of cytoskeletal network reorganization and/or movement.

2.2.5 Immunocytochemistry and Confocal Imaging

To visualize the location of the actin and MT networks in rounded osteocytes, cells were plated in a similar manner as the flow experiment setup. Cells were fixed with 3.7% formaldehyde (Sigma-Aldrich) in phosphate buffered saline and permeabilized with .1% Triton-X 100 (Sigma-Aldrich). A 1% bovine serum albumin (Sigma-Aldrich) block was followed by incubation with a primary antibody for β-tubulin (Sigma Aldrich) and an Alexa Fluor 488 secondary antibody (Invitrogen) to visualize the MT network. The cells were then counterstained with rhodamine phalloidin (Invitrogen) to visualize the actin network. Cells were imaged using a 100X oil immersion lens on a laser scanning confocal microscope (Leica Microsystems GmbH, Wetzlar, Germany) with Ar and HeNe lasers and a prism spectral detector tuned for appropriate emission channels.

2.2.6 Image Analysis

All raw images were first processed in MetaMorph 7.6.2. Bottom-view and side-view intensity images of the cytoskeleton and plasma membrane images were first

processed with a background intensity subtraction using the average pixel intensity of a region in each image away from the cell and then further with a 3 pixel by 3 pixel median filter.

Each cytoskeletal image over time was processed further using the digital image correlation technique (Sutton, Cheng et al. 1986). A normalized cross-correlation algorithm (Lewis 1995) was used to track 16x16 pixel subregions of each image with a center-to-center spacing of 2 pixels against the original image with a zero-order approach using the Image Processing Toolbox in MATLAB 7.8 (The Mathworks, Natick, MA). The subregion size and center-to-center spacing were determined by simulating rigid body displacement of sample cytoskeletal images and obtaining an accuracy of >99.5% and a standard deviation of < .2 pixels of the simulated displacement (Bae, Lewis et al. 2006).

The resulting x-y (for bottom-view) and x-z (for side-view) displacement fields (see axis definitions in Fig. 2.1 B) were each first smoothed using a 5-point moving average across the time dimension for each pixel. The displacements fields were then smoothed and differentiated using a 5x5 2D Savitsky-Golay bilinear least squares filter (Pan, Xie et al. 2007). Finite Lagrangian strain fields were then calculated from the differentiation fields (3 bottom-view strains: Eyy, bottom-view Exx, Exy; 3 side-view strains: Ezz, side-view Exx, Exz) (Wang, Deng et al. 2002). Points within 2 pixels of the edges of the cell were discarded from the analysis due to the square filtering process used. The strain error in the actin images undergoing simulated rigid body displacement was 0.0192 ± 0.0268 (%). Similarly, the strain error from MT images was -0.0021 ± 0.0287 (%). The calculated strain error on simulated stretch images was less than 0.3%.

Each plasma membrane image over time was also processed to obtain whole-cell volume, as outlined in Fig. 2.1 C. The initial bottom-view and side-view images were thresholded to obtain the points corresponding to the cell membrane boundary. Each point in the outline was tracked over time using the same digital image correlation technique as above. The tracked membrane boundaries in the two views for each timepoint were oriented in 3D space and then fit to a spline function in Solidworks (Dassault Systèmes, Concord, MA). The cell boundary skeleton was then filled using a lofting algorithm in Solidworks, and volume was obtained, taking advantage of the almost rounded osteocyte shape.

2.2.7 Statistics

All statistics were performed using NCSS 2007 software (NCSS LLC, Kaysville, Utah). Due to the large variability between cells, repeated measures analysis of variance (ANOVA) tests were utilized when appropriate to compare multiple groups. For whole-cell average strain results, peak strain values at the end of each loading period and residual strains values at the end of each unloading period for all 6 strain components were collected from each sample. One-tailed t-tests were run to determine if the average strain values were tensile or compressive. The significance level, α, was set at 0.05. A repeated measures ANOVA for each strain parameter with cycle number as a within-subject factor was performed, and a *post-hoc* Tukey-Kramer test was run to determine significance between loading cycles. The Geisser-Greenhouse correction was utilized in the ANOVA when the sphericity assumption was violated. A one sample t-test of the linear slopes of the peak and residual Exx between side and bottom views for each cell

was performed to investigate the differences between the two views' Exx, which were measured simultaneously, but separately, in both views.

To compare subcellular strains, each cell was divided into various subcellular regions, by subcellular thirds in both views, *i.e.*, the leading, middle, or trailing thirds of the cell, or by subcellular height in side-view, *i.e.*, the apical, mid-height, and basal heights (Fig. 2.1 B). Strains in each location were averaged. An ANOVA with one between-subjects factor (inhibitor) and two within-subjects factors (subcellular region, cycle number) was run between the Actin and Actin+Colchicine groups, and between the MT and MT+cytoD groups. The interactions involving the subject factor were pooled into one error term to achieve more power in the F-tests. *Post-hoc* Tukey-Kramer multiple comparison tests were run to determine significance of factors and interactions.

2.3 Results

2.3.1 Whole-Cell Dilatation

The whole-cell dilatation as measured by the plasma membrane-based cell volume over time was less than 3% in all 4 groups (Fig. 2.2). This suggested that osteocytes were almost incompressible at the shear loading level that was applied. No statistical difference was seen between the 4 groups' whole-cell volume change over time.

2.3.2 Cytoskeletal Network Deformation

Sample images of the actin and microtubule networks before and after flow are shown in Fig. 2.3. Sample whole-cell actin network strain traces over time are provided in Fig. 2.4, B and D. Whole-cell MT network strain traces over time are provided in Fig. 2.5, B and D. Cells showed creep behavior from the loading and relaxation periods in

both networks in both bottom and side views. The strain profiles are clearly time-dependent, emphasizing the necessity of a high temporal resolution to fully capture the instantaneous and short-term behavior of cells under mechanical loading.

Interestingly, shear strain was only seen in side-view: bottom-view shear Exy in most cells hovered near zero while shear Exz in side-view showed significant creep and creep recovery. Side-view strains that measured height (Ezz), flow-directional (side-view Exx), and shear deformations were on the same order of magnitude as the bottom-view strains. These results highlight the 3D deformational behavior of osteocytes under fluid flow in both actin and MT networks.

Actin strain contour plots at the end of the first loading period are provided in Fig. 2.4, C and E. MT strain contour plots are provided in Fig. 2.5, C and E. Fine-grain heterogeneity of the high compressive or tensile strains varied between individual cells, emphasizing the variability of cellular mechanical properties and cytoskeletal network distribution at the single-cell level. No statistical difference was seen between bottom-view Exx and side-view Exx, although they were separate, independent measurements.

Non-loaded actin and MT network strains magnitudes were 0.4% or lower after a mock 65 second flow period (Table 2.1), demonstrating that cytoskeletal rearrangement and movement at the network scale was relatively insignificant over the given time period.

Actin and MT networks were distributed perinuclearly in rounded osteocytes (Fig. 2.10). Actin networks were predominantly cortically distributed and immediately outside the nucleus, while MT networks were more diffusely spread throughout the cell.

2.3.3 Whole-Cell Actin Strains

Whole-cell average strains for the actin-tracked networks treated with or without colchicine to disrupt the microtubules are summarized in Fig. 2.6. Overall, the peak strains in the untreated Actin group were almost always tensile, and the residual strains were always lower than the peak strains. Peak and residual strains tended to increase with cycle for most strains. No trend for Eyy was seen in the Actin group (Fig. 2.6 A). For side-view Exx (Fig. 2.6 B), Exz (Fig. 2.6 D) and Ezz, (Fig. 2.6 C), the residual strains were tensile, suggesting that the relaxation period was insufficient for the actin network to return to its original state, highlighting the viscoelastic nature of the actin network.

The effect of MT disruption on actin network strains was varied, with some cells having compressive whole-cell peak strains, but no consistent trend among the cells in the Actin+Colchicine group. Addition of colchicine caused the Eyy peak strains to be tensile over all loading cycles (Fig. 2.6 A). An effect of colchicine was clearly seen in Ezz (Fig. 2.6 C). While peak and residual Ezz in the Actin group were tensile, strains in the Actin+Colchicine group were not different than zero, because some cells in this group had compressive whole-cell Ezz.

2.3.4 Whole-Cell Microtubule Strains

Whole-cell average strains for the MT-tracked networks treated with or without cytoD to disrupt the actin are summarized in Fig. 2.7. The untreated MT peak and residual strains were tensile and the residual strains increased with cycle, suggesting the cells were not able to fully recover in the given relaxation period. This tensile, viscoelastic effect was more apparent than in the actin networks.

Actin disruption by cytoD abolished this effect in the MT+cytoD bottom-view Exx (Fig. 2.7 A). The other strains (Fig. 2.7, B, C, and D) remained mostly unaffected by the actin disruption, however.

2.3.5 Subcellular Cytoskeletal Strains

The side-view thirds strain distributions and effects of cytoskeletal disruption are summarized in Fig. 2.8. In the actin networks, regional strain field heterogeneity was seen in Exx and Exz (Fig. 2.8, B and C). The effects of MT disruption were greatest in the leading edge to flow in Ezz and side-view Exx strains, and strain field heterogeneity was lost in Exx (Fig. 2.8, A and B). MT disruption had no effect on the Exz strain field distribution (Fig. 2.8 C).

In the MT networks, regional strain field heterogeneity was only seen in Exz (Fig. 2.8 F). MT Exx increased in the leading edge, but decreased in the trailing edge when actin was disrupted (Fig. 2.8, E). Actin disruption caused MT Exz to increase in the middle of the cell, and strain field distribution heterogeneity was lost (Fig. 2.8 F). No effect was seen in MT Ezz (Fig. 2.8 D).

The strain distributions for different heights of the cell in side-view are summarized in Fig. 2.9. Actin Exx and Exz were highest in the mid-height of the cell (Fig. 2.9 B and C). MT disruption lowered the actin Ezz strain in the mid-height and basal regions of the cell (Fig. 2.9 A) and the actin Exx strain in the mid-height (Fig. 2.9 B). Interestingly, Exz was similar in both actin and MT networks (Fig. 2.9, C and F), and disruption of either network did not affect the regional strain field heterogeneity.

In summary, the normal Ezz and Exx strains were heterogeneously distributed regionally in the actin networks, but not in the MT networks. Shear Exz was similar in

both actin and MT networks, showed distinct patterns, and was relatively insensitive to disruption of the counterpart's network.

2.4 Discussion

Deformation of the cell and of intracellular cytoskeletal structures under fluid flow has been shown to be spatially heterogeneous, time-dependent, and height-dependent (Ueki, Sakamoto et al. ; Helmke, Rosen et al. 2003; Knight, Bomzon et al. 2006; Kwon and Jacobs 2007; Sato, Suzuki et al. 2007). Using the quasi-3D imaging technique, osteocytes were successfully imaged in two orthogonal planes under fluid flow at a frame rate sufficient to observe the transient, instantaneous mechanical behaviors of the cytoskeletal networks and of the whole-cell shape. The high temporal resolution of the system allowed the viscoelastic mechanical behavior to be characterized. To our knowledge, this is the first study to simultaneously investigate the Eyy, Exx, Exy, Ezz, and Exz strain components as measured by cytoskeletal network deformations. The novel side-view observations emphasize the 3D deformational behavior under fluid flow. Shear deformation was visible only in sideview: while bottom-view shear Exy was negligible, side-view shear Exz was on the same order of magnitude as the flow-directional strains. Furthermore, the quasi-3D technique is not limited to only the osteocyte cell type as studied here, but its versatility allows it to be used in other cell mechanics studies requiring spatiotemporal resolution, such as viewing endothelial cells or the primary cilia under fluid flow.

The plasma membrane dye showed that the cells did not experience a significant amount of dilatation under flow, demonstrating low cellular compressibility under

physiological levels of loading. A previous study found highly compressible whole-cell behavior but only at very high supraphysiological levels of shear loading (Ofek, Wiltz et al. 2009).

At the whole-cell level (Figs. 2.6 and 2.7), the actin and MT networks behaved as viscoelastic materials undergoing primarily tensile creep and creep recovery behaviors similar to most biological materials. Actin and MTs have generally been considered as pre-stressed tension and compression elements, respectively, when the cell is in an equilibrium, resting state (Ingber 2003). MTs have been shown to act as compression struts to balance the tensile actin pre-stresses inside a cell (Stamenovic, Mijailovich et al. 2002). This study focused on the dynamic, load-induced deformation of these two networks and showed that the MT network can experience tensile incremental strains under fluid flow in relation to its equilibrium, baseline pre-stressed state. Residual strains after the 10 second relaxation periods were more prevalent in the MT networks than in the actin networks, agreeing with previous studies in the timescales of recovery in reconstituted cytoskeletal network studies (Humphrey, Duggan et al. 2002; Lin, Koenderink et al. 2007).

Subcellularly, actin cytoskeletal peak normal strains decreased in the leading edge to flow and closer to the coverslip when the MT network was disrupted (Figs. 2.8, A and B, and 2.9, A and B). This suggests that removing the MT networks increases cell stiffness and is reflected in the apparent stiffness of the actin network, possibly through a pre-stress mechanism (Wang, Naruse et al. 2001; Wang, Tolic-Norrelykke et al. 2002; Park, Tambe et al. 2010). The role of MT networks in cell stiffness in the literature is varied, however (Trickey, Vail et al. 2004; Takai, Costa et al. 2005; Ofek, Wiltz et al.

2009). MT removal has been shown in some cases to increase cell stiffness through this actin pre-stress balancing mechanism (Stamenovic, Liang et al. 2002). Surprisingly, actin disruption had little effect on the MT network strain (Figs. 2.8 and 2.9).

An interesting finding of this study is that these cytoskeletal changes are location specific in the osteocyte cytoskeletal networks and are not reflected in the whole-cell strains. Interestingly, actin network displacement was not different in the leading and trailing edges in a previous study on endothelial cells (Mott and Helmke 2007), but those effects were viewed minutes after the onset of flow. A longer term study in endothelial cells showed the stiffness at the leading edge of flow was higher than at the trailing edge after 6 hours of flow, and this was due to actin network rearrangement (Sato, Suzuki et al. 2007). This emphasizes the time-dependent interactions between the flow field and the cytoskeletal networks. The effect of the transient, location-dependent strain patterns on biochemical outputs remains to be seen, however.

A tradeoff to the high temporal resolution was the loss of optical sectioning of the images. The ~ 1.3 μm depth of field of the quasi-3D system was confounded by the presence of out-of-focus fluorescent dye from neighboring planes. Consequently, the tracked displacements and resultant strains of the bottom-view and side-view came from images that were an average of cellular features in neighboring planes related by the point spread function. The measured strains therefore represent more of an average through many planes rather than of an individual thin slice of the cell.

Tracking the network deformations rather than individual fibers diminished the likelihood of obtaining erroneous strains based on individual filament rearrangement and Brownian motion, because the digital image correlation technique tracked textures of the

naturally occurring gradients of the cytoskeletal network. Tracking textures also lessened the impact of the presence of soluble G-actin, which were not associated with the F-actin networks and can account for up to one half of the actin in a cell (Alberts 2008). However, the contribution of small G-actin monomers to the gradients in texture of large cytoskeletal networks is presumably low. This limitation was less important in the MT tracked groups, because the GFP-fusion to the EMTB domain (Faire, Waterman-Storer et al. 1999) bound to MT filaments and not individual tubulin monomers.

The results from the quasi-3D imaging technique have demonstrated the necessity of characterizing the complex spatiotemporal behavior of osteocyte cytoskeletal networks under fluid flow. Future work in correlating the heterogeneous strain deformations to biological outputs, such as mechanosensitive protein kinase activation, will help give greater understanding to the initial events of mechanotransduction from fluid flow. This technique will prove useful in imaging more dynamic, physiological fluid flow profiles, *e.g.* oscillatory fluid flow at 1 Hz, where z-stack scanning techniques will inevitably be unable to accurately image a 3D cell over the flow profile.

2.5 Tables

Actin Strain Component	@ 30 seconds, mean whole cell strain	@ 65 seconds, mean whole cell strain
Eyy	0.000498 ± 0.00094	0.000477 ± 0.000961
Exx, bottom-view	-0.000479 ±0.00105	0.000764 ± 0.00458
Exy	0.000598 ± 0.00049	0.00154 ± 0.00146
Ezz	-0.000969 ± 0.00138	-0.00410 ± 0.00202
Exx, side-view	0.00153 ± 0.00188	0.00460 ± 0.00183
Exz	-0.000580 ± 0.00125	-0.000384 ± 0.00311

MT Strain Component	@ 30 seconds, mean whole cell strain	@ 65 seconds, mean whole cell strain
Eyy	-0.000638 ± 0.00136	0.00138 ± 0.00279
Exx, bottom-view	-0.00183 ± 0.00158	-0.00328 ± 0.00124
Exy	0.000714 ± 0.00212	0.000198 ± 0.00511
Ezz	-0.00137 ± 0.00569	-0.000614 ± 0.00162
Exx, side-view	0.00344 ± 0.00422	0.00482 ± 0.0102
Exz	-0.00535 ± 0.00276	-0.00814 ± 0.00607

Table 2.1: Actin and MT strains static whole-cell strains after 30 and 65 seconds of imaging. Cytoskeletal rearrangements in this time scale had a low contribution to the whole-cell strains compared to flow-induced strain magnitudes.

2.6 Figures

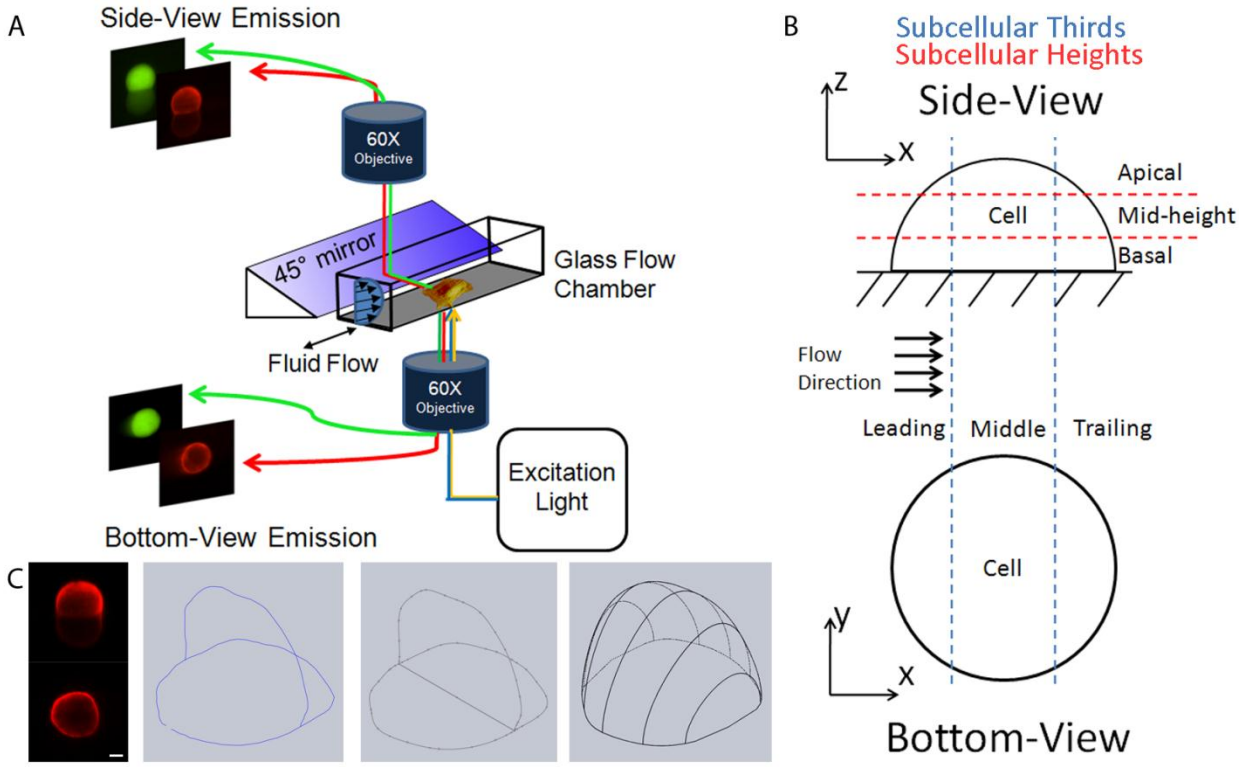

Figure 2.1: (A) Schematic of quasi-3D microscopy system. (B) Axes for bottom-view and side-view images defined. Subcellular location divisions are depicted. Subcellular thirds of leading, middle, and trailing thirds for bottom- and side-view are in blue lines, and subcellular heights for side-view are in red lines. (C) Schematic of conversion of cell plasma membrane boundaries from side-view and bottom-view to get a whole-cell volume. Boundary points tracked by digital image correlation are fit to a spline function and then lofted into a 3D shape. Scale bar is 5 μm.

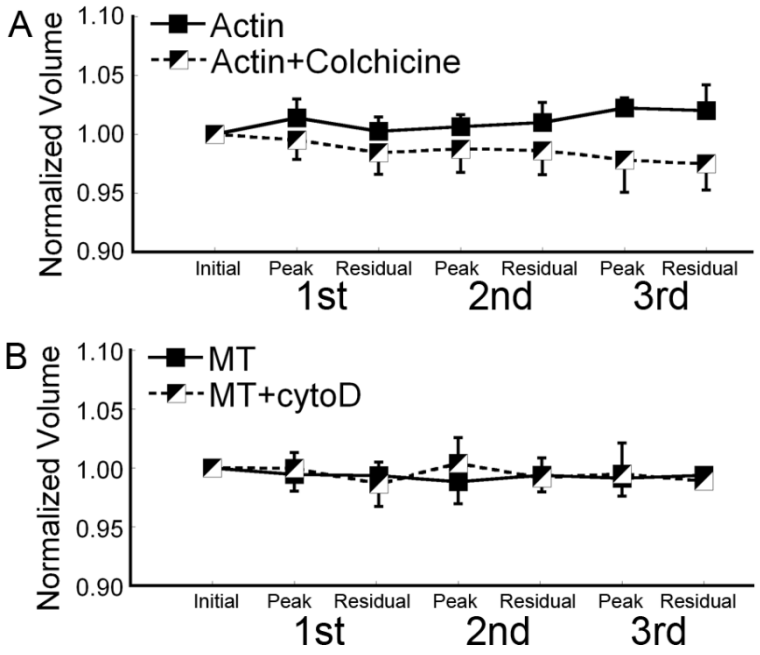

Figure 2.2: Whole cell volume change over time for (A) Actin tracked groups and (B) MT tracked groups. No significant differences were observed. Error bars are standard deviations.

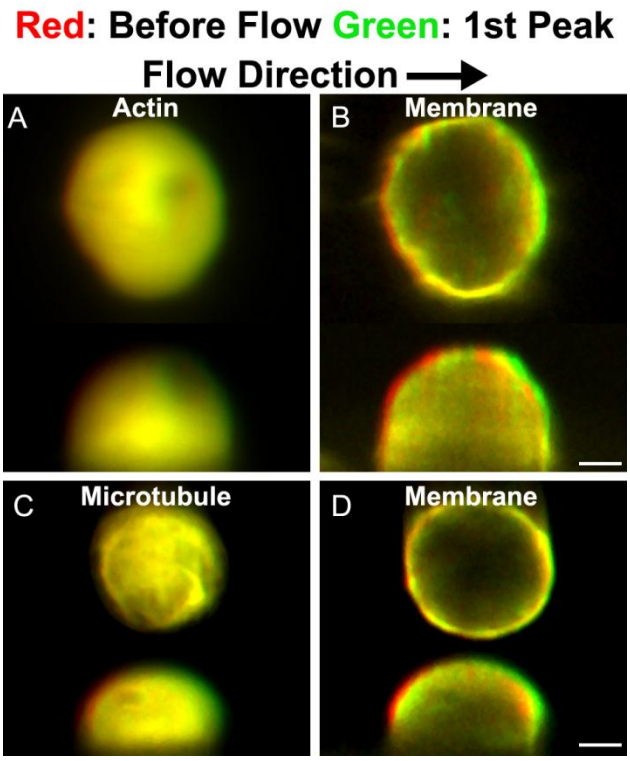

Figure 2.3: Merged fluorescent images of cells before (red) and after first loading period (green) in quasi-3D. Osteocyte transfected to visualize either actin or microtubules and counterstained with (B,D) plasma membrane dye. Flow-induced deformation is apparent in side-view in both dyes. Scale bar is 5 μm.

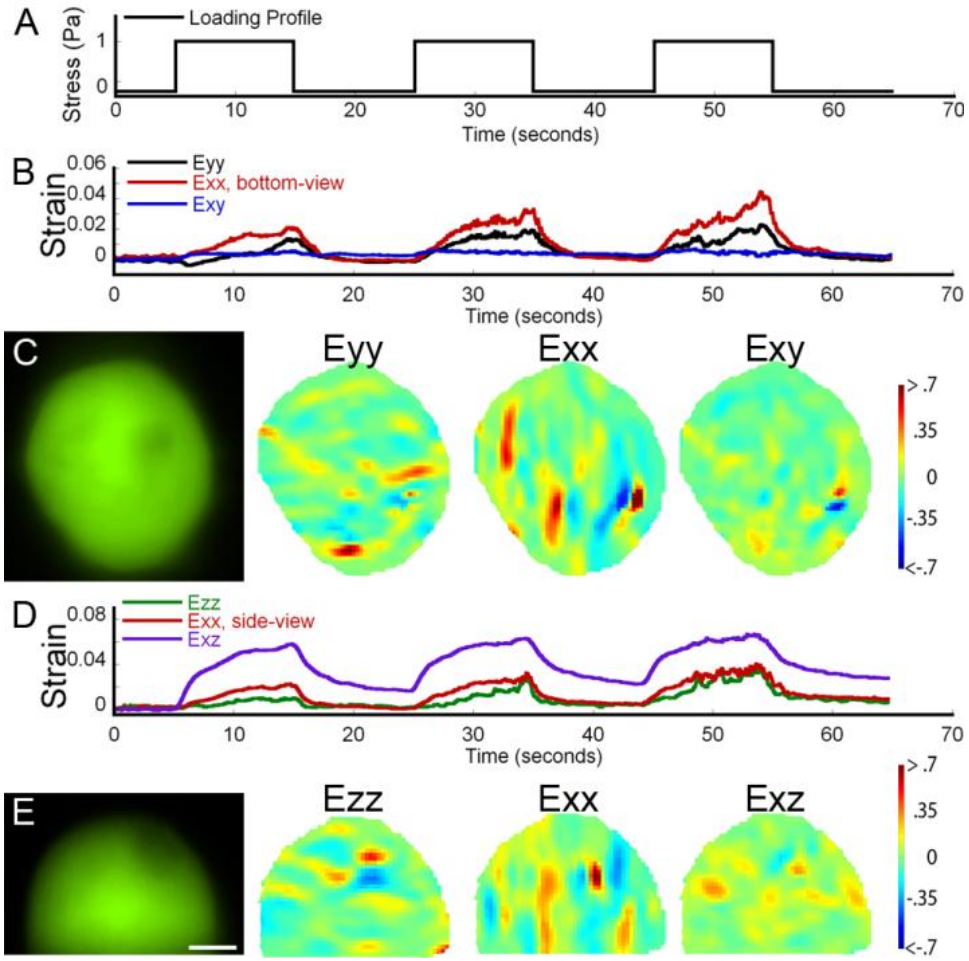

Figure 2.4: Actin network strain traces and contour plots for a sample osteocyte. (A) Flow pattern. (B) Sample trace of Eyy, Exx, and Exy of the osteocyte obtained in bottom-view. (C) Bottom-view image of the osteocyte in (B) and strain contour plots from the first peak. (D) Sample trace of Ezz, Exx, and Exz of the osteocyte obtained in side-view. (E) Side-view image of the osteocyte and strain contour plots from the first peak. Scale bar is 5 μm.

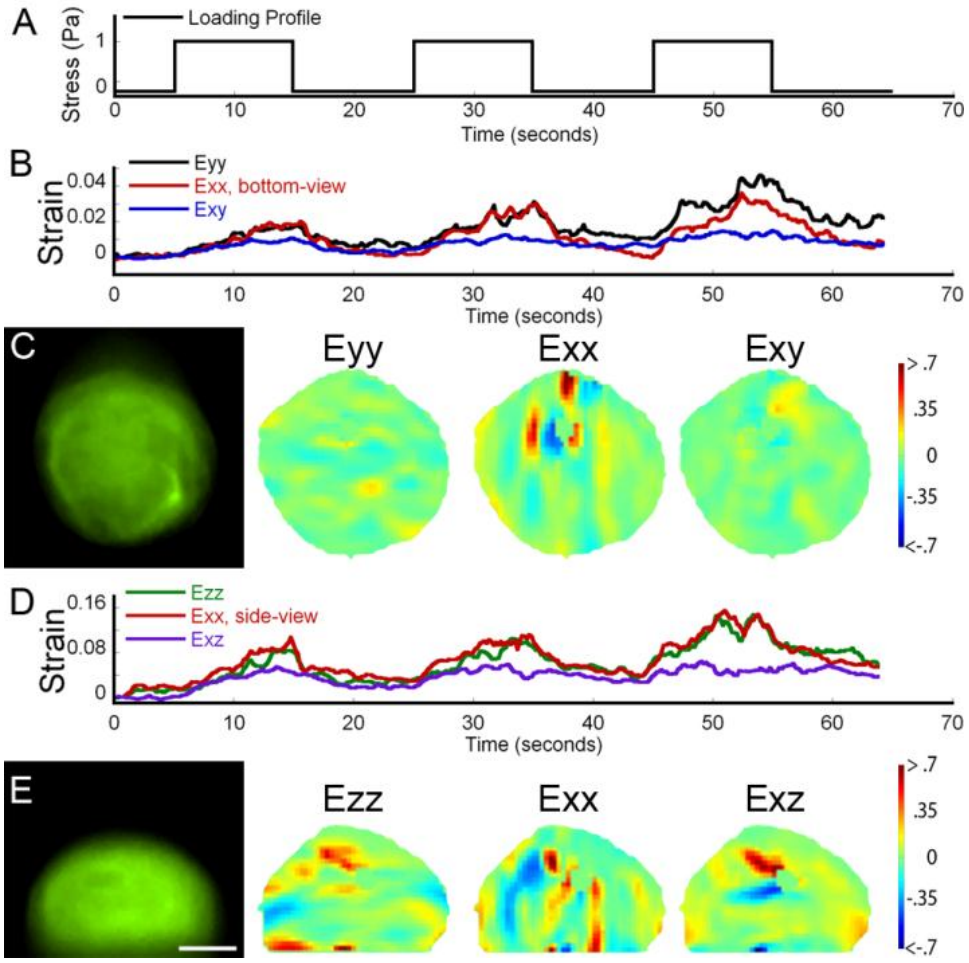

Figure 2.5: Microtubule network strain traces and contour plots for a sample osteocyte. (A) Flow pattern. (B) Sample trace of Eyy, Exx, and Exy of the osteocyte obtained in bottom-view. (C) Bottom-view image of the osteocyte in (B) and strain contour plots from the first peak. (D) Sample trace of Ezz, Exx, and Exz of the osteocyte obtained in side-view. (E) Side-view image of the osteocyte and strain contour plots from the first peak. Scale bar is 5 μm.

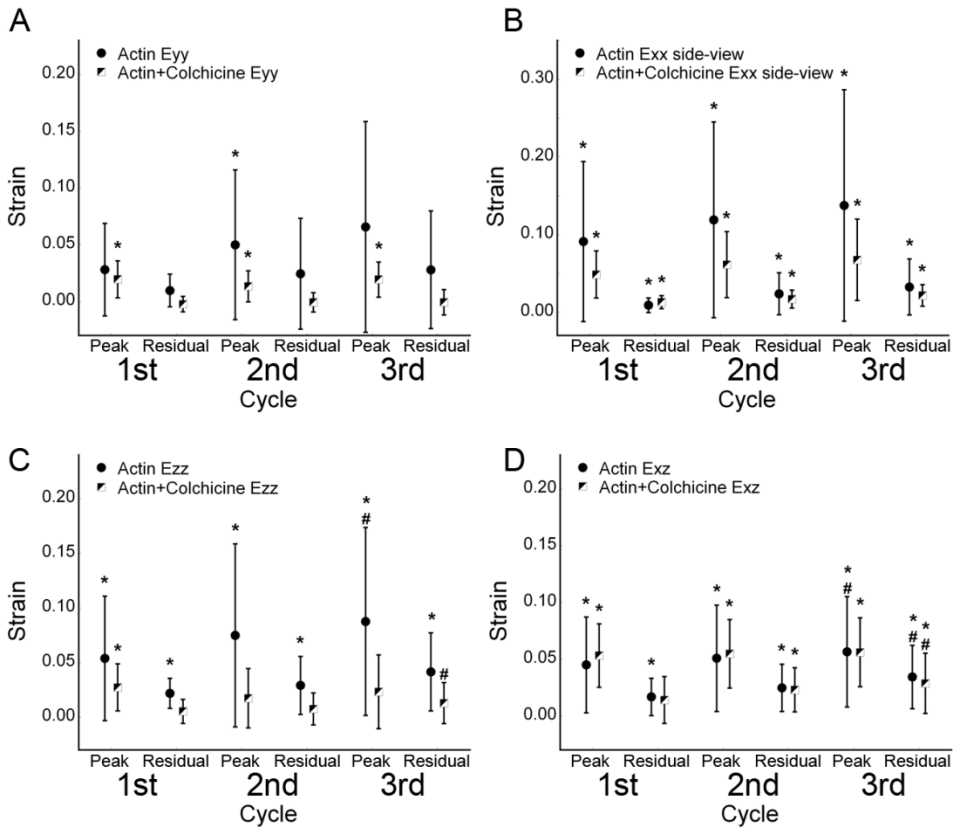

Figure 2.6: Actin and Actin+Colchicine whole-cell average strains for (A) Eyy, (B) Exx side-view, (C) Ezz, and (D) Exz. * = strain is greater than zero, $p<.05$, # = 3rd cycle peak/residual strain greater than 1st cycle's respective peak/residual strain, $p<.05$. Error bars are standard deviations.

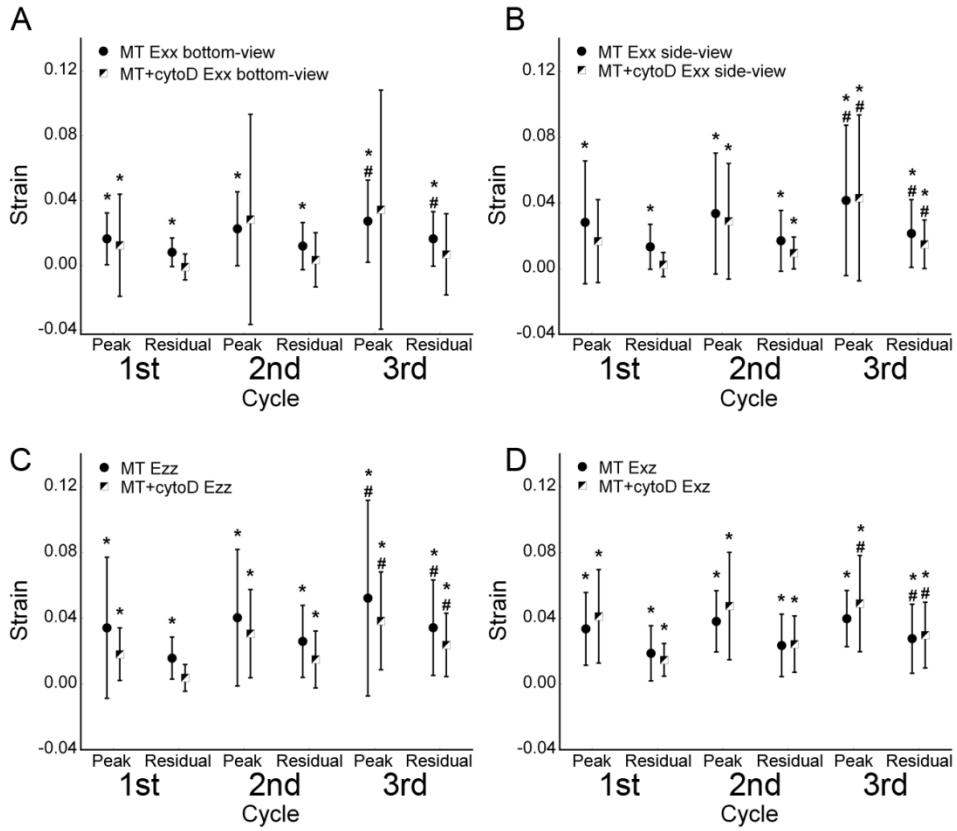

Figure 2.7: MT and MT+cytoD whole-cell average strains for (A) Exx bottom-view, (B) Exx side-view, (C) Ezz, and (D) Exz. * = strain is tensile (greater than zero), $p<.05$, # = 3rd cycle peak/residual strain greater than 1st cycle's respective peak/residual strain, $p<.05$. Error bars are standard deviations.

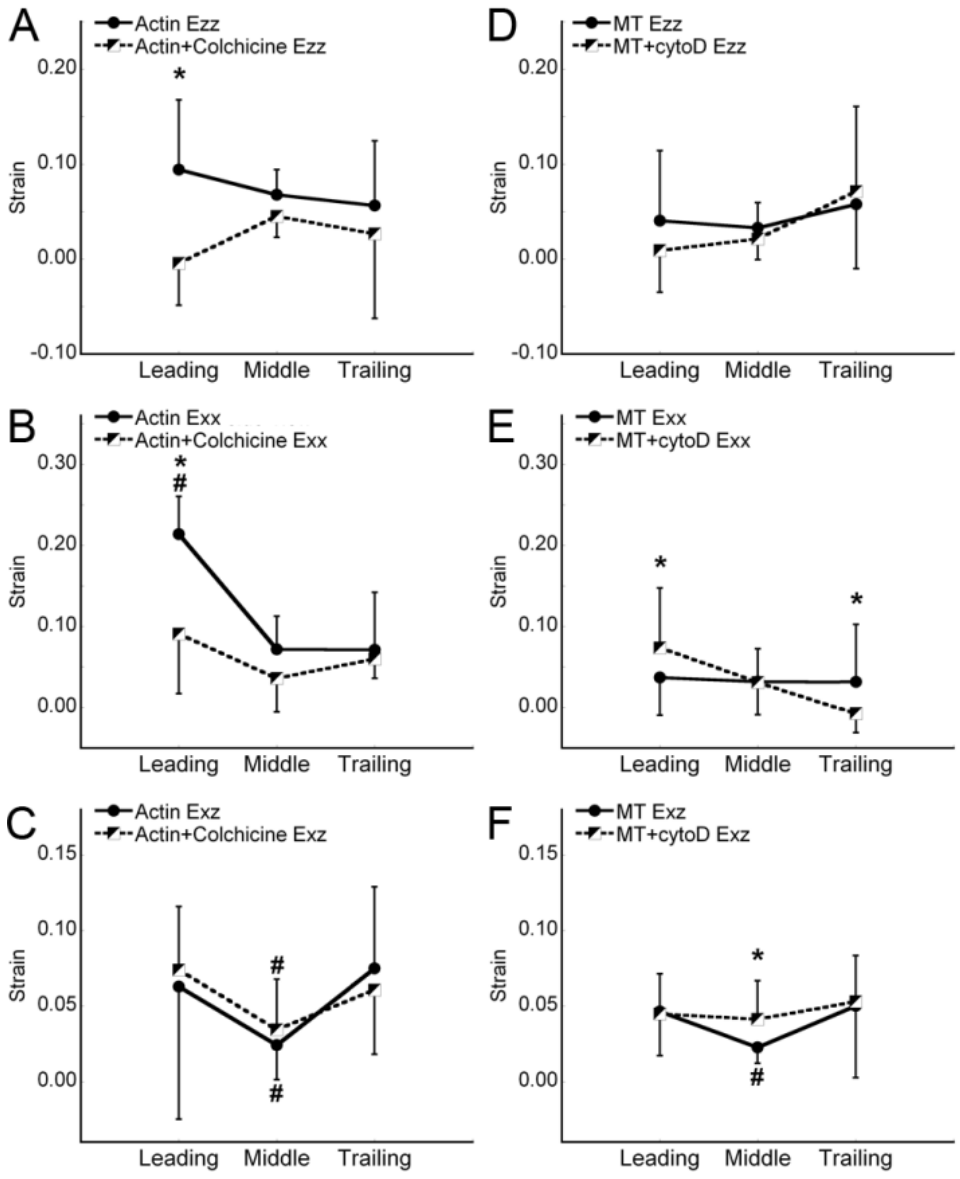

Figure 2.8: Drug and subcellular thirds location interactions in the actin network tracked strains (A, B, C) and MT network tracked strains (D, E, F). (A,D) Ezz strains, (B,E) side-view Exx strains, (C,F) Exz strains. * = statistically significant difference of the strains at given subcellular third location between groups. # = strain at location is significantly different from other subcellular third locations within that group. Error bars are standard deviations.

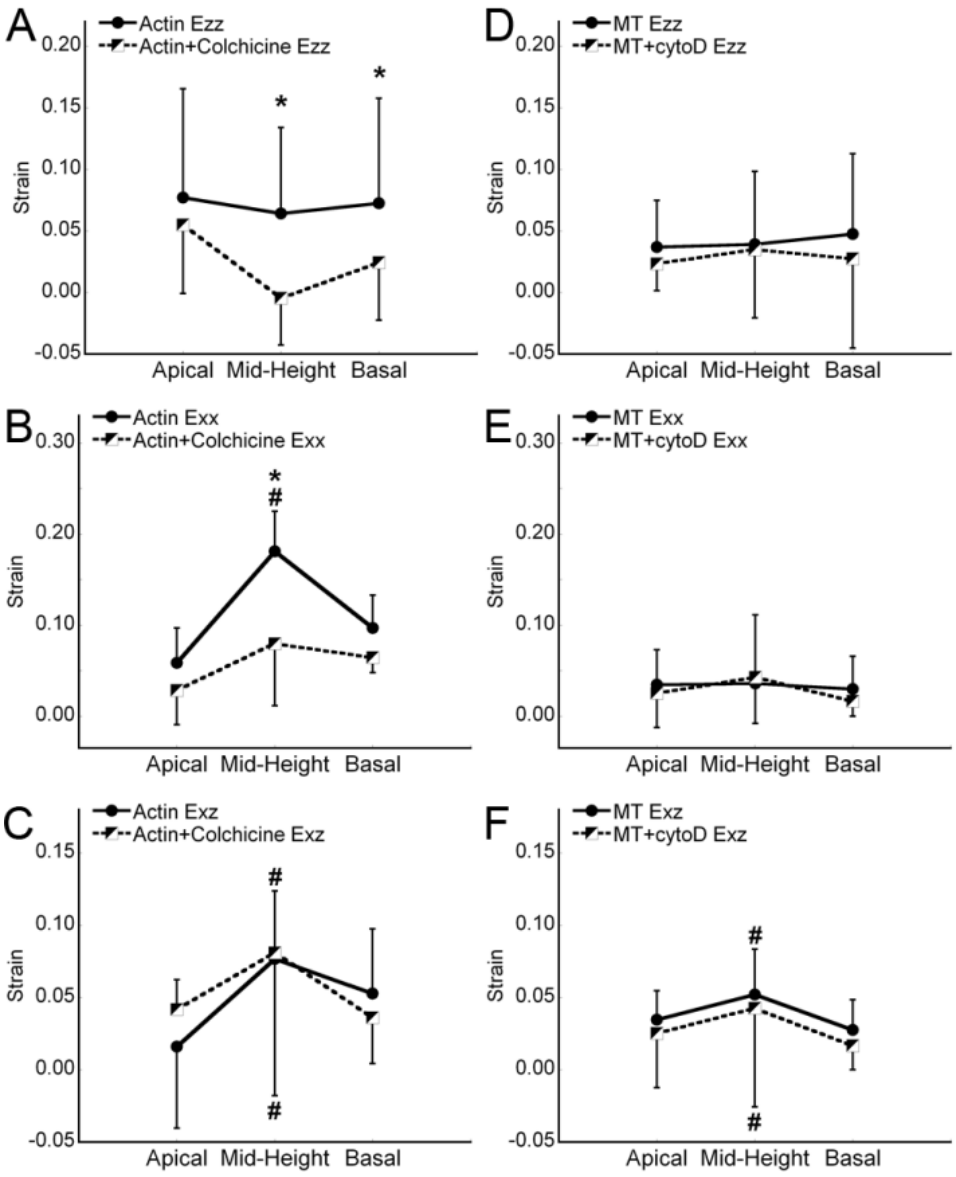

Figure 2.9: Drug and side-view heights location interactions in the actin network tracked strains (A, B, C) and MT network tracked strains (D, E, F). (A,D) Ezz strains, (B,E) side-view Exx strains, (C,F) Exz strains. * = statistically significant difference of the strains at given side-view height location between groups. # = strain at location is significantly different from other height locations within that group. Error bars are standard deviations.

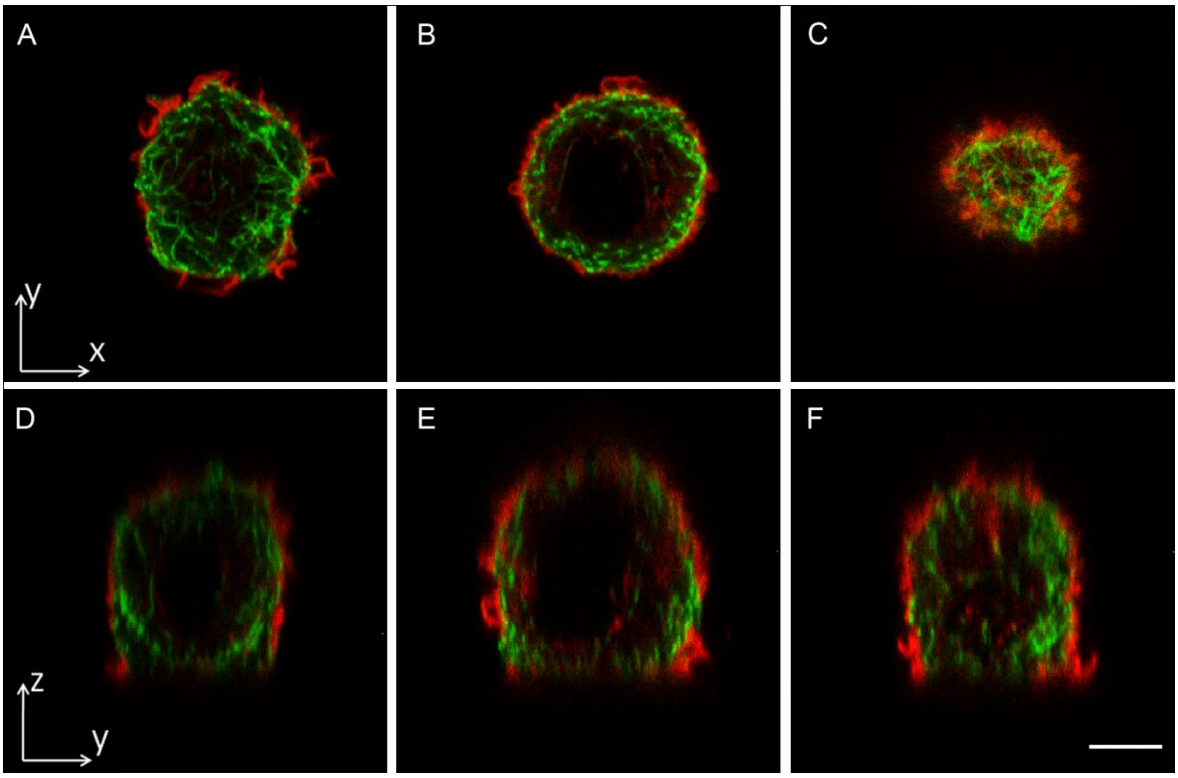

Figure 2.10: Confocal sections of an MLO-Y4 osteocyte fixed and stained for β-tubulin (green) and F-actin (red). Different subcellular heights shown for (A) basal, (B) mid-height, and (C) apical regions. Different subcellular thirds shown for (D) leading, (E) middle, and (F) trailing edges of the osteocyte. Axes definitions are in Figure 1. Scale bar is 5μm.

Chapter 3. Simultaneous Tracking of 3D Actin and Microtubule Strains in Individual MLO-Y4 Osteocytes under Oscillatory Flow

3.1 Introduction

Among the three major classes of bone cells (osteoblasts, osteoclasts, and osteocytes), osteocytes have attracted particular interest in the past several years (Bonewald 2011). Osteocytes have been established as mechanosensors in bone that can directly regulate bone turnover and adaptation (Tatsumi, Ishii et al. 2007). Mechanical load-induced fluid flow through the lacuncanalicular system has been proposed to induce shear stresses over the cell body and processes of osteocytes in the pericellular space to activate biochemical pathways (Weinbaum, Cowin et al. 1994; Burger and Klein-Nulend 1999). Furthermore, this fluid flow profile has been hypothesized to be oscillatory at 1 Hz. How an osteocyte deforms under dynamic, oscillatory fluid flow is still poorly understand in several important aspects. Accessing and measuring fluid shear stresses and strains in osteocytes embedded in the microscopic, narrow lacunocanalicular bone tissue matrix has proven challenging in many regards (Price, Zhou et al. 2011). *In vitro* experiments on extracted osteocytes have proven essential in understanding osteocyte mechanics. Most *in vitro* cell studies of osteocytes under oscillating flow have been performed on either semi-confluent or confluent, adherent osteocytes. Very few studies have considered the mechanical behavior of osteocytes at the single cell level (Baik, Lu et al. 2010; Rath, Bonewald et al. 2010). Osteoblast bone cells, a precursor to the osteocyte, deform elastically under dynamic oscillatory flow but viscoelastically under a steady flow (Kwon and Jacobs 2007). However, osteoblasts are morphologically and

biochemically distinct from osteocytes (Bonewald and Johnson 2008). This highlights the need to characterize osteocyte mechanics under a range of physiologically relevant fluid shear flow patterns.

Previous *in vitro* fluid shear studies on primary osteocytes and osteocyte cell lines have focused on flat, spread osteocytes, but the *in vivo* cell body shape of osteocytes is ellipsoidal or spherical (Vatsa, Breuls et al. 2008; van Hove, Nolte et al. 2009). It has been have demonstrated that osteocytes behave differently in this 3D configuration than when flat and spread (Bacabac, Mizuno et al. 2008). Additionally, the actin and microtubule networks in round osteocytes have remarkably different distributions and properties than in spread osteocytes (Tanaka-Kamioka, Kamioka et al. 1998; Murshid, Kamioka et al. 2007). Downstream cytoskeletal remodeling events in osteocytes were also affected by the usage of oscillatory flow versus steady flow, illustrating that the osteocyte cell type can biochemically differentiate physiological flow patterns (Ponik, Triplett et al. 2007). A previous study in our laboratory studied how actin and microtubule networks deformed individually in osteocytes, but a high degree of intercellular variability was seen (Baik, Lu et al. 2010). Mechanical comparisons between the two networks were limited due to this heterogeneity between individual cells. Studies in actin and MT polymer gel solutions have revealed composite-like behavior when the two networks interact under mechanical loading (Lin, Koenderink et al. 2007; Pelletier, Gal et al. 2009). How this mechanical behavior and interaction scale up in a cellular context remains to be seen, however. Therefore, it was of interest in this study to characterize the deformational behavior of the actin and MT networks in an osteocytes' cell body under a physiological level of fluid shear flow at the single cell level.

Limitations in temporal resolution of traditional raster-scanning 3D microscopy techniques (i.e. confocal and deconvolution) have hindered the ability to capture the 3D mechanical behavior of osteocytes because of the dynamic nature of oscillating flow (1 Hz) and the near-instantaneous mechanical responses of the cell. Previously in our laboratory, we developed a "quasi-3D" microscopy technique that was able to image a single cell in two orthogonal planes simultaneously while maintaining a high temporal resolution (Baik, Lu et al. 2010). This technique allowed better spatiotemporal visualization of the dynamics of cellular deformation in 3D that would have been lost in the slower raster scanning techniques. Side-view observations yielded novel ways to visualize and measure the shear strain of a cell under flow.

The viscoelastic deformational behavior between steady and oscillatory flow patterns in osteocytes will be compared using the actin and microtubule networks as measures of strain. By tracking both networks simultaneously using new developments in the quasi-3D microscopy technique, *direct* comparisons can now be made between the two networks, since the cytoskeletal analyses are paired and at a high enough temporal resolution to fully map out the oscillatory and steady loading profiles. The objectives of this study were to 1) simultaneously image in quasi-3D the actin and MT networks in osteocytes under steady and oscillatory fluid flow; and 2), calculate the developed strains in the actin and MT networks under the different flow profiles, and 3) compare their behaviors within the same cell.

3.2 Methods

3.2.1 Quasi-3D Microscopy

The basic quasi-3D design is presented in a previous study from our laboratory (Baik, Lu et al. 2010). In brief, an inverted microscope and an upright microscope with a 45° mirror in its lightpath are focused on a single cell in a rectangular tube with 60X objectives (Fig. 3.1A). These microscopes are independently yet simultaneously focused on two orthogonal planes of the same cell, dubbed "bottom-view" and "side-view." For this study, an additional functionality of simultaneous collection of up to 4 emission channels was added into the quasi-3D system. Two Quadview beamsplitters (Photometrics, Tucson, AZ) and custom-designed dichroics and excitation filters were used to visualize both the actin and microtubule networks simultaneously in quasi-3D (See Appendix Fig. A.1). The multichannel quasi-3D system was designed to collect the emissions of the following common dyes: CFP, YFP, mCherry/mkate2, and DiR (emission filters of 470/28, 530/30, 641/75, and 809/81, respectively) (Semrock, Rochester, NY). To achieve simultaneous dye excitation, a multi-band excitation filter was added to the xenon lamp light source to excite CFP and mkate2 (430/25 and 570/40). A custom-made dichroic was placed in the microscopes to reflect the excitation bands and pass-through the emission bands to the beamsplitter. DU-885 EMCCD cameras (Andor, Belfast, Northern Ireland) on each of the microscopes captured the bottom- and side-view emissions.

3.2.2 Cell Culture

MLO-Y4 osteocyte-like cells (a gift from Dr. Lynda Bonewald of the University of Missouri-Kansas City) were grown in α-modified Eagle's medium supplemented with

5% fetal bovine serum and 5% calf serum. The Lifeact live-cell F-actin probe (Riedl, Crevenna et al. 2008) was cloned into a TagCFP fusion plasmid (Evrogen, Moscow, Russia) to allow visualization of F-actin dynamics in cyan. The EMTB (ensconsin microtubule binding domain) MT probe (Faire, Waterman-Storer et al. 1999) was cloned into an mkate2 fusion plasmid to allow visualization of MT dynamics in red/far-red. The TagCFP and mkate2 fluorescent protein variants were chosen to minimize spectral bleedthrough of the fluorophores to negligible levels during simultaneous acquisition. Cells were double-transfected with the TagCFP-Lifeact and mkate2-EMTB plasmids 24 hours prior to flow experiments using Fugene 6 (Roche Applied Science, Indiana, IN) according to manufacturer's instructions.

3.2.3 Fluid Flow Experiments

24 hours after transfection, cells were trypsinized and plated on narrow glass slides for 45 minutes to ensure a fully attached, rounded cell shape. The glass slides were then placed into a square glass tube for imaging and flow. Hank's Buffered Saline Solution was used as flow media. Steady, unidirectional fluid flow (n=8) at a wall shear stress of 10 dynes/cm^2 was achieved by using a syringe pump (New Era Pump Systems, Wantagh, NY) and gas-tight syringe (Hamilton, Reno, NV).

Dynamic, oscillatory fluid flow (n=7) with a peak shear stress of 10 dynes/cm^2 was provided by a custom-built oscillatory pump. The flow profile was sinusoidal at a 1Hz frequency. Both flow types were applied to the flow chamber for 10 seconds. An individual cell was imaged in quasi-3D at a 10Hz frequency to fully map out the fluid flow profiles.

3.2.4 Image Analysis

All calculations were performed in MATLAB 7.8 (The MathWorks, Natick, MA). Intracellular displacement fields of the actin and MT networks for each cell were obtained identically for both bottom and side views according to a previously elaborated technique involving digital image correlation (Sutton, Cheng et al. 1986; Baik, Lu et al. 2010). Displacement fields were first smoothed with a bilinear least squares filter (Pan, Xie et al. 2007) and then smoothed and differentiated using a thin-plate spline algorithm (Wang, Deng et al. 2002). Finite Lagrangian strain fields were then calculated (three bottom-view strains: Eyy, bottom-view Exx, and Exy; and three side-view strains: Ezz, side-view Exx, and Exz). The absolute strain error on simulated rigid-body displacement actin and MT networks was 2.7e-4 ± 3.12e-4.

3.2.5 Strain Analysis

Strains were averaged in various subcellular regions (Fig. 1B). For steady flow, exponential constants for strains that displayed creep and creep recovery behavior were extracted from strain time course plots. Strain time course plots for each region were fit to an exponential function $\varepsilon(t) = a + be^{-ct}$ using least squares curve fitting. Plots that converged were considered to have creep-like behavior and the exponential constants were used in further analyses. Strains that displayed creep-like behavior in both networks were directly compared in paired statistical tests.

Strain time course plots in oscillatory flow were run through a high pass filter, and plots that displayed periodic ~1Hz behavior had the peaks and troughs extracted for further analyses.

3.2.6 Statistical Analysis

All statistical analyses were performed using NCSS 2007 software (NCSS LLC, Kaysville, UT). Strain values for the actin and MT networks within each cell at different times or in subcellular regions were compared in paired analyses within a cell. The majority of comparisons were determined to have non-normal distributions, so the non-parametric Wilcoxon-signed rank test was used. The significance level, α, was set at 0.05.

3.3 Results

3.3.1 Simultaneous Tracking of Actin and MT Networks under Fluid Flow

Using the dual-excitation filter and emission beamsplitter, the actin and microtubule networks in a single osteocyte were able to be imaged simultaneously (Fig. 3.2A). F-actin networks formed primarily cortical networks near the membrane with diffuse staining perinuclearly. MT networks were also perinuclear but were noticeably less prevalent near the plasma membrane. Both networks were excluded from the cell nucleus. F-actin was also visible in very short filopodia-like cellular processes in the basal periphery of the cell, given the short plating time. MT networks were not visible in this area.

A high temporal resolution of 10Hz was maintained, allowing instantaneous strain deformations, i.e. at the onset of flow, to be measured in steady and oscillatory fluid flow profiles (Fig. 3.2, B & C).

3.3.2 Steady Flow Strain Comparisons

Actin and MT networks tended to behave with viscoelastic creep and creep-recovery behaviors in the actin and MT networks strains under steady flow, confirming

previous results (Baik, Lu et al. 2010). This behavior was observed with a 65.6% frequency in the subcellular shear Exz in both networks but was also present to a lesser degree in the normal Ezz and Exx strains at a 50.5% frequency. Bottom-view Eyy exhibited creep behavior only 27.1% of the time. There was no statistically significant difference in the frequency of creep behavior between the two networks. However, some cells displayed creep behavior in only one of the networks and not the other, adding to the complexity of intracellular strains at the single-cell level.

Additionally, high variability was seen in the heterogeneous distribution of the strains of the actin and MT networks within the same cell (Fig. 3.3). Peak strains at the end of the flow period were averaged in the subcellular regions of the cell (Fig. 3.4). To emphasize, all comparisons were performed using paired statistical tests between the actin and MT networks within single cells, thereby decreasing intercellular heterogeneities. In the apical region, MT Exz was higher than actin Exz ($p<.01$) by an average of .0192. However, this difference was reversed in the basal region of the cell. Actin Exz was higher than MT Exz ($p<.05$) by an average of .0201 in the basal region. Ezz normal strain was higher by an average of .0237 and .00797 in the leading ($p<.01$) and middle regions of the cell ($p<.05$).

Subcellular strains that displayed creep behavior in both networks had their exponential time constants directly compared (Table 3.1). Creep was slower in the normal strains than in shear strain, as evidenced by the higher time constants to reach equilibrium. Interestingly, Ezz and side-view Exx strains, but not Exz, reached equilibrium in creep recovery faster than in creep ($p<.05$). Creep recovery of side-view Exx, actin networks were able to reach equilibrium faster than MT networks ($p<.05$).

3.3.3 Oscillatory Flow Strain Comparisons

The actin and MT networks had elastic-like behavior under oscillatory flow. Both networks had smaller strains than in steady flow, with heterogeneous strain patterns that oscillated with the loading profile (Fig. 3.5). No residual strains were apparent after the end of flow (Fig. 3.2C). Oscillations were seen in both networks, but the average center position over the 10 periods of oscillations was not always zero strain. The peaks and troughs of the oscillations also did not deviate greatly through the 10 periods.

Oscillations were more prevalent in the actin networks than in the MT networks (Fig. 3.6). For Exz, oscillations occurred in 83.3% of the subcellular regions of the actin networks, but only in 30.9% of the subcellular regions in the MT networks. For the side-view normal strains (Ezz and side-view Exx), actin networks displayed oscillations in 35.7% of the subcellular regions, but in only 2.4% of the subcellular regions in the MT networks. However, oscillations in bottom-view normal strains (Eyy and bottom-view Exx) were more readily visible in both networks; actin and MT network bottom-view normal strains oscillated at 76.2% and 21.4% frequencies, respectively.

When comparing shear Exz at the whole cell average level of cells that displayed oscillations in both networks, the average peak-to-trough amplitudes of the actin and MT networks were .0094 ± .0038 and .0051 ± .0025, respectively, and the peak-to-trough amplitude was consistently higher in the actin networks than in the MT networks ($p<.05$).

3.4 Discussion

In this study, a multichannel quasi-3D microscopy technique was implemented to directly compare the fluid shear-induced strains of the actin and MT networks within a

cell. Steady and oscillatory flow patterns were used to analyze any differences between the two flow patterns on the cytoskeletal networks. The advantage of the multichannel quasi-3D microscopy technique was in its ability to image the two cytoskeletal networks at a sufficiently high spatiotemporal resolution to be able to map the intracellular strains under the dynamic oscillatory fluid flow profile. Dual labeling of the actin and MT cytoskeletons has been used in studies in other cell types (Salmon, Adams et al. 2002; Sampathkumar, Lindeboom et al. 2011), but this study used a truly simultaneous, rather than sequential, acquisition of the networks. Imaging a sinusoidal loading profile without undersampling generally requires at least 6 acquisition frames per period (Wang, Hu et al. 2007). Here, we obtained full coverage of the 1 Hz loading frequency by imaging both cytoskeletal networks at 10 Hz. Near-instantaneous responses of the cytoskeletal networks were captured and measured in both steady and oscillatory flows. Heterogeneity at the single-cell level has been observed in many cytoskeletal and mechanical behavior studies (Jaasma, Jackson et al. 2006; Dangaria and Butler 2007; Baik, Lu et al. 2010), and this study observed that responses in one network did not always match the strain in the other network within the same cell in either strain magnitude or time course pattern. Inter- and intracellular variability was high in this study, but the ability to pair the comparisons revealed novel observations. Furthermore, the dual labeling and short plating time recapitulated the spatial organization of the actin cortex and microtubule networks that are seen in osteocyte cell bodies *in vivo* (Tanaka-Kamioka, Kamioka et al. 1998; Kamioka, Sugawara et al. 2006; Vatsa, Semeins et al. 2008). Thick stress fibers which are numerous in flat, spread osteocytes *in vitro* but undetectable *in vivo* were absent in the current experimental setup.

Both steady and oscillatory flow produced measurable responses in shear strain Exz. Under steady flow, shear strain in both networks displayed viscoelastic behavior as creep and creep recovery were prevalent in both networks. The differences in actin and MT peak strains may be partially explained by the spatially heterogeneous distributions of the two networks. The cortical actin networks next to the leading edge membrane experience fluid shear flow before the MT networks, as the bulk of the MT networks are more intracellular and further away from the membrane, and this shielding may explain the observed higher actin Ezz strains near the leading edge of flow. The higher observed shear Exz in the basal actin Exz may also be due to anchoring of actin at the focal adhesions at the cell-extracellular matrix interface, which the MT networks are not strongly coupled to.

The decrease in time constant between the creep from fluid shear loading and creep recovery from flow removal of both networks suggests an active cellular process that may be modulating the viscoelastic behavior of the cell and its cytoskeleton. Previous studies have demonstrated rapid reorganization of the cytoskeleton in response to flow (Choi and Helmke 2008), and molecular motors like myosin have been shown to be able to actively control cytoskeletal network viscoelasticity by allowing entangled cytoskeletal fibers to move more easily (Humphrey, Duggan et al. 2002).

Under oscillatory flow, shear strain in both networks behaved elastically and followed the oscillatory loading pattern with no residual strains post-flow. The actin networks were the most responsive networks in frequency and magnitude of shear strains, suggesting that actin is an important link in mechanotransduction of physiologically relevant load levels. The activation of actin-related signaling pathways but not MT-

related pathways may be the link between the observed differences in steady and oscillatory flow in bone cells (Jacobs, Yellowley et al. 1998; Ponik, Triplett et al. 2007; Case, Sen et al. 2011), as the MT networks are less responsive in oscillatory flow but similar in steady flow. Strain oscillations were more visible in bottom-view than side-view, emphasizing the three dimensional nature of the deformation. Neither view alone was sufficient to characterize the full behavior of osteocyte cell bodies under the two fluid flow profiles used in this study.

While actin networks showed more long-range order in strains at the whole-cell level, MT networks still had large deformations in the subcellular region strain analysis. MT deformations at this level were on the same order of magnitude as the actin strains; the strains averaged out in the whole-cell analysis to a near-zero strain in oscillatory flow. MT strains may have a shorter range of influence than the actin networks, *e.g.* deformations in the leading edge to flow do not influence the trailing edge MT networks.

Dendritic processes have been well-established experimentally as mechanosensitive communicators in osteocytes (Adachi, Aonuma et al. 2009; Burra, Nicolella et al. 2010). Additional theoretical studies have mapped out the strain on the cytoskeleton in osteocyte processes in bone canaliculae (Wang, McNamara et al. 2007). The osteocyte cell body, situated in the bone lacunae, has been regarded as insensitive because it would experience lower strains *in vivo.* Recent *in vitro* and *in vivo* evidence have renewed interest in the role of the osteocyte cell body in mechanotransduction. For example, focal adhesions in the osteocyte cell body *in vivo* rearrange within the cell body depending on its mechanical environment, suggesting the cell body actively senses deformation and adapts to the loading (Vatsa, Semeins et al. 2008). When osteocytes

were not allowed to spread to avoid non-*in vivo* artifacts such as thick, aligned stress fiber formation and nuclear flattening, elastic modulus decreased and mechanosensitivity increased (Bacabac, Mizuno et al. 2008). Therefore, the understanding of the osteocyte cell body remains incomplete. *In vitro* experiments that recapitulate the *in vivo* shape and organization of osteocytes may prove crucial to understanding the interplay between the osteocyte processes and the osteocyte body.

In conclusion, we have developed a novel multi-channel quasi-3D technique to measure actin and MT network strains in a single cell. Mapping the link between flow stresses and biological signaling pathway activation requires an understanding of the mechanical responses of the cellular structures, including the cytoskeleton, membrane, and nucleus. Further studies in the downstream effects of actin network deformations and its spatial heterogeneity will help elucidate these questions.

3.5 Tables

Strain	Creep Time Constant		Creep Recovery Time Constant	
	Actin	MT	Actin	MT
Ezz	10.67±13.68†	13.17±10.12†	2.83±1.64†	2.58±1.16†
Exx, side-view	9.60±7.74†	6.74±5.66†	1.76±1.14*†	2.31±0.68*†
Shear Exz	4.45±2.83	3.77±1.54	3.58±1.74	3.82±1.33

Table 3.1: Creep and creep recovery time constants for each network for the side-view strains. * = significantly different from other network ($p<.05$). † = significantly different between creep and recovery ($p<.05$)

3.6 Figures

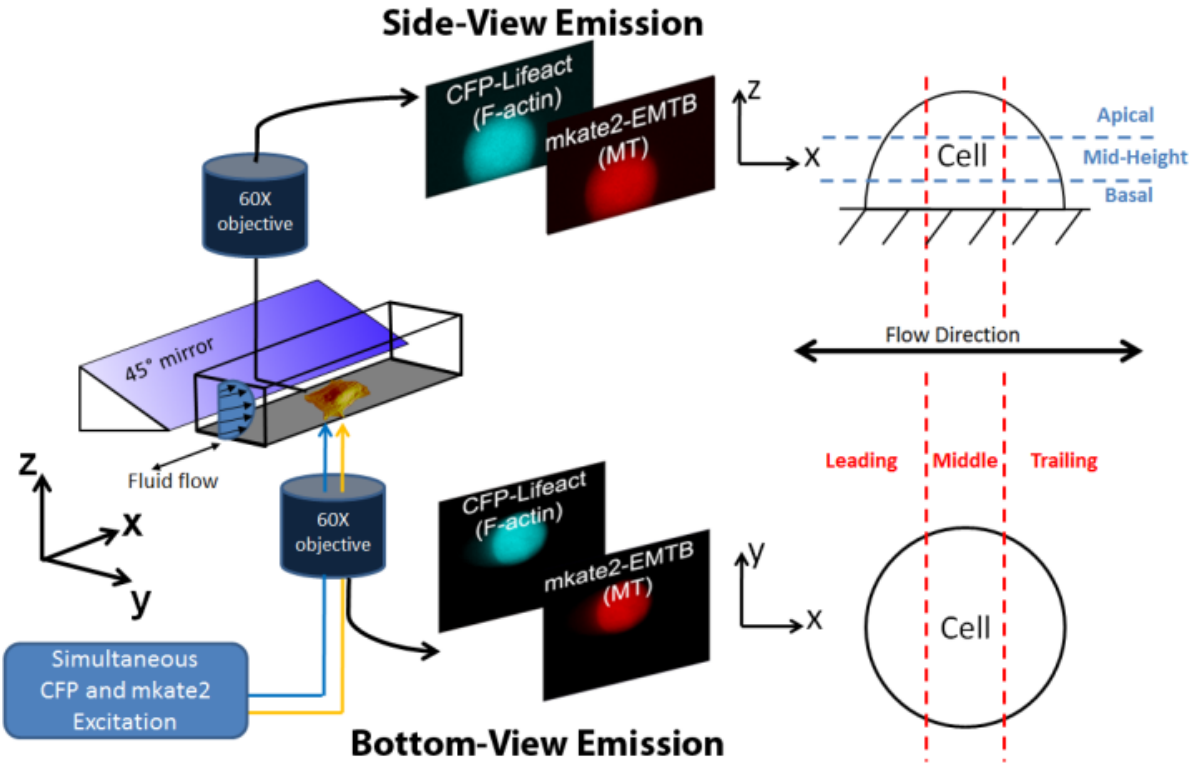

Figure 3.1: Schematic of the multi-channel quasi-3D microscopy technique to visualize the F-actin and MT networks simultaneously. The CFP and mkate2 fluorophores are excited with a dual-excitation filter. A beamsplitter in both microscopes separates the CFP and mkate2 emissions. Each microscope's camera is synchronized to obtain images at the same timepoint. Definitions for subcellular regions in the two views are presented on the right.

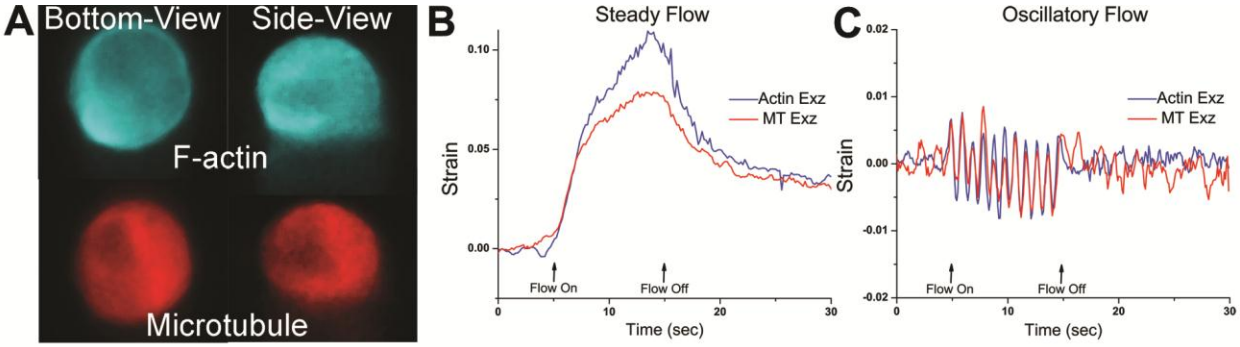

Figure 3.2: A) Image of the F-actin and microtubule networks of an MLO-Y4 osteocyte imaged simultaneously in two orthogonal planes (bottom and side views). B) Sample side-view whole-cell shear Exz strain trace for both cytoskeletons of a single osteocyte under steady flow. Both networks display creep and creep-recovery behaviors. C) Sample side-view whole-cell shear Exz strain trace for both cytoskeletons of a single osteocyte under oscillatory flow. Both networks display sinusoidal shear strains that follow the oscillatory flow pattern. The magnitude of the strain is also lower than in steady flow.

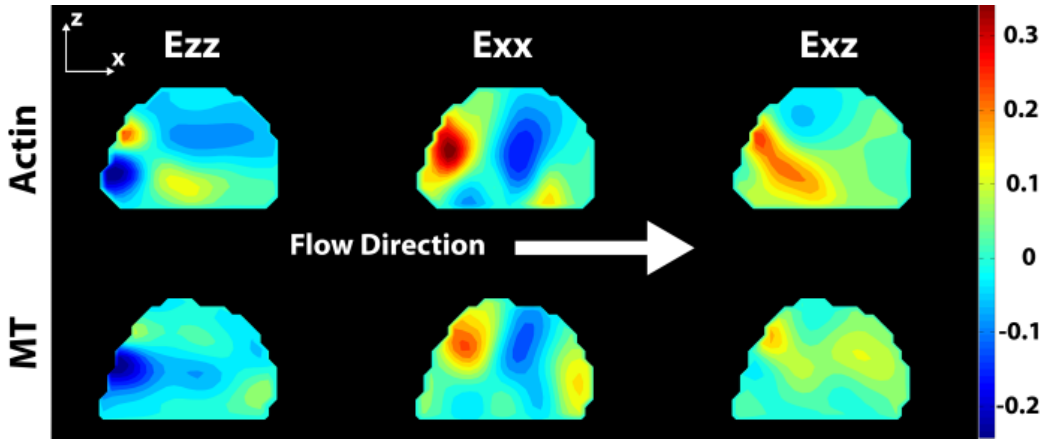

Figure 3.3: Strain contour plot of steady flow strains at the end of the loading period. The side-view strains of the actin and MT networks are presented from the same cell. Between the networks, the magnitudes of strains are different, and areas of tension and compression do not coincide in all areas, such as in Ezz in this cell.

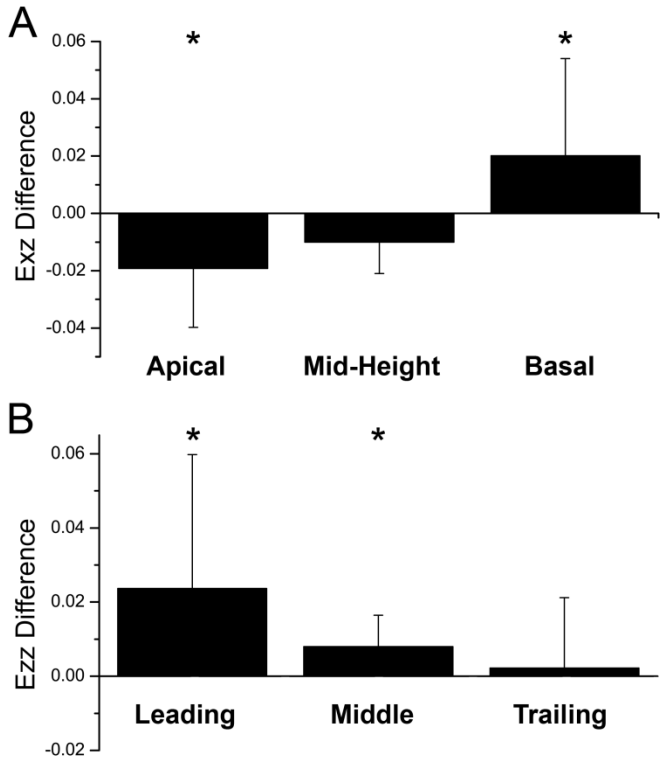

Figure 3.4: A) Mean of the paired differences within each cell between the Actin and MT Exz strains at different locations in the cell at the end of the steady flow loading period. In the apical region of the cell, Actin Exz was significantly lower than MT Exz ($p<.01$). In the basal region of the cell, the Actin Exz was significantly greater than MT Exz ($p<.05$). B) Mean of the paired differences within each cell between the Actin and MT Ezz strains at different locations in the cell at the end of the steady flow loading period. In the leading ($p=.05$) and middle ($p<.05$) regions of the cell, Actin Ezz was significantly higher than MT Ezz when comparing the paired differences between the two strains within each cell. Error bars represent standard deviation.

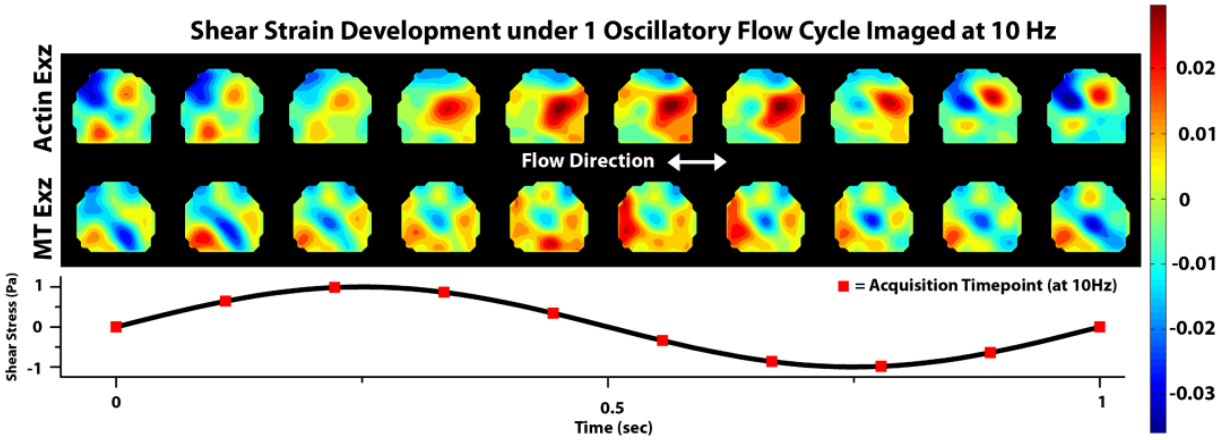

Figure 3.5: Actin and MT strain contour plots of the 5th cycle (of 10 total at 1Hz) of oscillatory flow. 10 images were taken during each cycle and are presented. Strains oscillate in magnitude following the oscillatory loading profile. The areas of oscillating strains in the two networks are distinct.

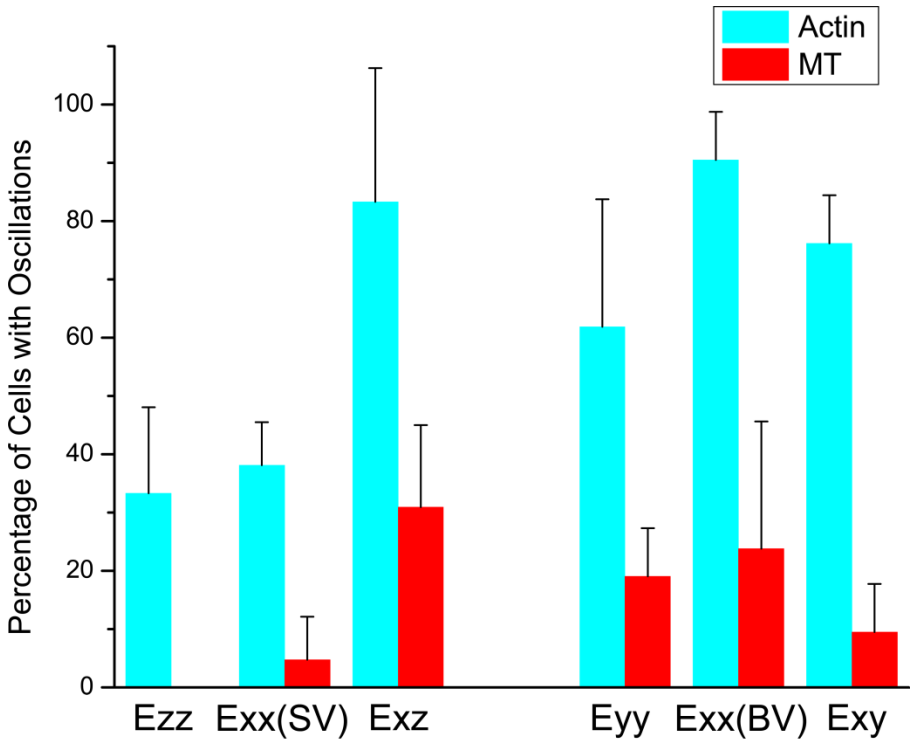

Figure 3.6: Percentage of cells that displayed oscillatory behavior in each strain. Oscillatory strain behavior was readily apparent in the actin strains and in shear Exz. The percentages in the MT networks were always lower than in the actin networks. Error bars represent standard deviation.

Chapter 4. Calcium Signaling in Osteocytes Induces Actomyosin Contractions

4.1 Introduction

The calcium ion (Ca^{+2}) is a signaling molecule crucial to the physiology of every cell type in the human body. Ca^{+2}/Calmodulin signaling regulates diverse cellular processes ranging from muscle contractility to neuronal memory by temporal control of intracellular Ca^{+2} concentration ($[Ca^{+2}]_i$). Many types of chemical and electrical stimuli can induce these $[Ca^{+2}]_i$ oscillations through activation of intracellular calcium stores (endoplasmic and sarcoplasmic reticulum) or membrane channels. The additional discovery of mechanosensitive ion channels (Guharay and Sachs 1984; Lansman, Hallam et al. 1987) has led to the finding that mechanical stimuli can also induce $[Ca^{+2}]_i$ oscillations (Ando, Komatsuda et al. 1988; Ajubi, Klein-Nulend et al. 1996; Yellowley, Jacobs et al. 1997).

Robust intracellular $[Ca^{+2}]_i$ oscillations, mediated by mechanosensitive Ca^{+2} channels and ER Ca^{+2}, have been observed in osteocytes in response to fluid shear stresses (Lu, Huo et al. 2012; Lu, Huo et al. 2012) even at very low magnitudes (Kamel, Picconi et al. 2010), lending credence to the hypothesis that osteocytes are highly sensitive mechanosensors. Furthermore, $[Ca^{+2}]_i$ oscillations have been observed in response to hormones (Ren and Wu 2012) and autonomously *in vivo* and *in vitro* (Ishihara, Sugawara et al. 2012). While many distant downstream pathways of $[Ca^{+2}]_i$ signaling have been studied, the immediate, temporally regulated effects of these

numerous $[Ca^{+2}]_i$ oscillations in osteocytes have not been investigated. The functional role of the frequent and regular $[Ca^{+2}]_i$ oscillations in bone have not been established.

A recent study in the gene expression of primary osteocytes has suggested high levels of muscle contraction-related proteins (Paic, Igwe et al. 2009). Interestingly, mRNA coding for protein isoforms from skeletal, cardiac, and smooth muscle was detected in the assay. Whether osteocytes represent a new hybrid muscle type incorporating all three muscle phenotypes or have complex post-transcriptional modifications preventing protein expression of muscle types has yet to be investigated. A hallmark of muscle is its $[Ca^{+2}]_i$-dependent actomyosin contractility: a $[Ca^{+2}]_i$ spike or spark triggers a troponin or myosin light chain kinase (MLCK) mediated actomyosin contraction. Coupling between $[Ca^{+2}]_i$ and contractile behavior has also been observed in non-muscle cell types such as fibroblasts and its related myofibroblasts (Doyle, Marganski et al. 2004; Munevar, Wang et al. 2004; Castella, Buscemi et al. 2010). Furthermore, the rate of $[Ca^{+2}]_i$ signaling and oscillations are integrated into different kinds of contractile responses (Sanderson, Bai et al. 2010).

We hypothesized that osteocytes utilize $[Ca^{+2}]_i$ oscillations to activate muscle-like contractile mechanical behavior. In this study, we used a quasi-3D imaging technique to simultaneously measure the deformations of the actin networks *and* $[Ca^{+2}]_i$ in single osteocytes in response to several types of stimuli for $[Ca^{+2}]_i$ influx. The imaging technique allowed unique 3D parameters to be measured on a timescale appropriate for observing potential contractile events that are tuned to $[Ca^{+2}]_i$ influx. Here, we demonstrate novel osteocyte mechano- and transduction behavior where $[Ca^{+2}]_i$

oscillations activate dynamic actomyosin contractions using a smooth muscle-like mechanism.

4.2 Methods

4.2.1 Quasi-3D Microscopy

The basic quasi-3D design was presented in a previous study from our laboratory (Baik, Lu et al. 2010). In brief, an inverted microscope and an upright microscope with a 45° mirror in its lightpath focus on a single cell in 2 orthogonal planes, dubbed "bottom-view" and "side-view," simultaneously using two EMCCD cameras (Fig. 4.1). Beamsplitters and multi-band excitation filters were added onto the system to allow *simultaneous* collection of emission bands of up to 4 common fluorescent dyes: CFP, YFP, mkate2, and near-IR. A custom-made dichroic was placed in the microscopes to reflect the excitation bands and pass-through the emission bands to the beamsplitter. To minimize photobleaching and phototoxicity, excitation light was attenuated by decreasing power output and use of a neutral density filter. To maintain simultaneous excitation of dyes and prevent camera pixel saturation from the higher intensity mkate2 emission, a neutral density filter was used on the mkate2 channel. Bleedthrough effects were accounted for by repeating all experiments using separate, sequential excitation of dyes.

4.2.2 Cell Culture

MLO-Y4 osteocyte-like cells were double transfected using Fugene 6 (Promega, Madison, WI) to visualize $[Ca^{+2}]_i$ and F-actin simultaneously using the following two plasmids: an improved Cameleon calcium FRET biosensor using ECFP and YPet as donor and acceptor fluorophores (Miyawaki, Llopis et al. 1997; Ouyang, Sun et al. 2008),

and the Lifeact live-cell F-actin probe (Riedl, Crevenna et al. 2008) cloned into a mkate2 fusion plasmid (Evrogen, Moscow, Russia). The fluorescent protein variants were chosen to minimize spectral bleedthrough during simultaneous acquisition. Alternatively, TagCFP-Lifeact and mkate2-EMTB were used to track the F-actin and microtubule networks simultaneously in the setup from Chapter 3.

Cells were plated on 10µg/mL fibronectin-coated glass microslides for 45 minutes to ensure a fully attached, rounded *in vivo* cell shape with proper cortical F-actin networks in the cell body. The slides were then placed into a square glass tube for imaging and flow.

4.2.3 Induction of Calcium Response

Steady, unidirectional fluid flow (n=10) at a wall shear stress of 2 Pa was applied. For drug-induced $[Ca^{+2}]_i$ responses, 50µM ATP (n=6) or 5µM ionomycin (n=5) were introduced (<0.075 Pa) into the imaging chamber at a low flow rate to ensure a wall shear stress of ~0.075 Pa. Cells were pre-incubated with 10µM ML-7 (n=5) or 150µM (+/-) blebbistatin to inhibit MLCK or myosin-2, respectively, for 20 minutes before ATP injection. In the blebbistatin group, Cameleon imaging was omitted due to the photoinactivation of blebbistatin by <500nm light.

4.2.4 Image Analysis

All image analysis was performed in MATLAB 7.8 (The Mathworks, Natick, MA). Intracellular displacement fields of the F-actin or MT networks were obtained for both views using a zero order digital image correlation technique. The x direction was defined as the flow direction, and the y and z as the lateral and height directions, respectively. Finite Lagrangian strain fields were then calculated from the displacement

fields using a bilinear least squares filter followed by a thin-plate spline differentiation (three bottom-view strains: Eyy, bottom-view Exx, and shear Exy; and three side-view strains: Ezz, side-view Exx, and shear Exz). ECFP and YPet FRET images were aligned using a normalized cross-correlation algorithm and YPet/ECFP emission ratios were calculated for each timepoint.

4.2.5 Western Blot

Cells were lysed in RIPA buffer supplemented with a protease/phosphatase cocktail (Sigma-Aldrich, St. Louis, MO) and quantified using a Bio-Rad protein quantification assay (Bio-Rad, Hercules, CA). 10µg of protein was loaded into 7.5% or 12% Tris-HCl SDS-PAGE electrophoresis gels and transferred overnight onto PVDF membranes. Primary antibodies raised in rabbit for skeletal muscle myosin heavy chain (MYH2), skeletal alpha-actin (ACTA1), Troponin I – fast skeletal (TNNI2), smooth muscle myosin heavy chain (MYH11), non-muscle myosin heavy chains (MYH9), myosin light chain kinase (MLCK1), and smooth muscle myosin heavy chain SM2 (MYH11) were obtained from Abcam (Abcam, Cambridge, MA). Troponin I (TNNI 1,2,3) was obtained from CellSignal (CellSignal, Beverly, MA). Troponin T – fast skeletal (TNNT3), raised in goat, was obtained from Santa Cruz Biotechnology (Santa Cruz Biotechnology, Santa Cruz, CA). Secondary anti-goat and anti-rabbit antibodies conjugated to horseradish peroxidase were obtained from Abcam. Gels were imaged using ECL+ (GE Healthcare Biosciences, Pittsburgh, PA) and a CCD blot imager (Nikon, Japan). Skeletal muscle and NIH3T3 protein lysates were used as positive and negative controls for skeletal and smooth muscle proteins, respectively (Abcam). FACS sorted

DMP1Topaz (+) and (-) cells were also loaded to verify protein presence in primary osteocytes (generous gift from Dr. Ivo Kalajzic, University of Connecticut).

4.3 Results

4.3.1 Simultaneous Tracking of $[Ca^{+2}]_i$ and Actin Strains under Fluid Shear Flow

$[Ca^{+2}]_i$ and actin network strains were successfully measured using the multi-channel quasi-3D microscopy technique (Fig. 4.2). Exposure times as low as 100msec were able to simultaneously image the ECFP, YPet, and mkate2 fluorescent dyes with minimal image post-processing. Imaging sampling rates of 0.5 Hz to 9Hz were able to capture the $[Ca^{+2}]_i$ spiking behavior and steady-flow induced creep strains. Sequential excitation of ECFP/YPet and then mkate2 did not change the profiles or strain measurements (data not shown). The 9 Hz sample rate occasionally allowed the identification of the initiation points of the global $[Ca^{+2}]_i$ spike (Fig. 2B) in a few of the tested cells, but there was no trend in the location of initiation of this potential $[Ca^{+2}]_i$ spark (Fig. 4.2 B).

Osteocyte $[Ca^{+2}]_i$ spikes were relatively long in comparison to the sampling rate, as transient flow-induced $[Ca^{+2}]_i$ spikes were ~20-40 seconds long and occurred ~10 seconds after the onset of flow (Fig. 4.2 A), agreeing with previous results using fura dyes (Lu, Huo et al. 2012). Interestingly, creep strain development was near-instantaneous upon flow onset, suggesting the rate-limiting step of $[Ca^{+2}]_i$ spike initiation may not be mechanical, but rather may be due to an intermediate signaling molecule.

Upon a $[Ca^{+2}]_i$ spike initiation, a decrease in actin Ezz was observed in 7 out of the 10 cells tested (Fig. 4.3). Compression was observed in Ezz regardless of whether or

not fluid flow had induced tensile creep (Osteocyte 1 and 3) or no overall change (Osteocyte 2) in the period prior to $[Ca^{+2}]_i$ spike initiation. The compression after spike initiation in Ezz was enough to counteract the flow-induced strains in the cells experiencing Ezz creep. It is presumed compression in other normal strains was not observed due to the partial masking effect of the contraction by the flow-induced tensile strains.

4.3.2 Chemically Induced $[Ca^{+2}]_i$ Spikes Results in Actin Contraction

To determine if the actin network contraction was dependent on just fluid flow-induced $[Ca^{+2}]_i$ or was a general response to $[Ca^{+2}]_i$ signaling, ionomycin and ATP were used to stimulate a $[Ca^{+2}]_i$ response: ionomycin is a Ca^{+2} ionophore and ATP acts on the P2X/P2Y purinergic receptors to effect a $[Ca^{+2}]_i$ response. Within several seconds, compression in all measured normal strains was visible in all groups (Fig 4.4 A, C). Ezz height strain tended to have the largest compression, while shear strains were not affected. In the ATP and ionomycin groups, Eyy and Exx also compressed, indicative of a whole-cell actin contraction. ATP stimulated cells displayed a recovery to baseline (~180 sec), demonstrating a reversible, phasic contraction. When the actin and MT networks were tracked simultaneously with the ionomycin stimulation, the MT networks displayed little contraction compared to the actin network within the same cell (Fig 4.4 B).

4.3.3 Myosin Mediates $[Ca^{+2}]_i$-dependent Contractility

Under ATP stimulation, ML-7, a MLCK inhibitor, drastically altered the kinetics of contraction (Fig. 4.4 D, E). The time before a decrease in Ezz strain was observed was increased from 13.3 ± 6.4 sec to 41.8 ± 24.2 sec. Blebbistatin had no effect on the time course or magnitude of the Ezz compression after $[Ca^{+2}]_i$ spike. Blebbistatin is a potent

skeletal and non-muscle myosin II inhibitor, but a poor smooth muscle myosin inhibitor (Limouze, Straight et al. 2004). The "no ATP" negative control showed no trend in strain development over the imaging period.

4.3.4 Smooth Muscle-like Contractions

Due to the surprising inability of blebbistatin to inhibit the contractions, we investigated the possibility that smooth muscle myosin is regulating the contractions. In MLO-Y4 cells, we failed to detect skeletal myosin-related proteins, including skeletal α-actin, skeletal myosin ATPase, or skeletal/cardiac troponins (Fig. 4.5 A). Western blots verified the presence of smooth muscle myosin-II ATPase and its SM2 isoform (Fig 4.5 B). The westerns for troponin I and smooth muscle myosin were repeated using lysates of FACS sorted DMP1 positive cells, verifying that primary osteocytes are similar to MLO-Y4 osteocytes in this regard. This data suggests a smooth muscle, rather than a skeletal or cardiac muscle, phenotype in osteocytes.

4.4 Discussion

Ca^{+2}/Calmodulin is a ubiquitous second messenger system in mammalian cells. Osteocytes have multiple $[Ca^{+2}]_i$ oscillations in response to fluid shear flow unlike many other cell types, including their predecessor osteoblasts (Lu, Huo et al. 2012). However, positing a biological reason for this robust $[Ca^{+2}]_i$ behavior in osteocytes has been difficult. Here, we demonstrate actomyosin contractility in the cell body of MLO-Y4 osteocytes mediated through smooth muscle myosin, which was previously hypothesized by another group (Paic, Igwe et al. 2009; Bonewald 2011). Similar to myocytes, a tight coupling between $[Ca^{+2}]_i$ oscillations and phasic actomyosin contractions was observed.

All tested inducements of $[Ca^{+2}]_i$ oscillations produced phasic contractions in the F-actin networks, suggesting that this is a universal response to Ca^{+2} signaling in osteocytes, rather than from a specific type of Ca^{+2} receptor or store. Our laboratory previously determined that $[Ca^{+2}]_i$ oscillations from fluid shear flow come from different sources of Ca^{+2} depending on the spike number (Lu, Huo et al. 2012).

In Chapter 4, the intracellular mechanics of the actin and MT networks were determined in the first 10 seconds of flow onset. With the additional tracking of $[Ca^{+2}]_i$, a $[Ca^{+2}]_i$ spike was observed after > 8 seconds of flow. The strain developed before a measurable $[Ca^{+2}]_i$ spike was variable between cells in all measured strains, and a minimum strain threshold to activate $[Ca^{+2}]_i$ signaling was not observed. However, given that oscillatory flow stimulates less $[Ca^{+2}]_i$ oscillations than steady flow and develops a lower magnitude of viscoelastic strains, some aspect of the strain magnitude, perhaps in the initial step of flow onset, over this pre-spike period may play a role in the activation of the mechanosensitive Ca^{+2} channels or ER store release of Ca^{+2}. The presence of cortical actin networks rather than thick stress fibers in flattened osteocytes presumably decreased the cell modulus and allowed contractile behavior to be observed.

The relaxation time for the Ezz contraction under ATP stimulation was on the order of 150-200 seconds, which generally coincides with the time between $[Ca^{+2}]_i$ oscillations in osteocytes under fluid shear flow (Lu, Huo et al. 2012). Hence, the kinetics of contraction and $[Ca^{+2}]_i$ signaling are synced as slow, phasic, “twitching” contractions rather than tonic, sustained contractions (Sanderson, Bai et al. 2010).

Due to the physical proximity of osteocytes and muscle cells, endocrine and paracrine effects between the two have been implicated (Bonewald 2011). New studies

now suggest a similarity between osteocytes and myocytes in gene expression and development. Recent studies have discovered the role of muscle-related factors in osteocyte function (Juffer, Jaspers et al. 2012; Kramer, Baertschi et al. 2012) and genes traditionally considered osteocyte-specific, such DMP1 and E11, are also expressed in vascular smooth muscle cells in certain contexts (Zhu, Mackenzie et al. 2011). A new potential avenue of study is in the role of TGFβ1 in osteocyte contraction, as it has a role in contractile phenotype development in vascular smooth muscle cells (ten Dijke and Arthur 2007) and has been shown to be an important player in bone (Tang, Wu et al. 2009; Yang, Harris et al. 2009).

While mRNA gene expression data suggested the presence of both skeletal and smooth muscle contractile proteins, our western blots show only smooth muscle proteins in both MLO-Y4 and primary osteocytes. The implications of having smooth muscle myosin ATPase in osteocytes requires further study. It remains to be seen if the cytoplasmic $[Ca^{+2}]_i$ oscillations can induce contraction in the osteocyte processes in a similar manner. It is plausible that the presence of a muscle myosin may allow long-range contractions within an osteocyte allowing the osteocyte processes to mechanically slide in the canaliculae. This Ca^{+2} -driven mechanical contraction of the actin-rich processes may be another unexplored avenue of autocrine-like mechanotransduction in osteocytes (Wang, McNamara et al. 2007). The failure to detect troponins does not exclude the possibility of the presence of skeletal or cardiac muscle proteins. Low protein expression levels undetectable by western blot may exist and influence the contractility of osteocytes. The gene expression data of Paic et al. (Paic, Igwe et al. 2009) suggested a troponin-mediated control of contractility, and low levels of troponin may still be able to modulate

contractility. Our group tested a skeletal and cardiac calcium sensitizer that targets troponin I, levosimendan, and found higher contractions in osteocytes (data not shown). Whether this was due to off-target effects of the drug or interactions with a low level of troponin remains to seen, however.

In conclusion, a novel Ca^{+2}-dependant contractile phenotype has been characterized in MLO-Y4 osteocytes. Evidence suggests this contractility is also present *in vivo* when osteocytes are embedded in the lacunocanalicular matrix. Possible interactions with mechanotransduction pathways are numerous and deserve further study using mouse knockout and knock-in models that target smooth muscle-related genes in osteocytes. Ultimately, the relationship between osteocyte contractions and bone development and remodeling deserves further study.

4.5 Figures

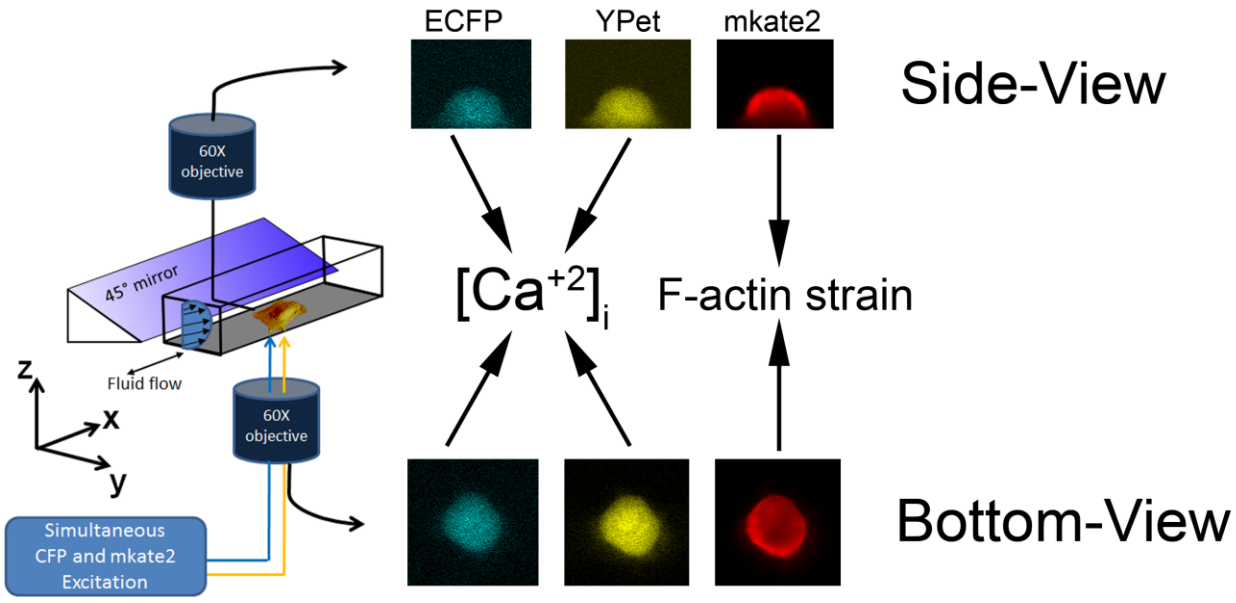

Figure 4.1: Schematic of the multi-channel quasi-3D microscope technique used in the study. Beamsplitters allowed simultaneous acquisition of a ECFP/YPet Cameleon biosensor and an mkate2-Lifeact fusion plasmid. $[Ca^{+2}]_i$ and F-actin network strains were recorded over time in a single osteocyte cell. A syringe pump connected to the imaging chamber allowed controlled entry of fluid for drug or fluid shear flow studies while imaging.

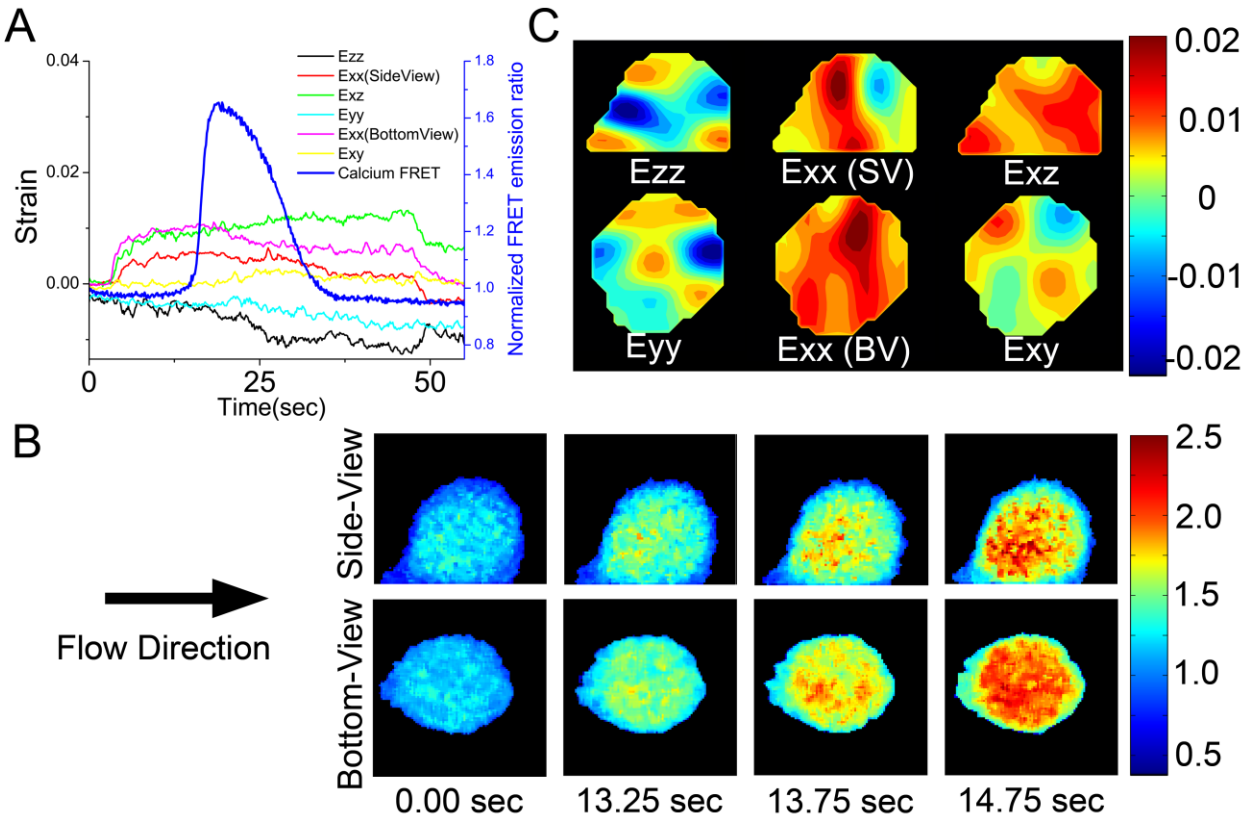

Figure 4.2: Sample osteocyte under 2 Pa fluid shear flow with actin strains and $[Ca^{+2}]_i$. (A) Time course of actin strains and $[Ca^{+2}]_i$. Creep strains develop immediately after the onset of flow @ 5 seconds. A $[Ca^{+2}]_i$ spike occurs ~8 seconds after the onset of flow. (B) FRET emission ratios of the Cameleon $[Ca^{+2}]_i$ biosensor at various timepoints depicting possible $[Ca^{+2}]_i$ spark initiation point. (C) Corresponding actin strain contour plots @ 13.75 seconds.

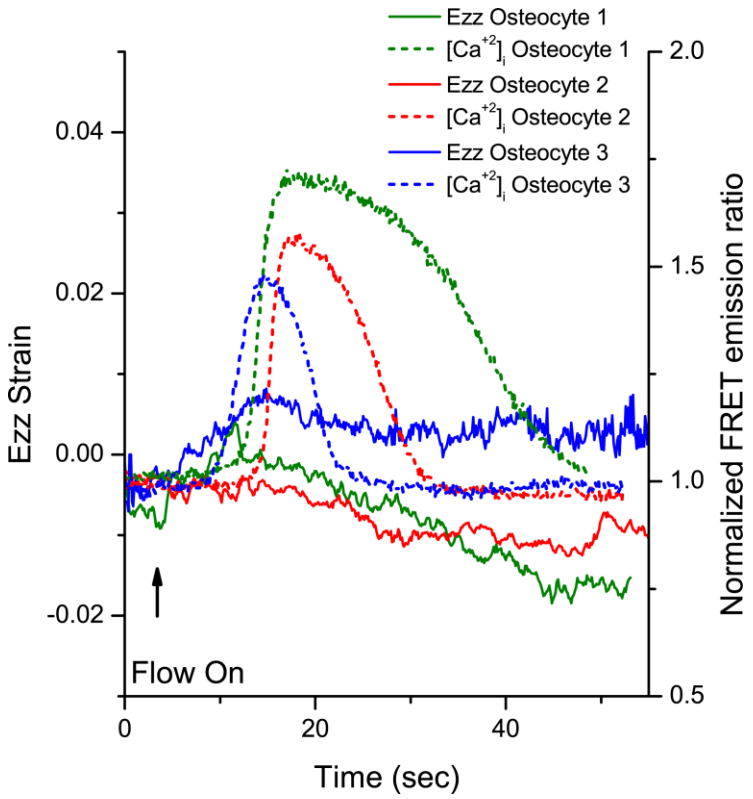

Figure 4.3: Sample curves of $[Ca^{+2}]_i$ and Ezz actin strain in 3 osteocytes. Upon flow onset, creep is visible in 2 of the cells. A $[Ca^{+2}]_i$ occurs ~8-10 seconds after onset of flow. Ezz decreases after the initiation of the $[Ca^{+2}]_i$ spike. The contraction in Ezz counteracts the flow-induced tensile strains.

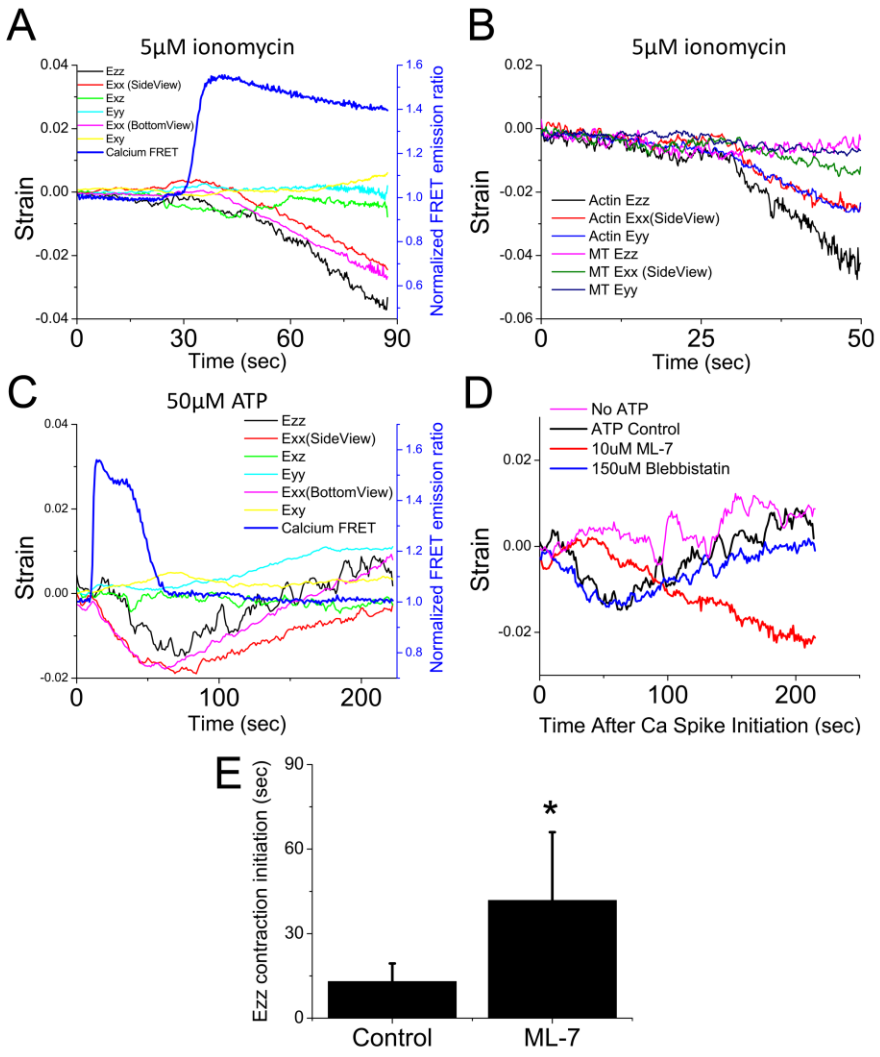

Figure 4.4: (A) Addition of 5μM ionomycin induces step increase in $[Ca^{+2}]_i$ and subsequent compression in actin normal strains, but not shear strains, indicative of whole-cell contraction. (B) Actin and MT networks tracked during the addition of 5μM ionomycin. The decrease in actin normal strains are higher than in the MT networks for each measured strain. (C) 50 μM ATP induces $[Ca^{+2}]_i$ spike and reversible actin compression in normal strains. (D) Ezz strain timecourse of sample cells treated with no ATP, ATP, ATP+ML-7, or ATP+blebbistatin. ML-7 increased the time to initiate a whole-cell contraction. (E) Quantification of contraction initiation time. * = $p < 0.05$.

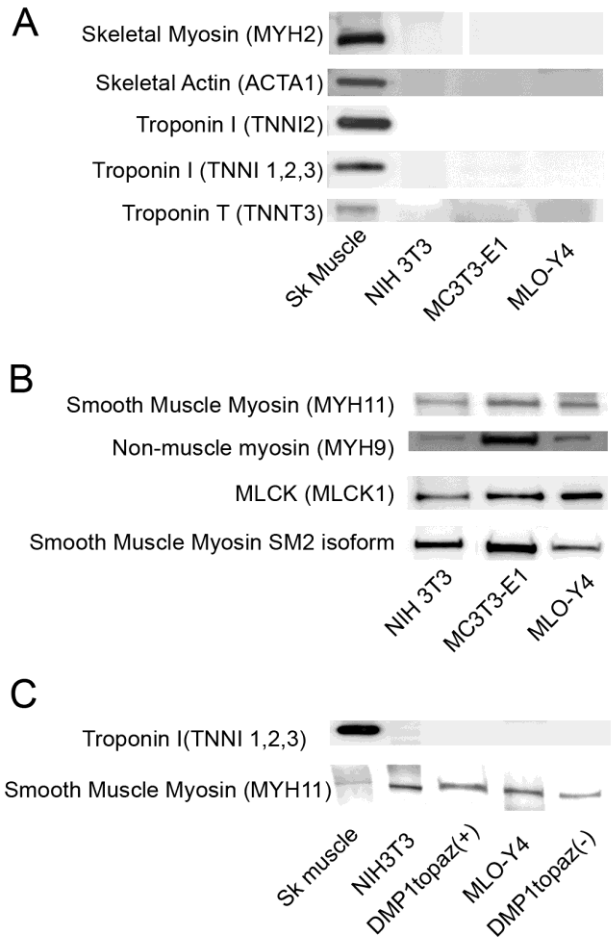

Figure 4.5: Western blots for (A) skeletal muscle contraction related proteins, (B) smooth muscle related proteins. Skeletal muscle lysate and NIH3T3 lysates were used as positive or negative controls. (C) Confirmation of MLO-Y4 cell line results using FACS sorted primary osteocytes (DMP1topaz(+)) for troponin I and smooth muscle myosin. Smooth muscle, but not skeletal muscle, contractile proteins were detected in this assay.

Chapter 5. Summary and Future Studies

5.1 Summary

The objective of this thesis was to develop a novel quasi-3D microscopy technique to investigate early spatiotemporal mechanics of the cytoskeleton and of the signal activation of mechanotransduction pathways in osteocytes. The work attempted to connect the "mechano" and the signal transduction aspects of the osteocyte to help understand how tissue-level mechanical forces are perceived by the osteocyte and how it progresses towards a downstream biological pathway. Optics, fluorescence microscopy, molecular biology, and image processing techniques were integrated to investigate three distinct mechanobiological questions. At the end of this thesis work, new fundamental questions have arisen based on new findings on osteocyte behavior.

5.1.1 Quasi-3D Development and Application to MLO-Y4 Osteocytes Under Steady Fluid Flow

Osteocytes respond to dynamic fluid shear loading by activating various biochemical pathways, mediating a dynamic process of bone formation and resorption. Whole-cell deformation and regional deformation of the cytoskeleton may be able to directly regulate this process. Imaging cellular deformation by conventional microscopy techniques has been hindered by low temporal or spatial resolution. This study developed a "quasi-3D" microscopy technique that achieved simultaneous visualization of an osteocyte's traditional "bottom-view" profile along with a "side-view" profile at a high temporal resolution. Quantitative analysis of the plasma membrane and either the intracellular actin or microtubule (MT) cytoskeletal networks provided characterization

of their deformations over time. While no volumetric dilatation of the whole cell was observed under flow, both the actin and microtubule networks experienced primarily tensile strains in all measured strain components. Regional heterogeneity in the strain field of normal strains was observed in the actin networks, especially in the leading edge to flow, but not in the MT networks. In contrast, side-view shear strains exhibited similar subcellular distribution patterns in both networks. Disruption of microtubule networks caused actin normal strains to decrease, while actin disruption had little effect on the microtubule network strains, highlighting the networks' mechanical interactions in osteocytes.

5.1.2. Actin and Microtubule Network Deformations in Single MLO-Y4 Osteocytes Under Steady and Oscillatory Flow

Osteocytes *in vivo* experience complex fluid shear flow patterns to activate mechanotransduction pathways. The actin and microtubule (MT) cytoskeletons have been shown to play an important role in the osteocyte's biochemical response to fluid shear loading. The dynamic nature of physiologically relevant fluid flow profiles (*i.e.* 1 Hz oscillatory flow) impedes the ability to image and study cytoskeletal behavior simultaneously in the same cell with high spatiotemporal resolution. To overcome these limitations, a multi-channel quasi-3D microscopy technique was developed to track the actin and MT networks simultaneously under steady and oscillatory flow. Cells displayed high intercellular variability and intracellular cytoskeletal variability in strain profiles. Shear Exz was the predominant whole-cell strain in both steady and oscillatory flows, in the form of viscoelastic creep and elastic oscillations, respectively. Flow-directional differences in whole-cell strain development under steady flow between the actin and MT

networks were observed in shear Exz and Ezz strains. The actin strains displayed an oscillatory strain profile more often than the MT networks in all the strains tested and had a higher peak-to-trough magnitude. At the subcellular level, large strains were visible in both the actin and MT networks with differences in the leading edge to flow in steady flow. Taken together, the actin networks are the more responsive cytoskeletal networks in osteocytes under oscillatory flow and may play a bigger role in mechanotransduction by having longer range mechanical influences.

5.1.3. $[Ca^{+2}]_i$-Dependent Actomyosin Contractility in Osteocytes Mediated by Smooth Muscle Myosin

Osteocytes are mechanosensory cells in bone with robust intracellular calcium ($[Ca^{+2}]_i$) oscillations in response to fluid shear stresses, hormones, and autonomously in vivo. While many distant downstream pathways of $[Ca^{+2}]_i$ signaling have been studied, the immediate, temporally regulated effects of $[Ca^{+2}]_i$ oscillations in osteocytes have not been investigated. Here, we demonstrate novel osteocyte mechano- and transduction behavior where $[Ca^{+2}]_i$ oscillations activate phasic actomyosin contractions using a smooth muscle-like mechanism. Using a quasi-3D imaging technique, $[Ca^{+2}]_i$ and F-actin network strains were tracked simultaneously in a single osteocyte. Fluid shear, ATP, and ionomycin induced $[Ca^{+2}]_i$ signaling with a subsequent compression and recovery in actin strains of the cell, being most apparent in the Ezz height strain. This contraction was reversible over the period of hundreds of seconds. ML-7, a myosin light chain kinase inhibitor, significantly slowed down the kinetics of contraction initiation, but blebbistatin, a potent skeletal and non-muscle inhibitor, had no effect on the actin contraction. Furthermore, smooth muscle contraction-related proteins were detected by Western blot.

Muscle-like contractility in osteocytes represent a novel mechanical behavior that may interface with muscle-related signaling pathways.

5.2 Future Studies

Osteocyte mechanics remains understudied in several aspects: filopodia/processes mechanics, extracellular matrix interactions, mechanotransduction *in vivo*, and relationships to muscle. Here, we propose several studies that would naturally follow from the findings of the presented thesis.

5.2.1 Osteocyte Mechanics

This thesis focused on the mechanics of the osteocyte cell body in a spherical *in vivo* mimicking shape. Osteocyte mechanobiology has mainly focused on the dendritic processes while ignoring the cell body. A future investigation into the roles of dendritic processes and cell body communication can be implemented using the multi-channel quasi-3D setup. Preliminary experiments in our lab have used soft contact lithography to micropattern various shapes for controlled osteocyte attachment on a glass substrate. It is possible to create a pattern such that a single osteocyte produces several dendritic processes while maintaining a spherical or ellipsoidal cell body. Using this technology in conjunction with the quasi- 3D technique will allow simultaneous visualization of dendrites and cell body. The high temporal resolution of the quasi-3D technique can capture $[Ca^{+2}]_i$ sparks or waves that propagate through the cell. Mapping signal activation within the cell can produce a better picture of how mechanical signals are transduced into biological signals (Na, Collin et al. 2008). The advances in FRET biosensor technology also opens doors to tracking mechanically regulated kinases. Two key early players that are activated by mechanical stimulation are Src kinase and focal adhesion kinase (FAK)

(Li, Kim et al. 1997; Wang, Botvinick et al. 2005; Na, Collin et al. 2008; Young, Gerard-O'Riley et al. 2009). Studies have shown an intimate physical and pathway connection between the two in modulating many cellular processes in bone cells (Xing, Chen et al. 1994; Plotkin, Mathov et al. 2005; Young, Gerard-O'Riley et al. 2009; Rangaswami, Schwappacher et al. 2010; Young, Hum et al. 2011). Furthermore, both kinases are known to be closely associated with the intracellular actin and microtubule cytoskeletal networks, which are responsible for giving the cell its mechanical properties. Therefore, the relationship between the mechanical structural networks in the cell and signal transduction in mechanical loading is of interest for future studies.

5.2.1 Osteocyte *in vivo*

One limitation of the current thesis is the usage of *in vitro* studies and cell lines to investigate osteocyte behavior. However, the *in vivo* osteocyte microenvironment is quite complex with its unique, entombed extracellular matrix and subsequent reduced fluid and nutrient transport. The number of osteocyte dendritic processes *in vivo* can be close to one hundred per cell. Therefore, any *in vitro* finding must be verified in an *in vivo* context. The difficulty in culturing primary osteocytes without losing phenotype or imaging osteocytes *in vivo* has severely hindered progress in observing live osteocyte behavior. Intravital imaging of osteocytes in bone is a possibility (Pittet and Weissleder 2011), with advantages of having the native environment of endocrine, sympathetic/parasympathetic, and vascular systems intact. However, a somewhat simpler method that has been utilized in the past is *ex vivo* calvarial or long-bone imaging. Unmineralized calvariae are transparent enough to allow deep light penetration to perform fluorescent microscopy (Adachi, Aonuma et al. 2009; Ishihara, Sugawara et al. 2012). Studies in our laboratory

have been able to use standard laser-scanning confocal microscopy to image osteocytes in tibial long bone to a depth of ~100μm, where a large number of osteocytes reside. The simplicity of imaging a single segment of bone tissue allows purely osteocyte mechanotransduction to be studied with minimal effects from other organs. One immediate experiment from the thesis to be repeated *ex vivo* is to measure actin strains under mechanical loading of bone. Bone from a transgenic mouse with the same Lifeact F-actin probe used in Chapter 3 and 4 can be dissected and imaged directly (Riedl, Flynn et al. 2010). The mechanical behavior of dendritic and cell body osteocyte F-actin networks *in situ* will bring new insights on how actin networks transduce substrate and fluid shear based strains.

5.2.3. Osteocyte Contractility

The novel observation that osteocytes contain smooth muscle myosin heavy chain (SMMHC) begs the question of its role in osteocyte biology. The implications of this finding have yet to be determined but may be related to osteocyte function *in vivo*. A hallmark of all forms of muscle is $[Ca^{+2}]_i$-dependent actomyosin contractility. Many muscle types exhibit phasic contractility that is regulated by periodic Ca^{+2} oscillations. These temporal patterns of Ca^{+2} oscillations are remarkably similar to the patterns seen in osteocytes. Furthermore, factors involved in SMMHC contractility development, such as MEF2C and TGFβ1, have also been shown to be important in bone physiology (Tang, Wu et al. 2009; Kramer, Baertschi et al. 2012). Therefore, we hypothesize SMMHC actomyosin contractility in osteocytes may interface with osteocyte signaling and function. The first study to consider whether $[Ca^{+2}]_i$-dependent actomyosin contractility occurs when osteocytes are in bone tissue. Using the Lifeact mouse and an *ex vivo* system

as described in the previous section will be able to verify this phenomenon. It will be interesting to see if dendritic processes can contract and slide in the canaliculae. The findings will introduce new potential mechanical signals that osteocytes may be able to generate to activate mechanotransduction pathways.

A larger, more involved, but rewarding study is a transgenic conditional knockout of the SMMHC gene in osteocytes. As SMMHC knockouts are lethal to newborn pups, a conditional knockout using a DMP1-Cre or SOST-Cre to ablate osteocyte SMMHC activity can be created to observe the skeletal phenotype using microCT, histomorphometry and *in vitro* assays. We hypothesize that ablation of osteocyte SMMHC will create defects in bone remodeling by interfering with osteocyte paracrine signaling to osteoblasts and osteoclasts. Ultimately, the goal of this future study would be to determine a functional role of osteocyte actomyosin contractility; mechanical contractions may play a role in the "mechanotransduction" pathways established as crucial in osteocyte function, including Ca^{+2}/CaM, Wnt, and PGE_2.

Appendix A. Validation of a Quasi-3D Microscopy Technique to Track Intracellular Deformation

A.1 Introduction

Experimental and theoretical studies have shown that cellular deformation of cells under fluid flow is inhomogeneous and location and height dependent (Helmke, Rosen et al. 2003; Adachi, Aonuma et al. 2009), highlighting the importance of accurately measuring intracellular strains in 3D. For adherent cells under fluid flow, the interactions between the flow field, the cell, and the substrate are dynamic and complex. The conventional inverted-view microscopy of cell deformation is insufficient to characterize the intracellular deformation of the adhered cells at their apical surface and at their basal surface under flow. In addition, cellular mechanotransduction events in response to mechanical stimuli are still poorly understood, especially at the initial events of biochemical signal activation and transduction.

The recent progress in the development of a wide range of green fluorescent protein (GFP) color variants (such as cyan fluorescent protein (CFP), red-colored mCherry, far-red mPlum, etc.) has allowed the ability to use multiple fluorescent protein colors simultaneously in the same cell to label intracellular structures (Davidson and Campbell 2009). This has led to the development of genetically encoded fluorescence resonance energy transfer (FRET) biosensors that utilize fluorescent proteins to directly measure the cellular activity of kinases or proteases by optical microscopy.

Studies involving FRET biosensors and mechanotransduction have shown that mechanically-regulated activations of signaling kinases are on the order of milliseconds

and spatiotemporally heterogeneous (Tzima, Del Pozo et al. 2002; Na, Collin et al. 2008; Hu;, Li; et al. 2010). Few studies have correlated the mechanical response of a cell to its dynamic activation of signaling pathways, partially due to limitations in capturing the near-instantaneous events of deformation and signal activation upon mechanical stimulation (Na, Collin et al. 2008).

Obtaining reasonable 3D cell information using spinning-disk or laser scanning confocal microscopy technologies takes approximately 0.5 to 0.8 seconds. The limitation of the z-stack scanning speed makes the confocal microscope a non-ideal choice to image events requiring a higher temporal resolution, such as the imaging of osteocytes sheared at a 1Hz oscillatory loading frequency, which require at least 8 full frames per second to adequately cover the 1 Hz loading profile (Wang, Hu et al. 2007).

To address these limitations, we have developed a multi-channel quasi-3D microscopy technology that is capable of simultaneously obtaining up to 4 different fluorescent emission bands at ~12-15 Hz in two orthogonal planes of a cell in parallel. Using this novel technology, mechanotransduction will be observed at an early timescale that traditional techniques have had difficulty in imaging, thereby helping to elucidate the spatiotemporal dynamics of the conversion of mechanical signals into biochemical signals. The objectives of this study were to 1) develop a multi-channel quasi-3D microscopy technique, 2) validate an image-based digital image correlation technique using a computational FEA-based simulated cell to obtain intracellular strains.

A.2 Methods

A.2.1 Quasi-3D Microscopy Technique

A custom-designed dual-microscope system consisting of an Olympus IX-71 inverted microscope (for conventional top-bottom view) and an Olympus BX-2 upright microscope (for side-view) are used in this thesis proposal. A custom-built device is employed to align an enhanced silver coated mirror at 45° in the light path of the BX-2 microscope to obtain the side view images of a cell (Fig. A.1). The IX-71 microscope is used to obtain the "bottom-view" image of the cell body. Therefore, two orthogonal wide-field images of a cell are obtained in parallel. Fluorescence images are synchronously recorded for both microscopes using two cooled EMCCD cameras (iXon 885. Andor, AZ), one Lambda DG-4 Ultra High Speed Wavelength Switcher Xenon lamp (Sutter Instrument Company, Novato, CA), one Far-Red LED lamp (M780L2, ThorLabs, Newton, NJ) and two 60X long working distance objectives (Olympus, Japan). Two Quadview emission beam splitters (Photometrics, Tucson, AZ) are placed in the emission light path of both bottom- and side- view microscopes. This setup has the advantages of synchronized 4-channel imaging in both bottom view and side view to obtain multi-wavelength "quasi-3D imaging."

The 4 emission channels in the Quadview systems use commercially available dichroic mirrors and emission filters from Chroma Corporation to provide the following: CFP emission, YFP emission, mKate2 emission, and Far Red/Infrared emission. Taking advantage of the fact that most designed FRET biosensor require only CFP excitation, the Xe and LED light sources will provide 3 excitation bands. CFP excitation, mKate2

excitation, and Far Red/Infrared excitation will be provided by a combination of commercially available single and dual bandpass excitation filters.

A.2.2 Digital Fluorescence Algorithm

To mimic the light properties of randomly distributed intracellular fluorescent dye particles, randomly distributed points in 3D space in an object were treated as particle point sources of light with an assigned value of light intensity. The mean fluorescent light intensity for a cell measured in our quasi-3D images was used to mimic that of a simulated cell. However, the light intensity of each individual particle was assigned a randomly generated value from a Gaussian distribution. The light intensity values generated by the Gaussian distributor were in the same range as those typically seen in experimentally obtained quasi-3D images in our system. A distance decay function was adopted to assign the light intensity from each particle point to a surrounding 5×5×5 image pixel grid to create a nonuniform light intensity pattern similar to fluorescent images of cells with punctate structures ~1 μm in size. The distance between two adjacent grid points, *i.e.*, the image pixel resolution, was the same as the quasi-3D system, 0.215μm. The distance decay function was:

$$I_d(z) = I_0(0) \times f(z) = I_0(0) \times \frac{2}{\pi}\left[\cos^{-1}\left(\frac{z}{\alpha}\right) - \left\{\left(\frac{z}{\alpha}\right)\left(1-\left(\frac{z}{\alpha}\right)^2\right)\right\}^{1/2}\right], z < \alpha$$

where $I_0(0)$ is the initial light intensity and the parameter α is the bandwidth. We set α=10 μm. z is the distance from the points (i, j) to the adjacent point (i + Δi, j + Δj). From this procedure, a "virtual", simulated 3D fluorescently dyed cube or a hemi-spherical cell-like object was created. By running the Gaussian random light intensity value generator several times, five sets of virtual cubes or hemi-spherical cells (n=5 each)

were created for subsequent processing and analyses. The cube and cells were then convolved with a PSF function as detailed in A.2.5. The edge length of the cube was 15 μm, and the diameter of the cell was about 15 μm as well. The realistic cell 3D shape was reconstructed from previous quasi-3D cell membrane images (Baik, Lu et al. 2010). It should be noted that the spatial positions of the fluorescent dye particles were used for nodes of tetrahedral elements in the finite element model of the same cell to precisely prescribe cellular deformations.

A.2.3 Deformed Cube Images

In order to precisely create deformation of the cube, we created a 15μm cube finite element model using commercial finite element software ADINA 8.6.2 (ADINA R&D, Waterman, MA). The fluorescent particle points were used as nodes of the tetrahedral elements in the model. The size of each element was about 1μm. Three uniaxial tensile (E_{xx}, E_{yy}, and E_{zz}) and two uniaxial shear strain conditions (E_{xy} and E_{xz}) were applied to the model. The uniaxial strains in the cube were homogeneous in the applied direction. A linear elastic solid model was adopted as the constitutive cube material model. The Young's modulus was set as 1kPa, and the Poisson's ratio was 0.45.

Appropriate uniaxial displacement boundary conditions were imposed to ensure uniaxial tension or shear strains. The cube was deformed in 20 uniform incremental deformation steps. All the element nodes were deformed within the whole cube. Therefore, the deformed positions of fluorescent particle points were tracked and used to generate the corresponding simulated deformed images of the cell. Uniaxial strain and simple shear cases were applied to the cube model in directions corresponding to the

measurable strains in the quasi-3D technique (*i.e.*, E_{xx} bottom-view, E_{xy}, E_{zz}, E_{yy}, E_{xx} side-view, and E_{xz}).

A.2.4 Realistic Cell Images under Fluid Flow Deformation

The fluorescent particle positions of a 3D realistic cell were used as nodes and input into a fluid-structure interaction finite element model using ADINA. The fluid and solid solution variables were fully coupled. The flow boundary conditions were set to give a wall shear stress of 7 dynes/cm^2 in a tube of the same rectangular cross-section as in our previous experimental study. Flow was applied for 10 seconds in the FEA model followed by a 10 second rest period. The cell was deformed in 27 steps with the same incremental deformation amplitude over 20 seconds. The deformed positions of fluorescent particle points were tracked and used to generate the corresponding simulated images of the deformed cell.

A.2.5 Quasi-3D Image Simulation and Strain Calculation

The quasi-3D technique consists of two wide-field fluorescent microscopes that can simultaneously and independently obtain 2D images of a cell in the orthogonal "bottom-view" x-y and "side-view" x-z planes. To mimic this image technique, the 3D simulated fluorescent images (n=5 for either cube or cell images) were convolved with a PSF onto x-y or x-z plane slices for creating simulated bottom or side view fluorescent wide-field microscopy images for quasi-3D analysis. The PSF describes the response of an imaging system to a point source or point object of light. With linear optics, the image of a complex object can then be seen as a convolution of the true object and the PSF. In this case, the "true" object was the simulated image of a cell. With information of the specific PSF for our microscopy system, we generated 2D bottom or side views of the

cell. We adopted a PSF that used an analytical derivation using Fraunhofer diffraction along with a .7 Numerical Aperture, 60X magnification, 510 nm wavelength of emission light, and CCD pixel size (12.9 μm), to generate a 3D PSF (Ohkubo, Wada et al. 2006; Marian, Charriere et al. 2007; Gardner, Sprague et al. 2010). The convolution of the PSF and the light intensity matrix containing the cell and all related calculations were performed in MATLAB 2009b (The Mathworks, Natick, MA). Furthermore, to test the effect of general types of image noise on the accuracy of the PSF and digital image correlation, additive steps of Gaussian noise were uniformly applied to the quasi-3D image slices of the cell model under fluid shear to decrease the SNR. SNR was defined as the mean intensity of the inside of the cell subtracted by the mean of the background non-cell region, divided by the standard deviation of the background. Convolved sets of quasi-3D images of the object and its deformed states were processed to obtain strain fields according to a previously established technique (Pan, Xie et al. 2007). Briefly, each deformed image was compared against the original using a digital image correlation technique to obtain displacement fields inside the object. The displacement fields were smoothed and differentiated using a bilinear least squares filter and then Lagrangian strains were determined. The E_{xx}, E_{yy}, and E_{xy} were calculated for the bottom-view images, and E_{zz}, E_{xx}, and E_{xz} were calculated for the side-view images. These average quasi-3D strains were compared with the finite element prescribed strain values.

A.3 Results

A.3.1 Quasi-3D Microscopy Construction

The schematic of the design of the multi-channel quasi-3D microscopy technique is presented in Figure A.1A. Using quad view beamsplitters, 4 separate fluorescent channels are able to be imaged simultaneously. A custom-made polychroic mirror (Fig. A.1B) was fabricated to allow the proper filtering of all the channels. Furthermore, the beamsplitters are removable, allowing full-frame images of single fluorescent dyes. A sample image showing the quasi-3D technique is provided in Figure A.2. The side-view microscope focused on different x-z planes to provide cross sectional images of the beads in the x-y image.

A.3.2 Cube Cell Model under Uniaxial Strains

A homogeneous uniaxial strain model of a cube and a heterogeneous shear flow model of a cell coupled with a digital fluorescence algorithm were successfully created. These 3D models were convolved with a PSF function specific for the experimental quasi-3D setup (Baik, Lu et al. 2010). Sample 2D PSF-convolved images of the fluorescent cube and cell before and after deformation are shown in Figure A.3. It should be noted that the precise deformation of these simulated images was known and was able to be compared with quasi-3D calculations.

Six different uniaxial strain or pure shear cases were applied to the PSF-convolved simple cube model. The applied strain was then calculated in the middle plane of the cube in the view that the applied strain was visible (*e.g.* E_{zz} was measured using the side-view x-z plane). The results are presented in Table A.1. The quasi-3D calculated strains closely matched the prescribed strains (from FEA) in the simple cube model in

both uniaxial and shear strain cases. The relative error for these measurements was less than 5%.

A.3.3 Realistic Cell Model under Fluid Flow

The 3D cell fluid-structure interaction finite element model was used to investigate the whole-cell strains of a simulated cell under fluid shear loading. In the FEA simulation, average strains of the whole cell were calculated for each time point. Whole-cell E_{xz} showed viscoelastic creep and creep recovery strain effects from the fluid flow, but near-zero strains were observed in all other 3D FEA strain components (Fig. A.4). The cell model was then convolved with a PSF, and the quasi-3D strains were calculated from selected planes in the bottom-view x-y and side-view x-z. Near-zero strains were observed in the bottom-view x-y plane, but significant strains were seen in side-view x-z plane (Fig. A.4). Overall, the calculated quasi-3D strains were similar to the FEA strains inside the cell. Whole-cell E_{xz} showed large viscoelastic behavior from the fluid flow, while the E_{zz} and E_{xx} side-view strain components hovered near zero throughout the flow pattern. However, the E_{zz} was slightly overestimated during the flow period (Fig. A.4 A).

A minimum SNR of 12 was necessary to maintain accurate strains with a mean error of less than .004 (Fig. A.5). At an SNR of 9 and lower, the mean strain error jumped to greater than .01. Interestingly, while normal strains were inaccurate at a SNR of 9, shear strain accuracy was relatively unaffected at an SNR 9.

A.4 Discussion

This study focused on developing a quasi-3D microscopy technique and validating the accuracy of quasi-3D strains against the real 3D deformation within a cell from a theoretical perspective. The versatility of the quasi-3D system is in its spatiotemporal resolution. As FRET-based mechanical changes can occur on the millisecond timescale (Na, Collin et al. 2008; Poh, Na et al. 2009), the multichannel quasi-3D technique would be able to capture this near-instantaneous behavior.

A computational model was developed using parameters from experimentally obtained quasi-3D images to be able to directly compare prescribed 3D strains in a cell-shaped model versus their quasi-3D counterparts. A finite element model of a cube and cell was deformed with simple and complex deformation patterns. Each deformation state was then convolved with a PSF and then quasi-3D images were extracted and processed to obtain quasi-3D strains.

The quasi-3D strains correlated well with the prescribed 3D strain values in both uniform uniaxial and shear cases and also in realistic fluid flow-induced deformation. The computational model was able to determine how the PSF affects wide-field microscopy-based measurements of strains. The additional error from the PSF was less than 5%, showing that the quasi-3D technique can accurately capture 3D deformations of a cell. A lower SNR limit of 9 was determined in this model system when calculating normal strains. This SNR limit was lower than other simulated image studies involving digital image correlation (Zhou and Goodson 2001). However, most studies focus on displacement error as an output of SNR. The output in this study was strain, a differentiated value of the displacement field, and may be less sensitive to error due to the

additional smoothing and differentiation operations (Wang, Deng et al. 2002; Pan, Xie et al. 2007). Normal strain errors at an SNR of 9 in Ezz and Exx were higher than in Eyy due to the difficulty of tracking larger displacements in noisy images of the model cell under fluid shear in the z and x directions than in the y direction. Interestingly, shear strain error was relatively unaffected at this SNR value, demonstrating that the accuracy of calculated normal strains may be more sensitive to Gaussian noise than shear strain in fluid shear experiments. This should be considered when determining the acceptable level of noise of wide-field microscopy images used in mechanical analyses of strain.

Several parameters that could potentially influence the accuracy of the quasi-3D calculations were absent from this idealized model. Factors such as photon noise (of a Poisson distribution) and complex inhomogeneous deformation patterns could decrease the ability of quasi-3D strains to accurately represent the real 3D strain. However, this study focused on the main source of error inherent to the quasi-3D system itself, *i.e.*, the blur caused by out-of-focus planes.

The quasi-3D technique represents a novel technique to overcome limitations in temporal and spatial resolution of current microscopy techniques to measure cellular events in 3D. This study provides additional theoretical validation of this novel quasi-3D technique and of wide-field microscopy in calculating strains and deformations in 3D.

A.5 Tables

	Quasi-3D Strain	FEA Strain	Relative Error (%)
E_{zz}	0.0516±0.0007	0.05	3.82±0.80
E_{xx}, side-view	0.0516±0.0005	0.05	3.15±0.99
E_{xz}	0.0318±0.0007	0.0333	4.71±2.20
E_{yy}	0.0517±0.0009	0.05	3.36±1.88
E_{xx}, bottom-view	0.0520±0.0002	0.05	3.98±0.38
E_{xy}	0.0327±0.0010	0.0333	2.04±3.01

Table A.1. Precision study of the components of quasi-3D strain and FEA strain from cube cell model. Quasi-3D strain and relative error represent mean ± s.e.m. (n=5).

A.6 Figures

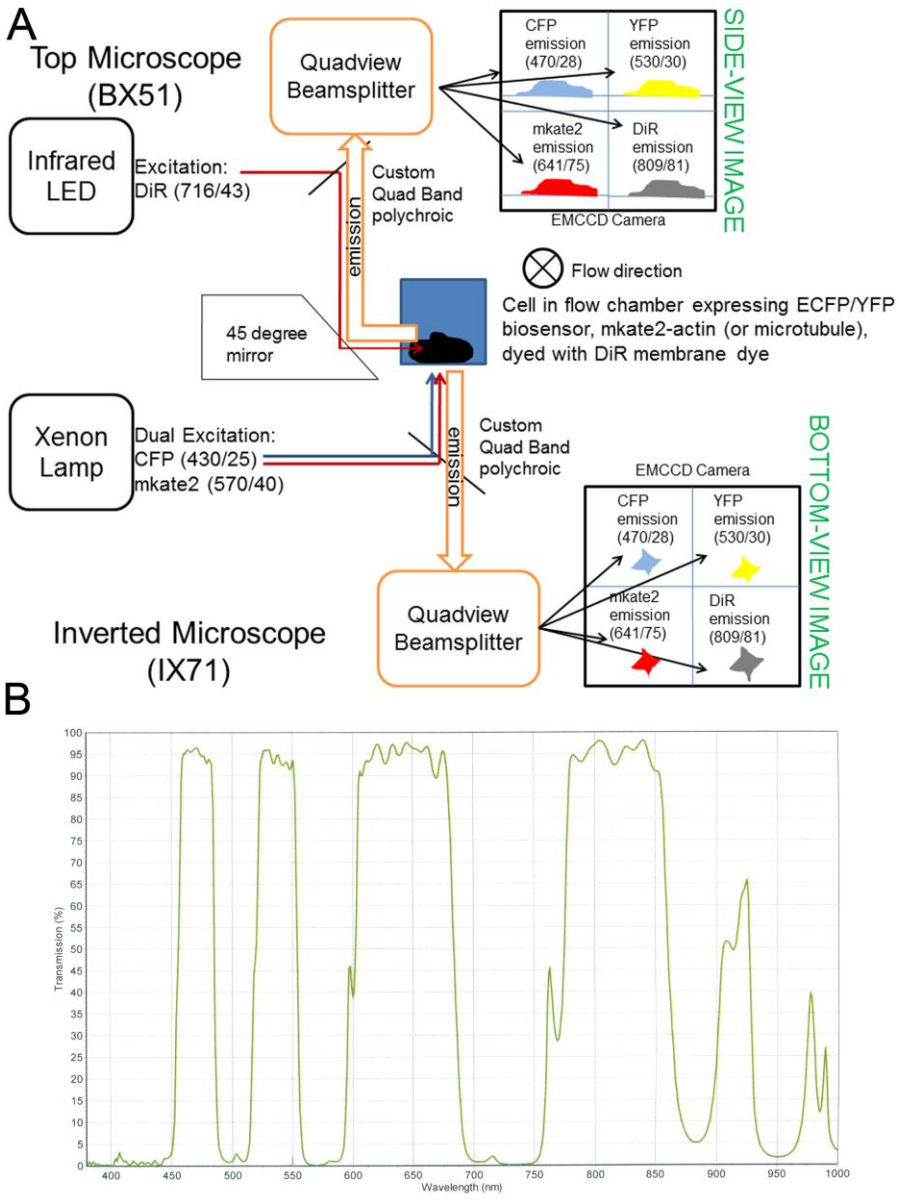

Figure A.1: (A) Schematic of the excitation and emission filters of the multichannel quasi-3D technique. Note that the beamsplitters can be removed to gain a full-frame monochrome image, as used in Chapter 3. (B) Transmission graph of the custom-designed quad band polychroics.

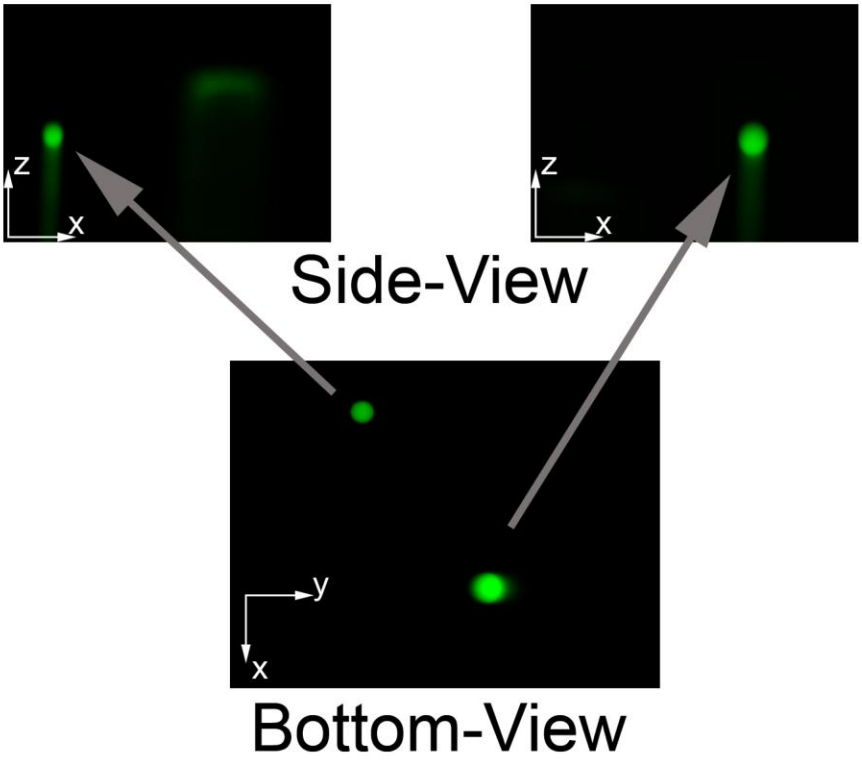

Figure A.2: Proof of concept of the quasi-3D technique. Two distinct fluorescent beads in bottom-view are viewed in side-view by changing the y-focal plane of image. Note the 3D axes.

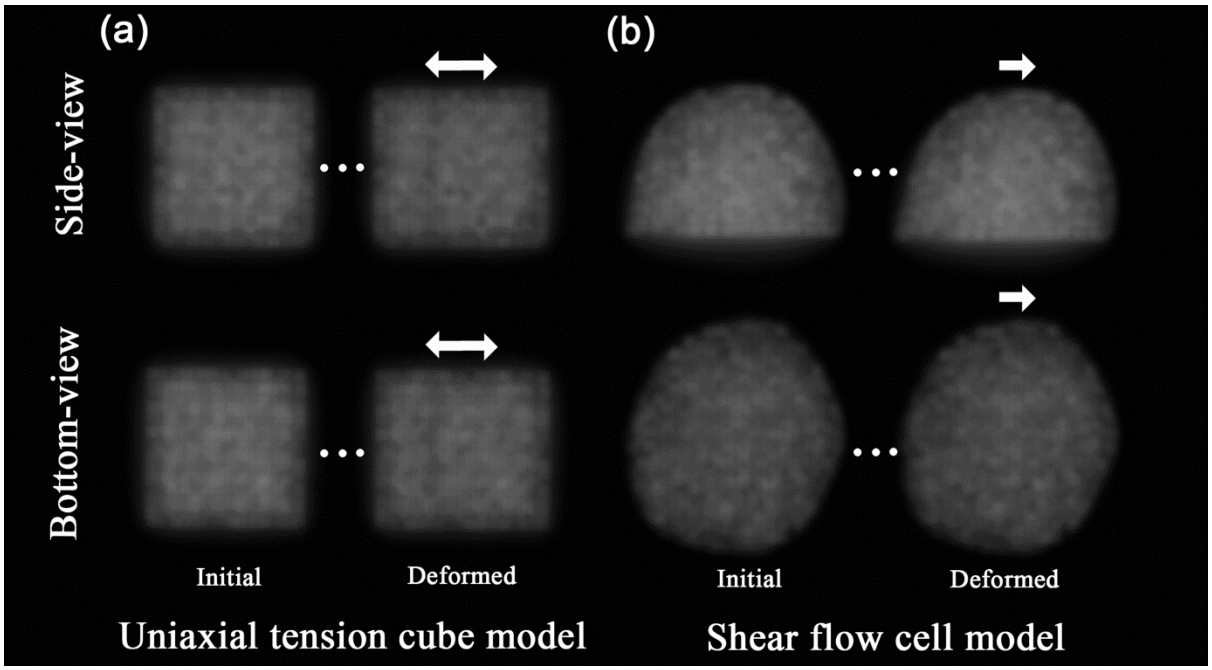

Figure A.3: Cube and cell image simulation. The fluorescently dyed 3D cube or cell was convolved with a PSF, and individual planes were extracted to obtain 2D images. Sample 2D images of the (a) cube and (b) cell are provided before and after deformation by uniaxial tension for the cube and fluid shear for the cell. Arrows represent the direction of deformation.

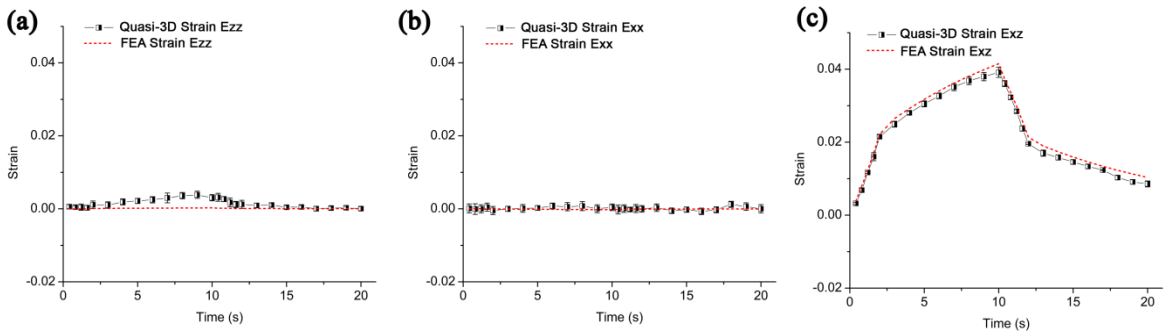

Figure A.4: Time course of whole-cell strains for (a) E_{zz}, (b) E_{xx}, and (c) E_{xz} in the cell shear flow model (n=5). FEA strains are in dashed lines and quasi-3D strains are in half-shaded squares. Viscoelasticity is visible in shear E_{xz} under fluid shear flow. Quasi-3D strains matched well with the FEA strains.

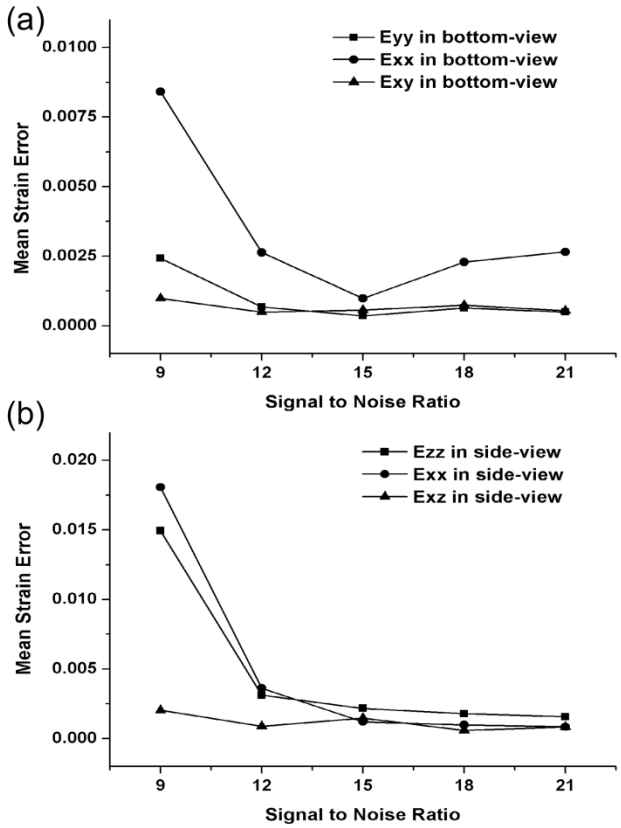

Figure A.5: Means of the absolute error of calculated quasi-3D whole-cell strains in (a) bottom-view and (b) side-view of the simulated cell shear flow model (n=3). Gaussian noise was added to the quasi-3D images prior to the calculation of strains to decrease the SNR. A critical SNR of 9 was found to cause a sharp increase in the error of quasi-3D strains vs. FEA strains, especially in the normal strains.

References

Adachi, T., Y. Aonuma, S. Ito, M. Tanaka, M. Hojo, T. Takano-Yamamoto and H. Kamioka (2009). "Osteocyte calcium signaling response to bone matrix deformation." J Biomech **42**(15): 2507-2512.

Adachi, T., Y. Aonuma, K. Taira, M. Hojo and H. Kamioka (2009). "Asymmetric intercellular communication between bone cells: Propagation of the calcium signaling." Biochemical and biophysical research communications **389**(3): 495-500.

Adachi, T., Y. Aonuma, K. Taira, M. Hojo and H. Kamioka (2009). "Asymmetric intercellular communication between bone cells: propagation of the calcium signaling." Biochem Biophys Res Commun **389**(3): 495-500.

Adachi, T., Y. Aonuma, M. Tanaka, M. Hojo, T. Takano-Yamamoto and H. Kamioka (2009). "Calcium response in single osteocytes to locally applied mechanical stimulus: differences in cell process and cell body." J Biomech **42**(12): 1989-1995.

Ajubi, N. E., J. Klein-Nulend, M. J. Alblas, E. H. Burger and P. J. Nijweide (1999). "Signal transduction pathways involved in fluid flow-induced PGE2 production by cultured osteocytes." Am J Physiol Endo Met **276**(1): E171-E178.

Ajubi, N. E., J. Klein-Nulend, P. J. Nijweide, T. Vrijheid-Lammers, M. J. Alblas and E. H. Burger (1996). "Pulsating fluid flow increases prostaglandin production by cultured chicken osteocytes--a cytoskeleton-dependent process." Biochem Biophys Res Commun **225**(1): 62-68.

Alberts, B. (2008). Molecular Biology of the Cell. New York, Garland Science.

Ando, J., T. Komatsuda and A. Kamiya (1988). "Cytoplasmic calcium response to fluid shear stress in cultured vascular endothelial cells." In Vitro Cell Dev Biol **24**(9): 871-877.

Arnaudeau, S., M. Frieden, K. Nakamura, C. Castelbou, M. Michalak and N. Demaurex (2002). "Calreticulin differentially modulates calcium uptake and release in the endoplasmic reticulum and mitochondria." J Biol Chem **277**(48): 46696-46705.

Bacabac, R. G., D. Mizuno, C. F. Schmidt, F. C. MacKintosh, J. J. Van Loon, J. Klein-Nulend and T. H. Smit (2008). "Round versus flat: bone cell morphology, elasticity, and mechanosensing." J Biomech **41**(7): 1590-1598.

Bae, W. C., C. W. Lewis, M. E. Levenston and R. L. Sah (2006). "Indentation testing of human articular cartilage: effects of probe tip geometry and indentation depth on intra-tissue strain." J Biomech **39**(6): 1039-1047.

Baik, A. D., X. L. Lu, J. Qiu, B. Huo, E. M. Hillman, C. Dong and X. E. Guo (2010). "Quasi-3D cytoskeletal dynamics of osteocytes under fluid flow." Biophys J **99**(9): 2812-2820.

Bonewald, L. F. (2011). "The amazing osteocyte." J Bone Miner Res **26**(2): 229-238.

Bonewald, L. F. and M. L. Johnson (2008). "Osteocytes, mechanosensing and Wnt signaling." Bone **42**(4): 606-615.

Brangwynne, C. P., G. H. Koenderink, F. C. Mackintosh and D. A. Weitz (2008). "Nonequilibrium microtubule fluctuations in a model cytoskeleton." Phys Rev Lett **100**(11): 118104.

Brangwynne, C. P., F. C. MacKintosh, S. Kumar, N. A. Geisse, J. Talbot, L. Mahadevan, . . . D. A. Weitz (2006). "Microtubules can bear enhanced compressive loads in living cells because of lateral reinforcement." J Cell Biol **173**(5): 733-741.

Burger, E. H. and J. Klein-Nulend (1999). "Mechanotransduction in bone--role of the lacuno-canalicular network. [Review] [118 refs]." FASEB Journal **13**(Suppl): S101-112.

Burra, S., D. P. Nicolella, W. L. Francis, C. J. Freitas, N. J. Mueschke, K. Poole and J. X. Jiang (2010). "Dendritic processes of osteocytes are mechanotransducers that induce the opening of hemichannels." Proc Natl Acad Sci U S A **107**(31): 13648-13653.

Cao, J., B. Donell, D. R. Deaver, M. B. Lawrence and C. Dong (1998). "In vitro side-view imaging technique and analysis of human T-leukemic cell adhesion to ICAM-1 in shear flow." Microvasc Res **55**(2): 124-137.

Cao, J., S. Usami and C. Dong (1997). "Development of a side-view chamber for studying cell-surface adhesion under flow conditions." Ann Biomed Eng **25**(3): 573-580.

Case, N., B. Sen, J. A. Thomas, M. Styner, Z. Xie, C. R. Jacobs and J. Rubin (2011). "Steady and oscillatory fluid flows produce a similar osteogenic phenotype." Calcif Tissue Int **88**(3): 189-197.

Castella, L. F., L. Buscemi, C. Godbout, J. J. Meister and B. Hinz (2010). "A new lock-step mechanism of matrix remodelling based on subcellular contractile events." J Cell Sci **123**(Pt 10): 1751-1760.

Chaudhuri, O., S. H. Parekh, W. A. Lam and D. A. Fletcher (2009). "Combined atomic force microscopy and side-view optical imaging for mechanical studies of cells." Nat Methods **6**(5): 383-387.

Choi, C. K. and B. P. Helmke (2008). "Short-Term Shear Stress Induces Rapid Actin Dynamics in Living Endothelial Cells." Mol Cell Biomech **5**(4): 247-258.

Cowin, S. C., S. Weinbaum and Y. Zeng (1995). "A case for bone canaliculi as the anatomical site of strain generated potentials." J Biomech **28**(11): 1281-1297.

Dangaria, J. H. and P. J. Butler (2007). "Macrorheology and adaptive microrheology of endothelial cells subjected to fluid shear stress." Am J Physiol Cell Physiol **293**(5): C1568-1575.

Davidson, M. W. and R. E. Campbell (2009). "Engineered fluorescent proteins: innovations and applications." Nat Methods **6**(10): 713-717.

Dong, C., J. Cao, E. J. Struble and H. H. Lipowsky (1999). "Mechanics of leukocyte deformation and adhesion to endothelium in shear flow." Ann Biomed Eng **27**(3): 298-312.

Doyle, A., W. Marganski and J. Lee (2004). "Calcium transients induce spatially coordinated increases in traction force during the movement of fish keratocytes." J Cell Sci **117**(Pt 11): 2203-2214.

Duncan, R. L. and C. H. Turner (1995). "Mechanotransduction and the functional response of bone to mechanical strain." Calcif Tissue Int **57**(5): 344-358.

Faire, K., C. M. Waterman-Storer, D. Gruber, D. Masson, E. D. Salmon and J. C. Bulinski (1999). "E-MAP-115 (ensconsin) associates dynamically with microtubules in vivo and is not a physiological modulator of microtubule dynamics." J Cell Sci **112 (Pt 23)**: 4243-4255.

Fletcher, D. A. and R. D. Mullins (2010). "Cell mechanics and the cytoskeleton." Nature **463**(7280): 485-492.

Gardner, M. K., B. L. Sprague, C. G. Pearson, B. D. Cosgrove, A. D. Bicek, K. Bloom, . . . D. J. Odde (2010). "Model Convolution: A Computational Approach to Digital Image Interpretation." Cellular and Molecular Bioengineering **3**(2): 163-170.

Genetos, D. C., C. J. Kephart, Y. Zhang, C. E. Yellowley and H. J. Donahue (2007). "Oscillating fluid flow activation of gap junction hemichannels induces ATP release from MLO-Y4 osteocytes." J Cell Physiol **212**(1): 207-214.

Grashoff, C., B. D. Hoffman, M. D. Brenner, R. Zhou, M. Parsons, M. T. Yang, . . . M. A. Schwartz (2010). "Measuring mechanical tension across vinculin reveals regulation of focal adhesion dynamics." Nature **466**(7303): 263-266.

Gu, Y., M. R. Preston, J. Magnay, A. J. El Haj and S. J. Publicover (2001). "Hormonally-regulated expression of voltage-operated Ca(2+) channels in osteocytic (MLO-Y4) cells." Biochem Biophys Res Commun **282**(2): 536-542.

Guharay, F. and F. Sachs (1984). "Stretch-activated single ion channel currents in tissue-cultured embryonic chick skeletal muscle." The Journal of physiology **352**: 685-701.

Han, Y., S. C. Cowin, M. B. Schaffler and S. Weinbaum (2004). "Mechanotransduction and strain amplification in osteocyte cell processes." Proc Natl Acad Sci U S A **101**(47): 16689-16694.

Helmke, B. P., A. B. Rosen and P. F. Davies (2003). "Mapping mechanical strain of an endogenous cytoskeletal network in living endothelial cells." Biophys J **84**(4): 2691-2699.

Helmke, B. P., A. B. Rosen and P. F. Davies (2003). "Mapping mechanical strain of an endogenous cytoskeletal network in living endothelial cells." Biophysical Journal **84**(4): 2691-2699.

Hu;, Y.-L., Y.-S. Li;, Y. Wang; and S. Chien (2010). Focal Adhesion Kinase Dynamics under Shear Stress in Live Endothelial Cells Studied with a FRET Biosensor FASEB J. **24:** 784.781.

Humphrey, D., C. Duggan, D. Saha, D. Smith and J. Kas (2002). "Active fluidization of polymer networks through molecular motors." Nature **416**(6879): 413-416.

Huo, B., X. L. Lu, K. D. Costa, Q. Xu and X. E. Guo (2010). "An ATP-dependent mechanism mediates intercellular calcium signaling in bone cell network under single cell nanoindentation." Cell Calcium **47**(3): 234-241.

Ingber, D. E. (2003). "Tensegrity I. Cell structure and hierarchical systems biology." J Cell Sci **116**(Pt 7): 1157-1173.

Ishihara, Y., Y. Sugawara, H. Kamioka, N. Kawanabe, H. Kurosaka, K. Naruse and T. Yamashiro (2012). "In situ imaging of the autonomous intracellular Ca(2+) oscillations of osteoblasts and osteocytes in bone." Bone **50**(4): 842-852.

Jaasma, M. J., W. M. Jackson and T. M. Keaveny (2006). "The effects of morphology, confluency, and phenotype on whole-cell mechanical behavior." Ann Biomed Eng **34**(5): 759-768.

Jacobs, C. R., C. E. Yellowley, B. R. Davis, Z. Zhou, J. M. Cimbala and H. J. Donahue (1998). "Differential effect of steady versus oscillating flow on bone cells." J Biomech **31**(11): 969-976.

Juette, M. F., T. J. Gould, M. D. Lessard, M. J. Mlodzianoski, B. S. Nagpure, B. T. Bennett, . . . J. Bewersdorf (2008). "Three-dimensional sub-100 nm resolution fluorescence microscopy of thick samples." Nat Methods **5**(6): 527-529.

Juffer, P., R. T. Jaspers, P. Lips, A. D. Bakker and J. Klein-Nulend (2012). "Expression of muscle anabolic and metabolic factors in mechanically loaded MLO-Y4 osteocytes." Am J Physiol Endocrinol Metab **302**(4): E389-395.

Kamel, M. A., J. L. Picconi, N. Lara-Castillo and M. L. Johnson (2010). "Activation of beta-catenin signaling in MLO-Y4 osteocytic cells versus 2T3 osteoblastic cells by fluid flow shear stress and PGE2: Implications for the study of mechanosensation in bone." Bone **47**(5): 872-881.

Kamioka, H., Y. Sugawara, S. A. Murshid, Y. Ishihara, T. Honjo and T. Takano-Yamamoto (2006). "Fluid shear stress induces less calcium response in a single primary osteocyte than in a single osteoblast: implication of different focal adhesion formation." J Bone Miner Res **21**(7): 1012-1021.

Knight, M. M., Z. Bomzon, E. Kimmel, A. M. Sharma, D. A. Lee and D. L. Bader (2006). "Chondrocyte deformation induces mitochondrial distortion and heterogeneous intracellular strain fields." Biomech Model Mechanobiol **5**(2-3): 180-191.

Kramer, I., S. Baertschi, C. Halleux, H. Keller and M. Kneissel (2012). "Mef2c deletion in osteocytes results in increased bone mass." J Bone Miner Res **27**(2): 360-373.

Kramer, I., C. Halleux, H. Keller, M. Pegurri, J. H. Gooi, P. B. Weber, . . . M. Kneissel (2010). "Osteocyte Wnt/beta-catenin signaling is required for normal bone homeostasis." Mol Cell Biol **30**(12): 3071-3085.

Kwon, R. Y. and C. R. Jacobs (2007). "Time-dependent deformations in bone cells exposed to fluid flow in vitro: investigating the role of cellular deformation in fluid flow-induced signaling." J Biomech **40**(14): 3162-3168.

Lansman, J. B., T. J. Hallam and T. J. Rink (1987). "Single stretch-activated ion channels in vascular endothelial cells as mechanotransducers?" Nature **325**(6107): 811-813.

Lewis, J. P. (1995). Fast Template Matching. Vision Interface. Quebec City, Canada, Canadian Image Processing and Pattern Recognition Society. **95:** 120-123.

Leyton-Mange, J., S. Yang, M. H. Hoskins, R. F. Kunz, J. D. Zahn and C. Dong (2006). "Design of a side-view particle imaging velocimetry flow system for cell-substrate adhesion studies." J Biomech Eng **128**(2): 271-278.

Li, S., M. Kim, Y. L. Hu, S. Jalali, D. D. Schlaepfer, T. Hunter, . . . J. Y. Shyy (1997). "Fluid shear stress activation of focal adhesion kinase. Linking to mitogen-activated protein kinases." J Biol Chem **272**(48): 30455-30462.

Limouze, J., A. F. Straight, T. Mitchison and J. R. Sellers (2004). "Specificity of blebbistatin, an inhibitor of myosin II." J Muscle Res Cell Motil **25**(4-5): 337-341.

Lin, Y. C., G. H. Koenderink, F. C. MacKintosh and D. A. Weitz (2007). "Viscoelastic properties of microtubule networks." Macromolecules **40**(21): 7714-7720.

Lu, X. L., B. Huo, V. Chiang and X. E. Guo (2012). "Osteocytic network is more responsive in calcium signaling than osteoblastic network under fluid flow." J Bone Miner Res **27**(3): 563-574.

Lu, X. L., B. Huo, M. Park and X. E. Guo (2012). "Calcium response in osteocytic networks under steady and oscillatory fluid flow." Bone **51**(3): 466-473.

Marian, A., F. Charriere, T. Colomb, F. Montfort, J. Kuhn, P. Marquet and C. Depeursinge (2007). "On the complex three-dimensional amplitude point spread function of lenses and microscope objectives: theoretical aspects, simulations and measurements by digital holography." Journal of Microscopy-Oxford **225**(2): 156-169.

Miyauchi, A., K. Notoya, Y. Mikuni-Takagaki, Y. Takagi, M. Goto, Y. Miki, . . . T. Fujita (2000). "Parathyroid hormone-activated volume-sensitive calcium influx pathways in mechanically loaded osteocytes." J Biol Chem **275**(5): 3335-3342.

Miyawaki, A., J. Llopis, R. Heim, J. M. McCaffery, J. A. Adams, M. Ikura and R. Y. Tsien (1997). "Fluorescent indicators for Ca2+ based on green fluorescent proteins and calmodulin." Nature **388**(6645): 882-887.

Mott, R. E. and B. P. Helmke (2007). "Mapping the dynamics of shear stress-induced structural changes in endothelial cells." Am J Physiol Cell Physiol **293**(5): C1616-1626.

Munevar, S., Y. L. Wang and M. Dembo (2004). "Regulation of mechanical interactions between fibroblasts and the substratum by stretch-activated Ca2+ entry." J Cell Sci **117**(Pt 1): 85-92.

Murshid, S. A., H. Kamioka, Y. Ishihara, R. Ando, Y. Sugawara and T. Takano-Yamamoto (2007). "Actin and microtubule cytoskeletons of the processes of 3D-cultured MC3T3-E1 cells and osteocytes." J Bone Miner Metab **25**(3): 151-158.

Na, S., O. Collin, F. Chowdhury, B. Tay, M. Ouyang, Y. Wang and N. Wang (2008). "Rapid signal transduction in living cells is a unique feature of mechanotransduction." Proc Natl Acad Sci U S A **105**(18): 6626-6631.

Nakashima, T., M. Hayashi, T. Fukunaga, K. Kurata, M. Oh-Hora, J. Q. Feng, . . . H. Takayanagi (2011). "Evidence for osteocyte regulation of bone homeostasis through RANKL expression." Nat Med **17**(10): 1231-1234.

Ofek, G., D. C. Wiltz and K. A. Athanasiou (2009). "Contribution of the cytoskeleton to the compressive properties and recovery behavior of single cells." Biophys J **97**(7): 1873-1882.

Ohkubo, M., S. Wada, T. Matsumoto and K. Nishizawa (2006). "An effective method to verify line and point spread functions measured in computed tomography." Medical Physics **33**(8): 2757-2764.

Ouyang, M., J. Sun, S. Chien and Y. Wang (2008). "Determination of hierarchical relationship of Src and Rac at subcellular locations with FRET biosensors." Proc Natl Acad Sci U S A **105**(38): 14353-14358.

Owan, I., D. B. Burr, C. H. Turner, J. Qiu, Y. Tu, J. E. Onyia and R. L. Duncan (1997). "Mechanotransduction in bone: osteoblasts are more responsive to fluid forces than mechanical strain." Am J Physiol **273**(3 Pt 1): C810-815.

Paic, F., J. C. Igwe, R. Nori, M. S. Kronenberg, T. Franceschetti, P. Harrington, . . . I. Kalajzic (2009). "Identification of differentially expressed genes between osteoblasts and osteocytes." Bone **45**(4): 682-692.

Pan, B., H. M. Xie, Z. Q. Guo and T. Hua (2007). "Full-field strain measurement using a two-dimensional Savitzky-Golay digital differentiator in digital image correlation." Optical Engineering **46**(3): -.

Park, C. Y., D. Tambe, A. M. Alencar, X. Trepat, E. H. Zhou, E. Millet, . . . J. J. Fredberg (2010). "Mapping the cytoskeletal prestress." Am J Physiol Cell Physiol **298**(5): C1245-1252.

Pelletier, V., N. Gal, P. Fournier and M. L. Kilfoil (2009). "Microrheology of microtubule solutions and actin-microtubule composite networks." Phys Rev Lett **102**(18): 188303.

Piekarski, K. and M. Munro (1977). "Transport mechanism operating between blood supply and osteocytes in long bones." Nature **269**(5623): 80-82.

Pittet, M. J. and R. Weissleder (2011). "Intravital imaging." Cell **147**(5): 983-991.

Plotkin, L. I., I. Mathov, J. I. Aguirre, A. M. Parfitt, S. C. Manolagas and T. Bellido (2005). "Mechanical stimulation prevents osteocyte apoptosis: requirement of integrins, Src kinases, and ERKs." Am J Physiol Cell Physiol **289**(3): C633-643.

Poh, Y. C., S. Na, F. Chowdhury, M. Ouyang, Y. Wang and N. Wang (2009). "Rapid activation of Rac GTPase in living cells by force is independent of Src." PLoS One **4**(11): e7886.

Ponik, S. M., J. W. Triplett and F. M. Pavalko (2007). "Osteoblasts and osteocytes respond differently to oscillatory and unidirectional fluid flow profiles." J Cell Biochem **100**(3): 794-807.

Price, C., X. Zhou, W. Li and L. Wang (2011). "Real-time measurement of solute transport within the lacunar-canalicular system of mechanically loaded bone: direct evidence for load-induced fluid flow." J Bone Miner Res **26**(2): 277-285.

Rangaswami, H., R. Schwappacher, N. Marathe, S. Zhuang, D. E. Casteel, B. Haas, . . . R. B. Pilz (2010). "Cyclic GMP and protein kinase G control a Src-containing mechanosome in osteoblasts." Sci Signal **3**(153): ra91.

Rath, A. L., L. F. Bonewald, J. Ling, J. X. Jiang, M. E. Van Dyke and D. P. Nicolella (2010). "Correlation of cell strain in single osteocytes with intracellular calcium, but not intracellular nitric oxide, in response to fluid flow." J Biomech **43**(8): 1560-1564.

Reilly, G. C., T. R. Haut, C. E. Yellowley, H. J. Donahue and C. R. Jacobs (2003). "Fluid flow induced PGE2 release by bone cells is reduced by glycocalyx degradation whereas calcium signals are not." Biorheology **40**(6): 591-603.

Ren, J. and J. H. Wu (2012). "17beta-estradiol rapidly activates calcium release from intracellular stores via the GPR30 pathway and MAPK phosphorylation in osteocyte-like MLO-Y4 cells." Calcif Tissue Int **90**(5): 411-419.

Riedl, J., A. H. Crevenna, K. Kessenbrock, J. H. Yu, D. Neukirchen, M. Bista, . . . R. Wedlich-Soldner (2008). "Lifeact: a versatile marker to visualize F-actin." Nat Methods **5**(7): 605-607.

Riedl, J., K. C. Flynn, A. Raducanu, F. Gartner, G. Beck, M. Bosl, . . . R. Wedlich-Soldner (2010). "Lifeact mice for studying F-actin dynamics." Nat Meth **7**(3): 168-169.

Salmon, W. C., M. C. Adams and C. M. Waterman-Storer (2002). "Dual-wavelength fluorescent speckle microscopy reveals coupling of microtubule and actin movements in migrating cells." J Cell Biol **158**(1): 31-37.

Sampathkumar, A., J. J. Lindeboom, S. Debolt, R. Gutierrez, D. W. Ehrhardt, T. Ketelaar and S. Persson (2011). "Live Cell Imaging Reveals Structural Associations between the Actin and Microtubule Cytoskeleton in Arabidopsis." Plant Cell **23**(6): 2302-2313.

Sanderson, M. J., Y. Bai and J. Perez-Zoghbi (2010). "Ca(2+) oscillations regulate contraction of intrapulmonary smooth muscle cells." Advances in experimental medicine and biology **661**: 77-96.

Sato, M., K. Suzuki, Y. Ueki and T. Ohashi (2007). "Microelastic mapping of living endothelial cells exposed to shear stress in relation to three-dimensional distribution of actin filaments." Acta Biomater **3**(3): 311-319.

Shyy, J. Y. and S. Chien (1997). "Role of integrins in cellular responses to mechanical stress and adhesion." Current opinion in cell biology **9**(5): 707-713.

Stamenovic, D., Z. Liang, J. Chen and N. Wang (2002). "Effect of the cytoskeletal prestress on the mechanical impedance of cultured airway smooth muscle cells." J Appl Physiol **92**(4): 1443-1450.

Stamenovic, D., S. M. Mijailovich, I. M. Tolic-Norrelykke, J. Chen and N. Wang (2002). "Cell prestress. II. Contribution of microtubules." Am J Physiol Cell Physiol **282**(3): C617-624.

Sutton, M. A., M. Q. Cheng, W. H. Peters, Y. J. Chao and S. R. Mcneill (1986). "Application of an Optimized Digital Correlation Method to Planar Deformation Analysis." Image and Vision Computing **4**(3): 143-150.

Takai, E., K. D. Costa, A. Shaheen, C. T. Hung and X. E. Guo (2005). "Osteoblast elastic modulus measured by atomic force microscopy is substrate dependent." Ann Biomed Eng **33**(7): 963-971.

Takai, E., R. Landesberg, R. W. Katz, C. T. Hung and X. E. Guo (2006). "Substrate modulation of osteoblast adhesion strength, focal adhesion kinase activation, and responsiveness to mechanical stimuli." Mol Cell Biomech **3**(1): 1-12.

Tanaka-Kamioka, K., H. Kamioka, H. Ris and S. S. Lim (1998). "Osteocyte shape is dependent on actin filaments and osteocyte processes are unique actin-rich projections." J Bone Miner Res **13**(10): 1555-1568.

Tang, J., J. Akerboom, A. Vaziri, L. L. Looger and C. V. Shank (2010). "Near-isotropic 3D optical nanoscopy with photon-limited chromophores." Proc Natl Acad Sci U S A **107**(22): 10068-10073.

Tang, Y., X. Wu, W. Lei, L. Pang, C. Wan, Z. Shi, . . . X. Cao (2009). "TGF-beta1-induced migration of bone mesenchymal stem cells couples bone resorption with formation." Nature medicine **15**(7): 757-765.

Tatsumi, S., K. Ishii, N. Amizuka, M. Li, T. Kobayashi, K. Kohno, . . . K. Ikeda (2007). "Targeted ablation of osteocytes induces osteoporosis with defective mechanotransduction." Cell Metab **5**(6): 464-475.

Taylor, A. F., M. M. Saunders, D. L. Shingle, J. M. Cimbala, Z. Zhou and H. J. Donahue (2007). "Mechanically stimulated osteocytes regulate osteoblastic activity via gap junctions." Am J Physiol Cell Physiol **292**(1): C545-552.

ten Dijke, P. and H. M. Arthur (2007). "Extracellular control of TGFbeta signalling in vascular development and disease." Nature reviews: Molecular cell biology **8**(11): 857-869.

Thompson, W. R., A. S. Majid, K. J. Czymmek, A. L. Ruff, J. Garcia, R. L. Duncan and M. C. Farach-Carson (2011). "Association of the alpha(2)delta(1) subunit with Ca(v)3.2 enhances membrane expression and regulates mechanically induced ATP release in MLO-Y4 osteocytes." J Bone Miner Res **26**(9): 2125-2139.

Trickey, W. R., T. P. Vail and F. Guilak (2004). "The role of the cytoskeleton in the viscoelastic properties of human articular chondrocytes." J Orthop Res **22**(1): 131-139.

Tzima, E., M. A. Del Pozo, W. B. Kiosses, S. A. Mohamed, S. Li, S. Chien and M. A. Schwartz (2002). "Activation of Rac1 by shear stress in endothelial cells mediates both cytoskeletal reorganization and effects on gene expression." EMBO J **21**(24): 6791-6800.

Ueki, Y., N. Sakamoto and M. Sato "Direct measurement of shear strain in adherent vascular endothelial cells exposed to fluid shear stress." Biochem Biophys Res Commun **394**(1): 94-99.

van Hove, R. P., P. A. Nolte, A. Vatsa, C. M. Semeins, P. L. Salmon, T. H. Smit and J. Klein-Nulend (2009). "Osteocyte morphology in human tibiae of different bone pathologies with different bone mineral density--is there a role for mechanosensing?" Bone **45**(2): 321-329.

Vatsa, A., R. G. Breuls, C. M. Semeins, P. L. Salmon, T. H. Smit and J. Klein-Nulend (2008). "Osteocyte morphology in fibula and calvaria --- is there a role for mechanosensing?" Bone **43**(3): 452-458.

Vatsa, A., C. M. Semeins, T. H. Smit and J. Klein-Nulend (2008). "Paxillin localisation in osteocytes--is it determined by the direction of loading?" Biochem Biophys Res Commun **377**(4): 1019-1024.

Wang, C. C., J. M. Deng, G. A. Ateshian and C. T. Hung (2002). "An automated approach for direct measurement of two-dimensional strain distributions within articular cartilage under unconfined compression." J Biomech Eng **124**(5): 557-567.

Wang, N., J. P. Butler and D. E. Ingber (1993). "Mechanotransduction across the cell surface and through the cytoskeleton." Science **260**(5111): 1124-1127.

Wang, N., S. Hu and J. P. Butler (2007). "Imaging stress propagation in the cytoplasm of a living cell." Methods Cell Biol **83**: 179-198.

Wang, N., K. Naruse, D. Stamenovic, J. J. Fredberg, S. M. Mijailovich, I. M. Tolic-Norrelykke, . . . D. E. Ingber (2001). "Mechanical behavior in living cells consistent with the tensegrity model." Proc Natl Acad Sci U S A **98**(14): 7765-7770.

Wang, N., I. M. Tolic-Norrelykke, J. Chen, S. M. Mijailovich, J. P. Butler, J. J. Fredberg and D. Stamenovic (2002). "Cell prestress. I. Stiffness and prestress are closely associated in adherent contractile cells." Am J Physiol Cell Physiol **282**(3): C606-616.

Wang, Y., E. L. Botvinick, Y. Zhao, M. W. Berns, S. Usami, R. Y. Tsien and S. Chien (2005). "Visualizing the mechanical activation of Src." Nature **434**(7036): 1040-1045.

Wang, Y., L. M. McNamara, M. B. Schaffler and S. Weinbaum (2007). "A model for the role of integrins in flow induced mechanotransduction in osteocytes." Proc Natl Acad Sci U S A **104**(40): 15941-15946.

Weinbaum, S., S. C. Cowin and Y. Zeng (1994). "A model for the excitation of osteocytes by mechanical loading-induced bone fluid shear stresses." Journal of biomechanics **27**(3): 339-360.

Xing, Z., H. C. Chen, J. K. Nowlen, S. J. Taylor, D. Shalloway and J. L. Guan (1994). "Direct interaction of v-Src with the focal adhesion kinase mediated by the Src SH2 domain." Mol Biol Cell **5**(4): 413-421.

Xiong, J., M. Onal, R. L. Jilka, R. S. Weinstein, S. C. Manolagas and C. A. O'Brien (2011). "Matrix-embedded cells control osteoclast formation." Nat Med **17**(10): 1235-1241.

Yang, W., M. A. Harris, J. G. Heinrich, D. Guo, L. F. Bonewald and S. E. Harris (2009). "Gene expression signatures of a fibroblastoid preosteoblast and cuboidal osteoblast cell model compared to the MLO-Y4 osteocyte cell model." Bone **44**(1): 32-45.

Yellowley, C. E., C. R. Jacobs, Z. Li, Z. Zhou and H. J. Donahue (1997). "Effects of fluid flow on intracellular calcium in bovine articular chondrocytes." The American journal of physiology **273**(1 Pt 1): C30-36.

You, J., C. E. Yellowley, H. J. Donahue, Y. Zhang, Q. Chen and C. R. Jacobs (2000). "Substrate deformation levels associated with routine physical activity are less stimulatory to bone cells relative to loading-induced oscillatory fluid flow." J Biomech Eng **122**(4): 387-393.

You, L., S. Temiyasathit, P. Lee, C. H. Kim, P. Tummala, W. Yao, . . . C. R. Jacobs (2008). "Osteocytes as mechanosensors in the inhibition of bone resorption due to mechanical loading." Bone **42**(1): 172-179.

Young, S. R., R. Gerard-O'Riley, J. B. Kim and F. M. Pavalko (2009). "Focal adhesion kinase is important for fluid shear stress-induced mechanotransduction in osteoblasts." J Bone Miner Res **24**(3): 411-424.

Young, S. R., J. M. Hum, E. Rodenberg, C. H. Turner and F. M. Pavalko (2011). "Non-overlapping functions for Pyk2 and FAK in osteoblasts during fluid shear stress-induced mechanotransduction." PLoS One **6**(1): e16026.

Zhou, P. and K. E. Goodson (2001). "Subpixel displacement and deformation gradient measurement using digital image/speckle correlation (DISC)." Optical Engineering **40**(8): 1613-1620.

Zhu, D., N. C. Mackenzie, J. L. Millan, C. Farquharson and V. E. MacRae (2011). "The appearance and modulation of osteocyte marker expression during calcification of vascular smooth muscle cells." PLoS One **6**(5): e19595.